



**HAL**  
open science

# Energetic ion processing of aromatic molecules in the solid phase

Anna Bychkova

► **To cite this version:**

Anna Bychkova. Energetic ion processing of aromatic molecules in the solid phase. Astrophysics [astro-ph]. Normandie Université, 2024. English. NNT : 2024NORMC236 . tel-04866360

**HAL Id: tel-04866360**

**<https://theses.hal.science/tel-04866360v1>**

Submitted on 6 Jan 2025

**HAL** is a multi-disciplinary open access archive for the deposit and dissemination of scientific research documents, whether they are published or not. The documents may come from teaching and research institutions in France or abroad, or from public or private research centers.

L'archive ouverte pluridisciplinaire **HAL**, est destinée au dépôt et à la diffusion de documents scientifiques de niveau recherche, publiés ou non, émanant des établissements d'enseignement et de recherche français ou étrangers, des laboratoires publics ou privés.

# THÈSE

Pour obtenir le diplôme de doctorat

Spécialité **PHYSIQUE**

Préparée au sein de l'**Université de Caen Normandie**

**Energetic ion processing of aromatic molecules in the solid phase**

Présentée et soutenue par

**ANNA BYCHKOVA**

**Thèse soutenue le 26/11/2024**

devant le jury composé de :

MME ALICJA DOMARACKA	Directeur de recherche au CNRS - 14 GANIL de CAEN	Directeur de thèse
M. PHILIPPE BODUCH	Maître de conférences - Université de Caen Normandie (UCN)	Co-directeur de thèse
M. HERVE COTTIN	Professeur des universités - UNIVERSITE PARIS 12 VAL DE MARNE	Président du jury
MME AUDE SIMON	Directeur de recherche - CNRS	Membre du jury
M. BRUNO MANIL	Professeur des universités - Sorbonne Université	Rapporteur du jury
MME JENNIFER NOBLE	Chargé de recherche HDR - CNRS	Rapporteur du jury

Thèse dirigée par **ALICJA DOMARACKA** (Centre de recherche sur les ions, les matériaux et la photonique (Caen)) et **PHILIPPE BODUCH** (Université de Caen Normandie)



## **Energetic ion processing of aromatic molecules in the solid phase**

Formed in the dense clouds, icy mantles are condensates of small molecules on solid grains. These icy mantles are promising sites for rich chemical processes, where complex organic molecules can form, as these mantles are continuously exposed to ionizing radiation. Once dense clouds transform into an accretion disc and eventually into a planetary system, these icy mantles may potentially contribute to the reservoir of the complex molecules of the planets.

In this thesis, the effects of ion irradiation on two aromatic molecules, pyridine and pyrene were investigated. The samples were exposed to ion irradiation at the GANIL (Caen, France) and ATOMKI (Debrecen, Hungary) ion beam facilities. Their evolution was monitored using in-situ infrared spectroscopy. It was found that the initial structure (amorphous or crystalline) and the irradiation temperature do not affect the destruction cross section of pure pyridine. Additionally, it was observed that the local dose is not a key parameter as previously assumed. Indeed, since the destruction of pyrene caused by heavy ions, starting from C, is significantly greater than that caused by lighter ions such as H and He for the same deposited local dose. For both molecules, a significant increase in the destruction cross section was observed for decreasing molecule concentration in the water matrix. The half-life time of pyridine and pyrene in dense clouds was estimated to be around 13 and 20 millions of years, respectively. This suggests that once formed in these environments, they could survive and contribute to planetary formation.

### **Évolution des molécules aromatiques en phase solide sous irradiation par des ions énergétiques**

Dans les nuages denses, les manteaux glacés sont des condensats de petites molécules sur des grains solides. Ces manteaux glacés représentent des sites prometteurs pour certains processus chimiques. Ils sont constamment irradiés et de nouvelles molécules organiques complexes peuvent être ainsi formées. Une fois que les nuages denses se transforment en disque d'accrétion et, éventuellement, en système planétaire, ces manteaux glacés peuvent potentiellement contribuer au réservoir de molécules complexes des planètes.

Dans cette thèse, les effets de l'irradiation ionique sur deux molécules aromatiques, la pyridine et le pyrène, ont été étudiés. Les échantillons ont été exposés à une irradiation ionique sur les lignes des accélérateurs du GANIL (Caen, France) et de l'ATOMKI (Debrecen, Hongrie). Leur évolution a été suivie par spectroscopie infrarouge in situ. Il a été constaté que la structure initiale (amorphe ou cristalline) et la température d'irradiation n'affectent pas la section efficace de destruction de la pyridine pure. De plus, il a été observé que la dose locale n'est pas un paramètre clé comme cela était affirmé précédemment. En effet, la destruction du pyrène provoquée par des ions lourds, à partir du carbone, est significativement plus importante que celle provoquée par des ions plus légers comme l'hydrogène et l'hélium pour une même dose locale déposée. Pour les deux molécules, une augmentation significative de la section efficace de destruction a été observée lorsque la concentration des molécules dans la matrice d'eau diminue. Le temps de demi-vie de la pyridine et du pyrène dans les nuages denses a été estimé à environ 13 et 20 millions d'années, respectivement. Cela suggère qu'une fois formées dans ces environnements, ces molécules pourraient survivre et contribuer à la formation planétaire.

## Table of contents:

1. Introduction .....	4
1.1 Complex organic molecules in space .....	4
1.1.1 Grains .....	5
1.1.2 Aromatic molecules of astrophysical interest .....	5
1.1.2.1 PAH hypothesis .....	6
1.1.3 Ice mantle evolution .....	8
1.2 Ions in space .....	10
1.3 Ion-matter interaction .....	12
1.3.1 Stopping power .....	13
1.3.1.1 Nuclear stopping power .....	15
1.3.1.2 Electronic stopping power .....	16
1.3.2 Radiation damage .....	17
1.3.2.1 Amorphization .....	17
1.3.2.2 Compaction .....	19
1.3.2.3 Radiolysis .....	19
1.3.2.4 Sputtering .....	20
1.4 Objective of the work .....	21
References .....	23
2. Experimental methodology .....	29
2.1 Ion beam facilities .....	29
2.1.1 GANIL .....	29
2.1.1.2 ARIBE platform .....	31
2.1.1.3 Flux calibration .....	32
2.1.2 ATOMKI .....	33
2.2 Infrared spectroscopy .....	34
2.3 Experimental setup .....	37
2.3.1 CASIMIR .....	37
2.3.2 IGLIAS .....	38
2.3.2.1 Oven .....	41
2.3.3 ICA setup .....	43
References .....	45
3. Ion irradiation of pyridine ice .....	47
3.1 Sample preparation .....	48

3.2 Pure pyridine irradiations – effect of initial ice structure .....	52
3.2.1 Results on amorphous samples irradiation .....	52
3.2.2 Results on crystalline samples irradiation.....	58
3.3 Pyridine-water mixtures irradiation.....	62
3.4 New molecules formation.....	68
References .....	75
4. Ion irradiation of pyrene ice .....	79
4.1 Sample preparations .....	80
4.2 Pure pyrene irradiations.....	81
4.2.1 Pyrene destruction as a function of deposited local dose .....	86
4.3 Results on pyrene-water irradiations .....	89
4.4 New molecules formation.....	94
References .....	99
5. Radioresistance of aromatic molecules: size effect.....	103
5.1 Sample preparations .....	104
5.2 Results .....	105
References .....	109
6. Astrophysical implications .....	111
References .....	115
Conclusion and perspectives .....	117

# 1. Introduction

## 1.1 Complex organic molecules in space

Over the last century, it has been discovered that organic molecules are widespread throughout our universe. The first molecules (CH, CN, CH<sup>+</sup>) were discovered in the 1930s through optical spectra in the gas phase (McKellar, 1940). In the 1960s, observations based on rotational transitions revealed the presence of ubiquitous molecular clouds. Detailed investigations of the characteristics of organic molecules in space, both in gas and solid phase, became possible with the launch of infrared observatories, such as the Infrared Space Observatory in 1995 and the Spitzer Space Telescope in 2005. It was revealed that the interstellar medium contains a vast number of large complex molecules (Tielens, 2013). To date, more than 200 types of complex organic molecules have been detected in space (Woon, 2024).

These discoveries have led to the hypothesis that organic molecules, which serve as essential building blocks for living organisms, were most likely delivered to the early Earth from space (Rothery, et al., 2018), rather than synthesized under terrestrial conditions. Molecules containing carbon are supposed to be essential participants in the stellar cycle, involved in both the formation and death of stars. As a result, they also contribute significantly to the formation of planetary systems (Figure 1.1) (Hansen, et al., 2022). Moreover, diverse organic matter was ubiquitously found in meteorites (Pizzarello, et al., 2006), (Sephton & Botta, 2005) and comets (Anders, 1989), (McKay & Roth, 2021), (Altwegg, et al., 2016), (Naraoka, et al., 2023). Thus, tracing the source and evolutionary path of carbon in space is crucial for gaining insights into the origins of life on Earth.

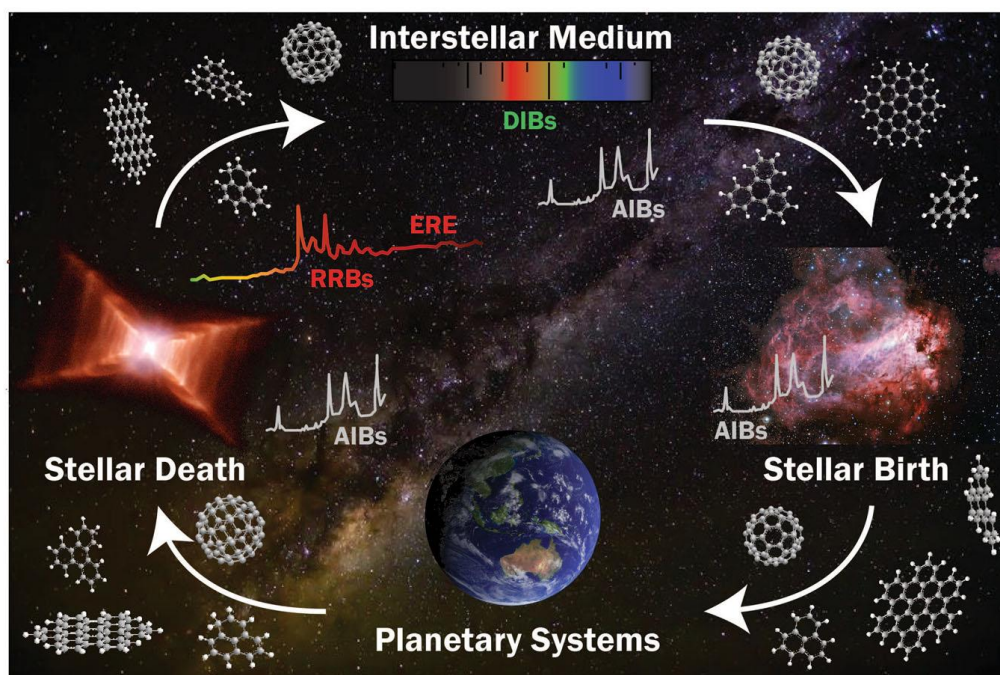


Figure 1.1. Carbon matter participates in the stellar life cycle. Extracted from (Hansen, et al., 2022).

### 1.1.1 Grains

A significantly higher number of molecules have been observed in the gas phase compared to the solid phase. This could be explained by the fact that the technique used to detect the rotational bands of gas-phase molecules is an order of magnitude more sensitive than infrared observations of the vibrational transitions of solid-state molecules (Rothard, et al., 2017). However, the chemistry occurring in the solid phase is particularly intriguing. When gas-phase molecules condense on the dust grains, they form a so-called "icy mantle". The chemistry that occurs in such icy mantles is of special interest as it represents an interface between refractory dust grains and gas-phase rich chemistry (Rothard, et al., 2017).

Dust grains uniformly mixed with the free gas molecules, represent  $\leq 1\%$  of the total mass of the interstellar medium (ISM) (Galliano, et al., 2018). They are formed from material ejected by ageing stars through gradual (stellar winds) or explosive (novae and supernovae) processes, where outflow conditions allow it. The nature of the material formed depends on the C/O ratio in the ejecta. When  $C/O < 1$  (oxygen-rich), the main products are silicates and when  $C/O > 1$  (carbon-rich), organic materials and carbides are formed (Sandford, et al., 2020). Solid grains composed of polycyclic aromatic hydrocarbons (PAHs) are also believed to be formed in the outflow of carbon-rich giants (Cherchneff, et al., 1992).

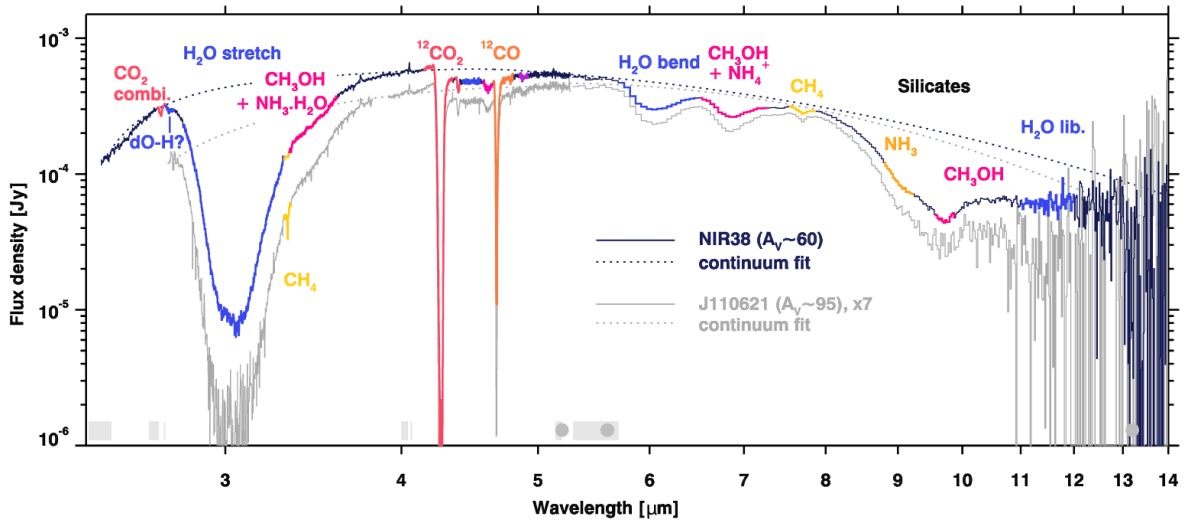


Figure 1.2. Ice features observations for two background stars NIR38 and J110621 obtained with JWST. Extracted from (McClure, et al., 2023).

Infrared spectra of two background stars are shown in Figure 1.2. Various molecules, including CO, CO<sub>2</sub>, CH<sub>3</sub>OH and CH<sub>4</sub> have been detected in the solid phase, along with the dominant ice constituent H<sub>2</sub>O, which makes up 60-70% of the ices in many environments (Gibb, et al., 2004), (Tielens, 2013). CO<sub>2</sub> and CO amount is around 10-20 and 20-40 % of H<sub>2</sub>O ice (McClure, et al., 2023).

### 1.1.2 Aromatic molecules of astrophysical interest

Aromatic molecules are organic compounds containing one or more aromatic rings. Unlike aliphatic compounds, these molecules exhibit high stability due to their delocalized  $\pi$



electron cloud. The term “aromatic” originally referred to the strong odour of the compounds, and now it signifies the presence of benzene or its structural relatives in the molecule. Aromatic compounds play a significant role in the biochemistry of all living organisms. They form molecules essential for genetic, energetic, structural, and signalling processes, such as deoxyribonucleic acid (DNA) and ribonucleic acid (RNA).

### 1.1.2.1 PAH hypothesis

Among other cyclic molecules, (PAHs) are believed to contain up to 25% of the elemental carbon in space (Tielens, 2008). Their fingerprints are observed everywhere (Figure 1.1): from dusty discs around young stars to the ISMs of galaxies (Candian, et al., 2018).

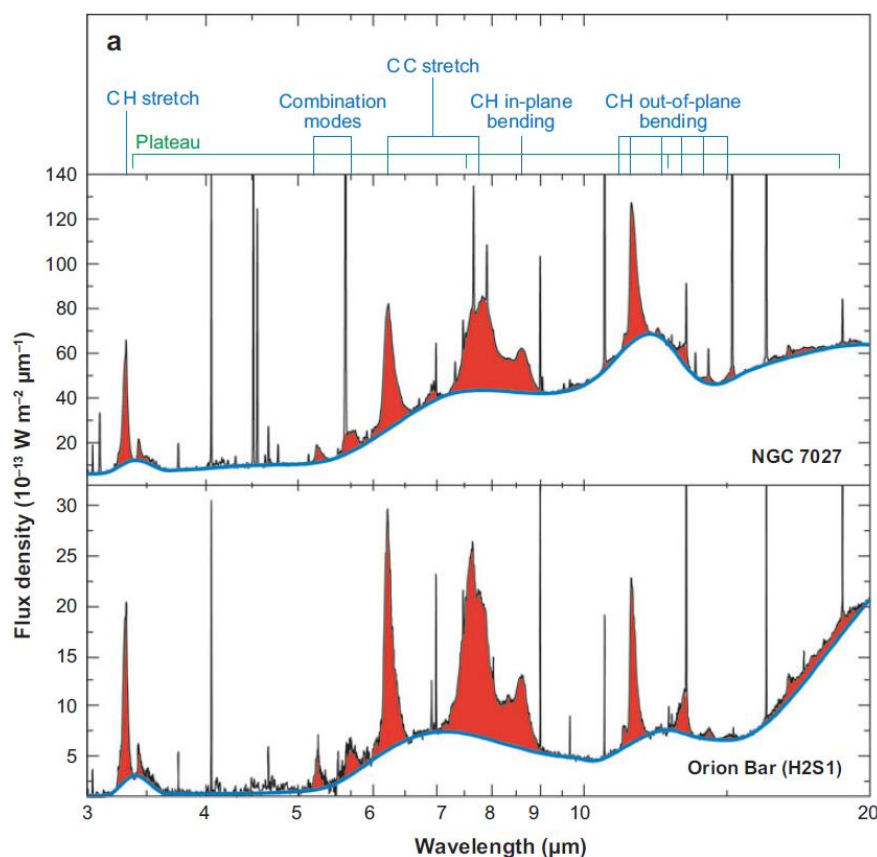


*Figure 1.3. The mid-infrared spectra of the planetary nebula NGC 7027 and the photodissociation region in the Orion Bar with highlighted PAH emission. Vibrational modes of PAH molecules are identified at the top. Extracted from (Tielens, 2008).*

In the 1960s, it was completely unexpected that a significant infrared excess, highlighted in red in Figure 1.3, could be seen in the planetary nebula NGC 7027 (Gillett, et al., 1967). The 3.3, 6.2, 7.7, 8.6, and 11.3  $\mu\text{m}$  (3030, 1613, 1299, 1163, 885  $\text{cm}^{-1}$  respectively) features were referred to as the unidentified infrared emission (UIE) bands since there are no counterparts in the infrared spectra of atoms. Since the work of (Duley & Williams, 1981), it has been widely recognised that UIE bands are caused by the carbonaceous compounds. The idea of assigning UIE bands to PAHs was proposed by (Leger & Puget, 1984) and (Allamandola, et al., 1985). According to their model, isolated PAH molecules absorb starlight in the ultraviolet (UV)

range, heating up to the temperatures of about 1000 K and then slowly cooling down by IR emission. The 3.3  $\mu\text{m}$  band was assigned to C-H stretching modes, the 6.2  $\mu\text{m}$  and 7.7  $\mu\text{m}$  features to C-C stretching, the 8.6  $\mu\text{m}$  feature to C-H in-plane bending, and the 11.3  $\mu\text{m}$  to C-H out-of-plane bending of PAH molecules (Allamandola, et al., 1989). The PAH hypothesis was summarized by (Tielens, 2008).

There are two main mechanisms explaining PAH formation in space: “bottom-up” and “top-down”. The first one implies the formation of PAH from smaller molecules, involving the closure of the first benzene ring and subsequent growth toward large PAHs. Different routes were proposed for the closure of the first benzene ring (Reizer, et al., 2022). For example, the reaction of 1,3-butadienyl radical ( $1,3\text{-}\dot{\text{C}}_4\text{H}_5$ ) with acetylene ( $\text{C}_2\text{H}_2$ ) (Frenklach, et al., 1985) or recombination of two propargyl radicals ( $\dot{\text{C}}_3\text{H}_3$ ) (Miller & Klippenstein, 2003). After the aromatic ring is closed PAH may growth according to different scenarios. The classical mechanism, proposed by (Frenklach, et al., 1985), is HACA, involving the sequence of hydrogen abstraction and subsequent acetylene ( $\text{C}_2\text{H}_2$ ) addition to the benzene ring. This process leads to the formation of polycyclic structure. Alternatives to HACA mechanism were also proposed in the literature (Mukherjee, et al., 1994), (Krestinin, et al., 2000), (Appel, et al., 2000). Subsequently, PAH molecules can aggregate into clusters (Figure 1.4) and form nanometer-scale carbonaceous grains (Rapacioli, et al., 2006), (Zhen, et al., 2019).

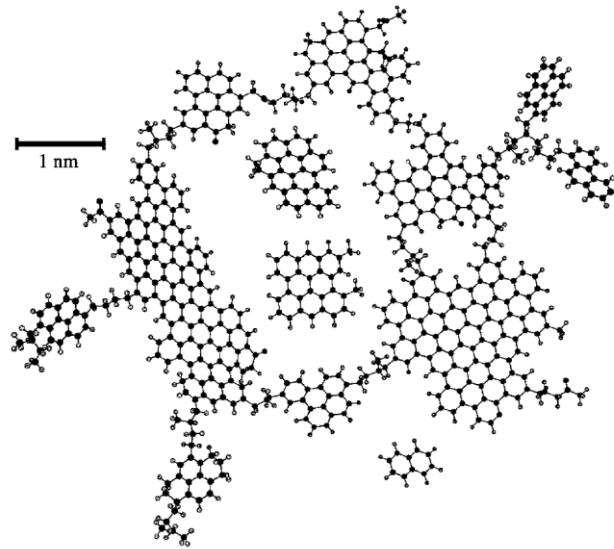


*Figure 1.4. The hypothesized representation of PAH cluster. Extracted from (Ehrenfreund, et al., 2002).*

Apparently, the “bottom-up” mechanism is not very efficient, as the molecular density is very low in the ISM. Thus, the “top-down” approach was proposed by (Berné & Tielens, 2012) to explain high concentration of PAHs and fullerenes in space. This “top-down” mechanism implies formation of PAHs from soot, injected to ISM from inner regions of evolved stars, fragmented by ionizing radiation and from PAH clusters itself (Figure 1.5). Several experimental works showed the feasibility of this process; variety of large PAH molecules were released while carbonaceous dust was exposed to radiation (Zhen, et al., 2018), (Pino, et al., 2019).

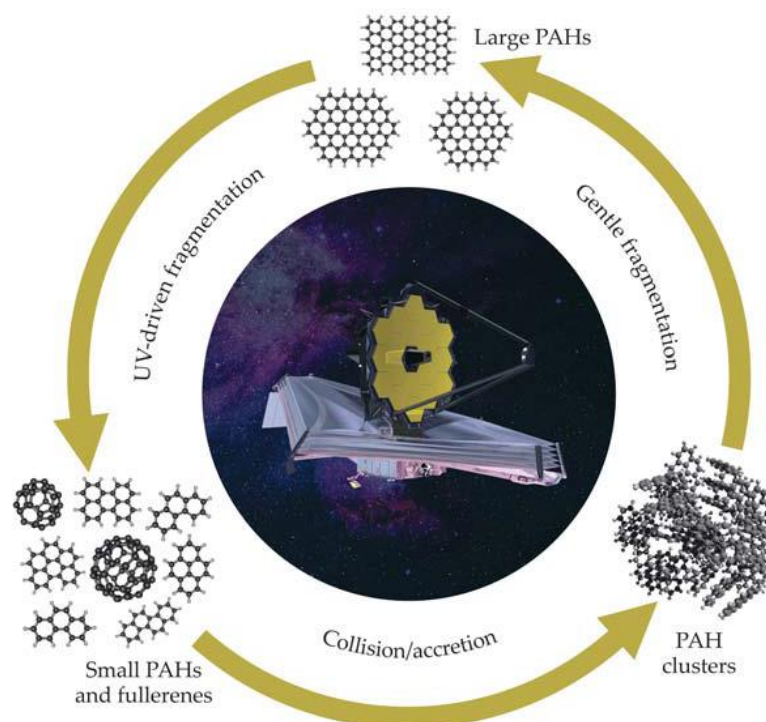


Figure 1.5. Life cycle of carbonaceous molecules. Extracted from (Candian, et al., 2018).

On Earth, PAHs are also extremely widespread and they are major air and water pollutants formed by the combustion of organic materials such as coal or oil.

A limitation of infrared spectrometry is its incapacity in this case to differentiate between specific molecules. This limitation arises because the vibrational modes, such as C-C and C-H, which are present for different PAH molecules, overlap in the infrared spectrum. Although detecting specific PAH molecules is possible using observations of millimeter wavelengths and radio frequencies through the molecule's rotational spectrum. However, only molecules possessing a permanent dipole moment can be detected with this method, which is not the case for many symmetric PAHs. Recently several PAHs were detected in the molecular cloud TMC-1: indene (Burkhardt, et al., 2021), (Cernicharo, et al., 2021), 1-cyanonaphthalene and 2-cyanonaphthalene (McGuire, et al., 2021). In all cases, it was reported that their concentration is much higher than expected, implying that existing models of PAH evolution in space need to be revised.

### 1.1.3 Ice mantle evolution

Dust grains, acting as nucleation sites, are composed of silicates, oxides, or PAH clusters and can reach sizes of up to several micrometers (Dartois, et al., 2024), (Gielen, et al., 2008). Molecular ice is thought to form in dense interstellar molecular clouds when gas-phase molecules and atoms condense into grains due to the low temperatures in these regions (Burke & Brown, 2010).

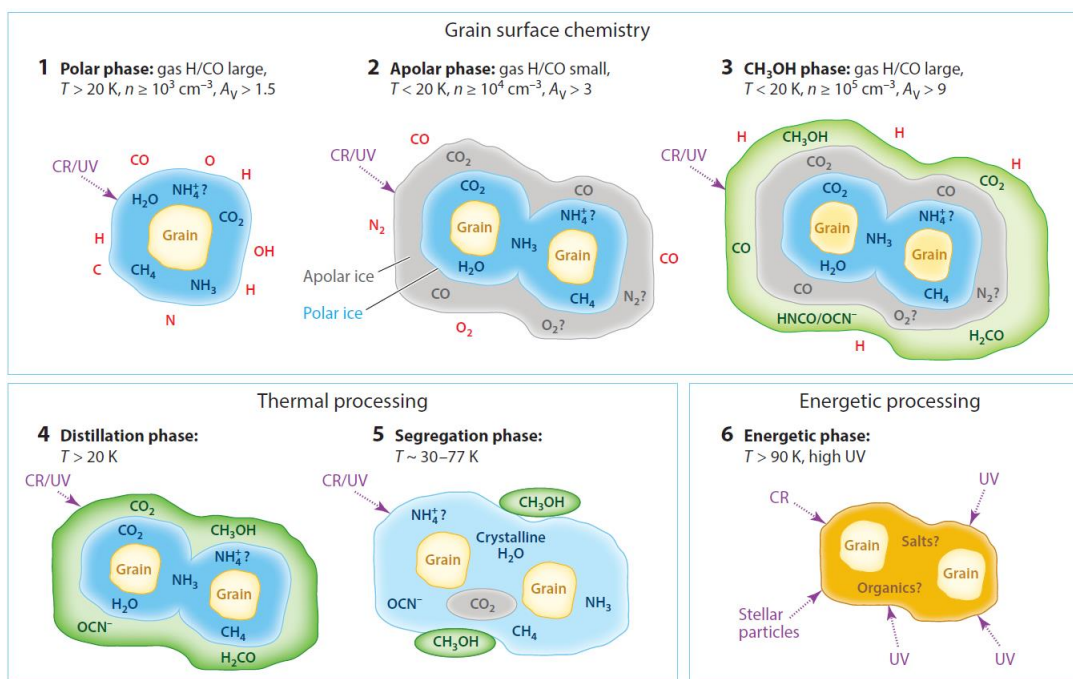


Figure 1.6. Scheme of ice grain evolution. Gas-phase species that can participate in surface reactions are indicated in red. CR – cosmic rays, UV – ultraviolet radiation. Extracted from (Boogert, et al., 2015).

The ice evolution model illustrated in Figure 1.6, has been summarised by (Boogert, et al., 2015). In the initial stage, atoms of hydrogen (H), nitrogen (N), carbon (C), and oxygen (O) combine to form basic molecules such as CH<sub>4</sub>, CO<sub>2</sub>, NH<sub>3</sub>, and H<sub>2</sub>O through processes like quantum tunnelling or thermal hopping on grain surfaces (Burke & Brown, 2010). PAHs can also freeze out in the ice mantle as guest molecules (Bouwman, et al., 2011). H<sub>2</sub>O is the dominant molecule in such ice, and it is referred to as polar ice. In regions characterized by temperatures lower than 20 K and densities around 10<sup>4</sup> cm<sup>-3</sup>, more volatile species such as CO, O<sub>2</sub>, and N<sub>2</sub> are formed, and this type of ice is referred to as apolar. The next stage of evolution is marked by a sharp increase in the concentration of methanol (CH<sub>3</sub>OH), as well as the appearance of molecules such as H<sub>2</sub>CO, OCN<sup>-</sup> and HNCO.

Once formed, icy mantles undergo constant thermal processing due to temperature variations in different regions of space. This results in sublimation, segregation, and crystallization of the compounds. For instance, water crystallization occurs beyond 125 K (Maté, et al., 2012). The thermal exposure also affects the chemistry, as radicals are more mobile and prone to reactions at higher temperatures (Boogert, et al., 2015).

However, the main driving force behind the emergence of a variety of molecules is the continuous processing of ice by ionizing radiation. UV photolysis and/or ion bombardment of interstellar ice produces radicals that can react with other molecules, forming species that are more complex. In regions of star formation, the gas and dust are heated to temperatures sufficient for these ices to evaporate (Garrod, et al., 2008). Subsequently, this set of gas- and solid-phase complex molecules incorporate into planetary systems. Thus, understanding the adsorption and desorption of ices on the grains is essential to comprehending the mechanisms underlying the formation of stars and planets (Burke & Brown, 2010).

## 1.2 Ions in space

Space is permeated with ionizing radiation, which mostly consist of electromagnetic radiation (UV and X-ray photons), as well as corpuscular radiation (electrons and ions). Galactic cosmic rays (GCR), the predominant corpuscular radiation in the interstellar medium, are charged particles of interstellar origin. Discovered by Victor Hess in 1912, they consists of 90% protons, 9% alpha particles and 1% are heavy ions (Gaisser, et al., 2016).

Figure 1.7 displays the number of particles as a function of energy of all-nuclear components present in CRs, reaching the Earth per unit time, surface, and solid angle. The spectrum is referred to as the "all-particle spectrum". In the high-energy part of the spectrum, there are three regions where a steepening occurs: knee ( $\approx 3 \cdot 10^6$  GeV), 2<sup>nd</sup> knee ( $\approx 2 \cdot 10^8$  GeV) and ankle ( $\approx 4 \cdot 10^9$  GeV) (Blasi 2013). However, there is no precise understanding yet of why these steepenings occur.

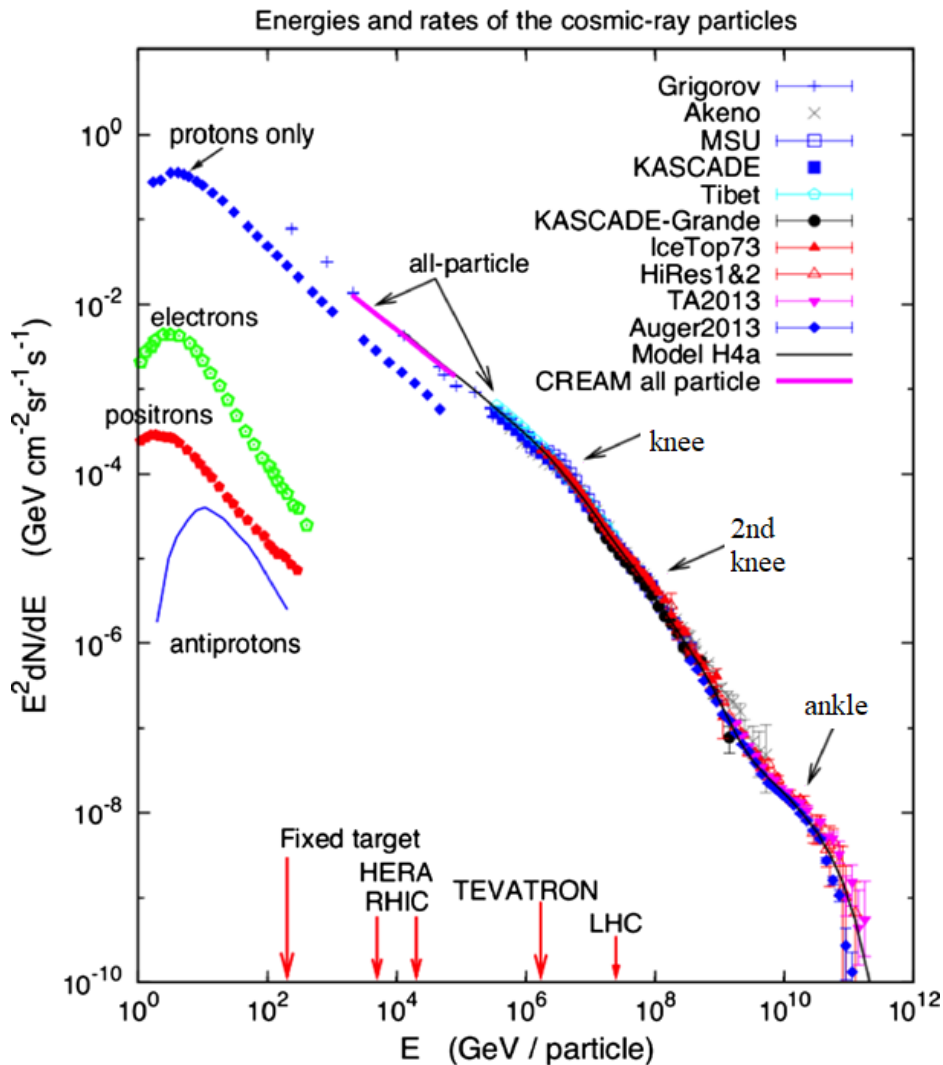


Figure 1.7. Spectrum of cosmic rays at the Earth. Spectrum measured by different experiments is plotted. Extracted from (Blasi, 2013).

GCRs with energies below  $10^7$  GeV are believed to be produced by supernovae. This view is based on the fact that the energy required to maintain the observed cosmic ray flux in

our Galaxy is slightly less than the average kinetic energy emitted into the interstellar medium by the three supernova explosions that occur every century. When a massive star collapses, its outer layers explosively disperse at speeds in excess of 10,000 kilometres per second. The ejected material from the supernova expands at supersonic speeds, creating a powerful shock wave that propagates into the surrounding medium. These shockwaves are expected to accelerate the nuclei within the passing material, transforming them into cosmic rays (Cronin, et al., 1997).

The origin of cosmic rays exhibiting energies above  $10^7$  GeV remain unidentified, and these particles are quite rare events. To study them effectively one needs detectors covering a large area. Currently, the implementation of such detectors is only feasible on terrestrial grounds. The main approach to study high-energy cosmic rays involves the detection of secondary particles, generated subsequent to the collision of a cosmic ray particle with gas molecules in Earth's atmosphere. Sometimes one cosmic ray particle can trigger over a million of new particles (Cronin, et al., 1997).

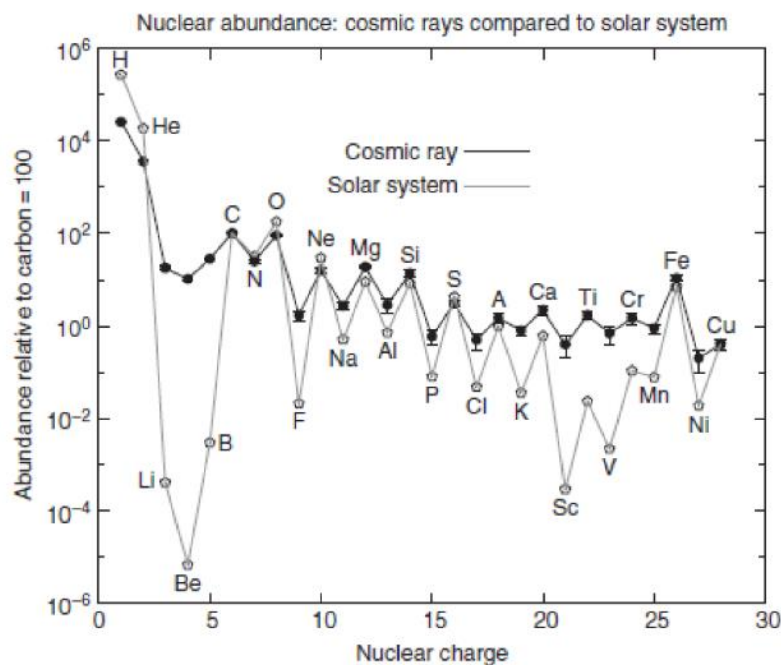


Figure 1.8. The cosmic ray (measured on Earth) and solar system elemental abundances relative to carbon = 100. Extracted from (Gaisser, et al., 2016).

Solar wind (SW) is a flow of charged particles released from the upper atmosphere of the Sun, mainly consists of protons (about 96%), alpha particles (about 4%) and ions of heavy elements (about 0.1%) (Wurz, 2005) with energies range from about 10 keV to several GeV (Reames, 2021). In Figure 1.8, the elemental abundances (H-Cu) of GCRs and SW are presented. The two groups of elements Li, Be, B and Sc, Ti, V, Cr, Mn are much more abundant in cosmic rays than in solar material. It happens because these elements are absent as products of stellar nucleosynthesis. Although they are present as spallation products of the abundant nuclei C and O (for Li, Be, B) or Fe (for Sc, Ti, V, Cr, Mn) with cosmic rays in the interstellar medium.

Figure 1.9 represents fluxes and energies of the most abundant nuclei of the GCRs and SW at the Earth orbit, including data from more than 10 experiments. It can be seen that the higher the atomic number of the element, the smaller its flux.

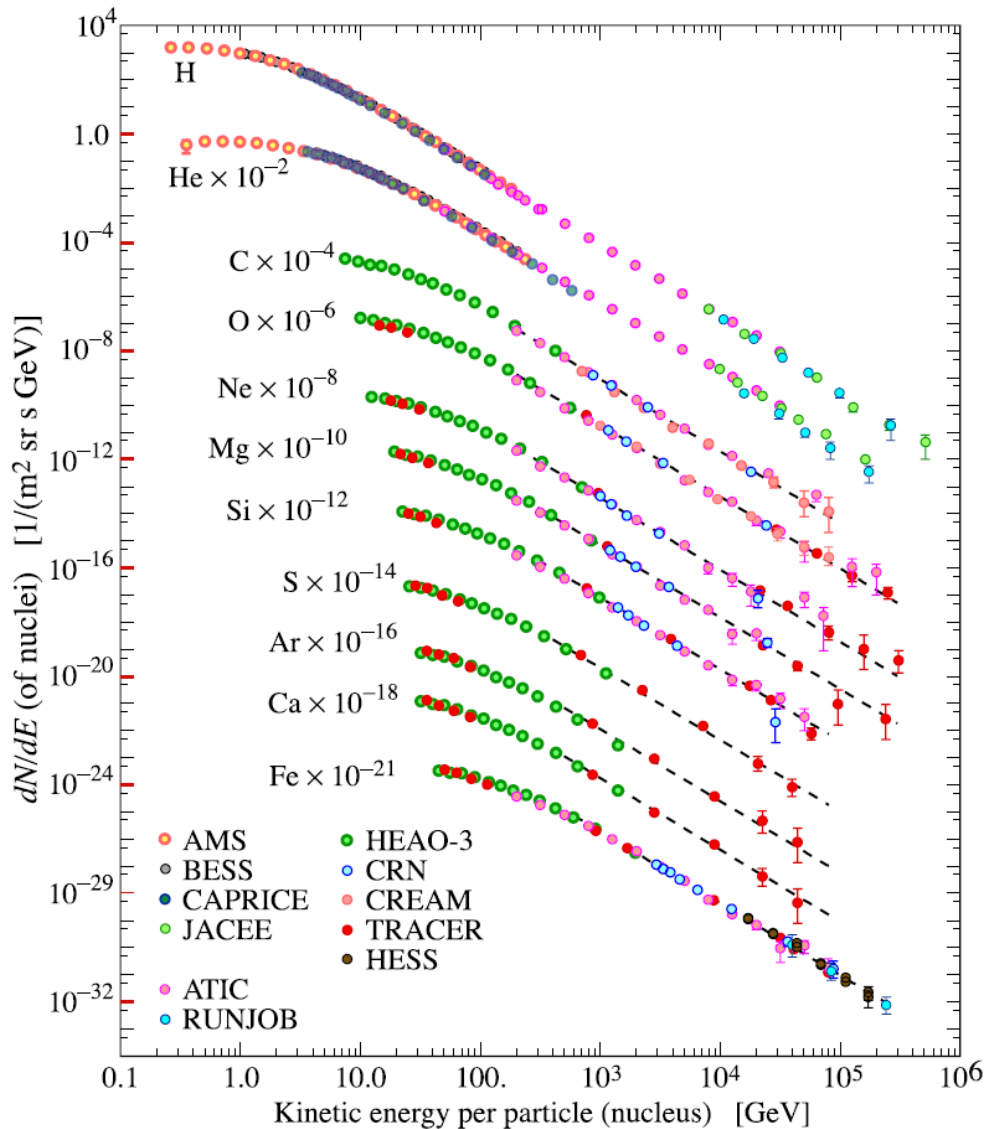


Figure 1.9. Fluxes of nuclei of the cosmic radiation as a function of energy per nucleus measured at different experiments near the Earth (sum of GCR and SW). Extracted from (Tanabashi, et al., 2018).

H and He are the predominant ions in space. However, heavier ions, ranging from C to Fe with energies of few tens of GeV per nucleon, are also relatively common. Given their potential to cause significant damage to materials, these heavier ions should not be disregarded in laboratory experiments investigating the evolution of icy mantles.

### 1.3 Ion-matter interaction

While swift ion beams penetrates the matter, collisions with target electrons can lead to excitation, ionisation and electron capture (Figure 1.10). The cross sections of these processes depend on the projectile energy. At velocities below the Bohr velocity, electron capture is the

dominant process. Above the Bohr velocity, ionisation becomes more and more important, while excitation occurs over the whole projectile velocity range.

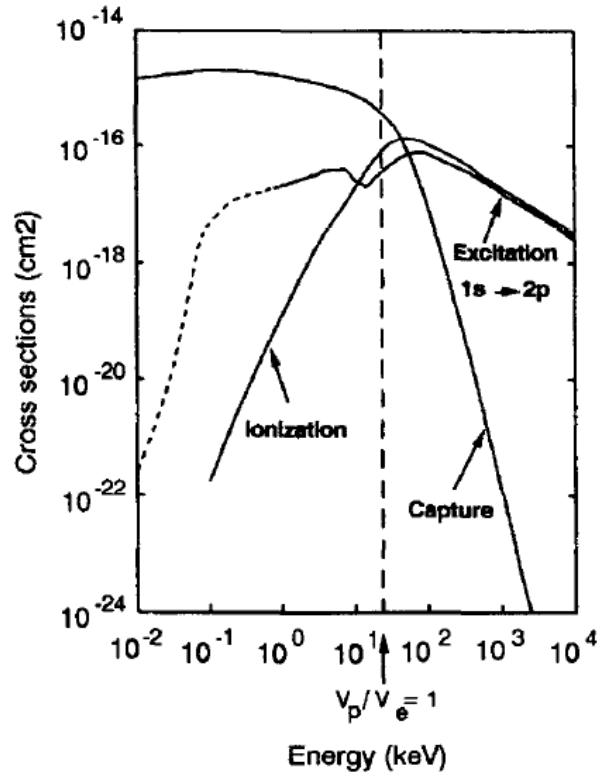


Figure 1.10. Capture, excitation and ionization cross sections as a function of energy for  $p + H$  collisions. Extracted from (Vernhet, et al., 1996).

The collision of GCR or SW particles with matter mainly results in ionization, potentially leading to significant harm to living organisms. On Earth, humans are shielded from this radiation by the Earth's magnetic field, redirecting the ions away from the surface. Although some ions manage to penetrate the atmosphere, they dissipate much of their energy through collisions with gas molecules, generating a cascade of secondary particles. In space, however, UV photons and ionic projectiles stand out as the dominant force driving astrochemistry, as they can dissociate molecules and create reactive radicals.

### 1.3.1 Stopping power

While traversing matter, ionic projectiles may lose kinetic energy through a sequence of elastic and inelastic collisions with the atoms of the target material.

The deposited energy may lead to the above-mentioned electronic processes and cause rearrangement of atoms in the solid. In elastic collisions with the nuclei of the atoms, energy is transferred to the target atom as a whole, leading to lattice disorder through the displacement of atoms from their original positions. The elastic interaction induces changes in both the energy and the trajectory of the ion, but the electronic configurations remain unchanged. Referred as nuclear energy loss  $S_n$ , it is dominant at low incident ion energies, which corresponds to SW particles.



Inelastic interaction with electrons may cause excitation or ionization of the target electrons. Inelastic ion-atom interaction (excitation or ionization of the target) causes the electronic energy loss  $S_e$ . The latter dominates at high ion energies (above 100 keV/u), which corresponds to GCR particles.

The boundary between inelastic and elastic energy loss of ions is blurred. These processes occur simultaneously but with different probabilities. The important parameters here are the atomic numbers of the projectile and the target material and the speed of the projectile. If the velocity of the ion exceeds the velocity of the electrons in their orbits, the ion will start losing electrons. In the limit of high velocity, the projectile will be completely stripped, leaving a "naked" nucleus with a charge  $Z_{pe}$  moving through the medium. The ion will only be able to recapture an electron after slowing down as it loses some of its energy through a series of Coulomb collisions with target electrons. Gradually, the ion loses energy and speed, capturing a second electron, a third, and so on, until its speed is diminished to a point below the orbital speed of the electron least strongly bound to the nucleus. The neutral incident particle generated from the described process exhibits weak interactions with the target electrons. The principal process leading to the deceleration of the particle shifts to elastic interactions with the target nuclei. The final stopping of the particle within the target occurs exclusively as result of elastic nuclear collisions.

The amount of energy loss per unit length of a particle along its path due to the "stopping power" of the target,  $\frac{dE}{dx}$  (keV/ $\mu\text{m}$ ) describes energy deposition in the material. The total energy loss is the sum of two components:

$$\frac{dE}{dx} = \left(\frac{dE}{dx}\right)_{nuclear} + \left(\frac{dE}{dx}\right)_{electronic} = S_n + S_e \quad \text{eq. (1.1)}$$

The energy loss in inelastic interaction with the nuclei and radiative processes such as bremsstrahlung and Cherenkov radiation are very small and neglected in our discussion.

In Figure 1.11 elastic nuclear and electronic energy loss of  $^{84}\text{Kr}^{15+}$  ion in amorphous pyridine are presented as a function of the ion energy. The calculations were performed using SRIM ("Stopping and Range of Ions in Matter") software (Ziegler, et al., 2010), which allows calculations of electronic stopping power  $S_e$ , nuclear stopping power  $S_n$  for all ions with energies up to 1 GeV/u while penetrating various materials. Knowing the stopping power allows calculating the total distance the ion travels before it stops - the ion range. As slow ions are subjected to elastic collisions with target atoms, this affects the trajectory of the ion, causing it to move in a zigzag pattern. Fast ions, on the other hand, are subjected to inelastic interactions, move in a straight line through the material with a slight deviation. If the projectile ion range is less than the target thickness, eventually the projectile ends up implanted in the material. Ion range can be calculated as (Nastasi, et al., 1996):

$$R = \int_{E_0}^0 \frac{1}{(S_n + S_e)} dE, \quad \text{eq. (1.2)}$$

where  $E_0$ - initial energy of the ion. SRIM also allows Monte Carlo simulations of ion trajectories. All calculations of  $S_e$ ,  $S_n$  and  $R$  in this thesis were performed using this software.

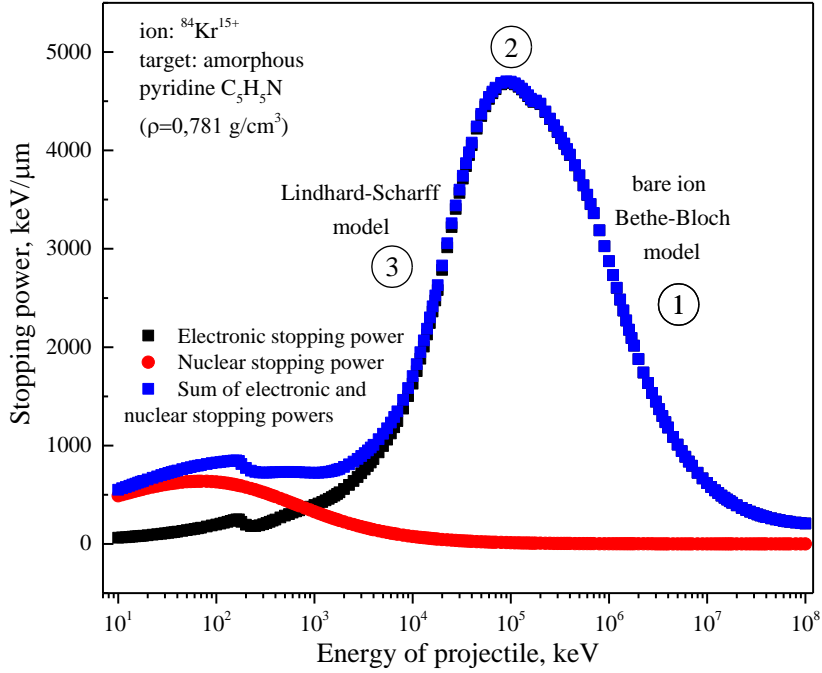


Figure 1.11. Electronic and nuclear stopping power for  $^{84}\text{Kr}^{15+}$  ion in amorphous pyridine target as a function of projectile energy calculated with SRIM (Ziegler, et al., 2010) software.

Most of the experiments in this thesis were performed with swift particles and we focus our attention on the inelastic interaction. The thickness of the samples was adjusted to be significantly less than the penetration depth, thereby maintaining a relatively constant ion energy throughout the sample. This also assures that the cross sections (ionisation, excitation, loss, capture) and thus the effective charge state of the ions remain constant. Only in the case of experiments involving low energy oxygen projectile, the ion remained implanted inside the sample.

### 1.3.1.1 Nuclear stopping power

The interaction potential of the Coulomb interaction depends on the distance between projectile and nucleus and is determined by the Coulomb force:

$$V(r) = \frac{Z_p Z_t}{r} \frac{e^2}{4\pi\epsilon_0} \times \varphi(x), \quad \text{eq. (1.3)}$$

where  $Z_p$  and  $Z_t$  – atomic numbers of the projectile and the nuclei of the target,  $r$  – distance between projectile and nuclei,  $\epsilon_0$  – electric constant,  $\varphi(x)$  – screening function.

Ion – nucleus interaction is entirely elastic, governed by the conservation laws of angular momentum and kinetic energy. Following this interaction, the trajectory of the ion changes and the target nucleus, upon obtaining sufficient energy, can leave its position (recoil) and begin to move within the target (as shown in Figure 1.12). The greater the energy of the incoming ion, the closer the particles can approach each other.

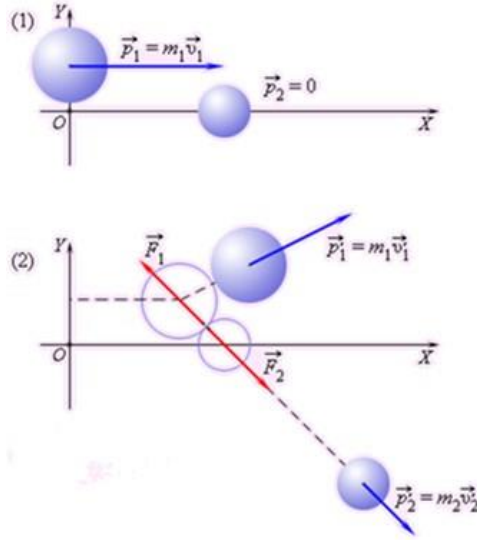


Figure 1.12. Schematic view of elastic collision between ion with mass  $m_1$  and velocity  $v_1$  and a resting target nucleus with mass  $m_2$ . After the collision velocity of ion became  $v_1'$  and velocity of nucleus became  $v_2'$ .

As the ion traverses the material, it encounters numerous collisions with the material's atoms. Each of these collisions results in the transfer of energy to the material and a corresponding reduction in the ion's energy:

$$\frac{dE}{dx} = N \int_0^{T_{max}} T \frac{d\sigma(T)}{dT} dT, \quad \text{eq. (1.4)}$$

Where  $N$  – number of collisions,  $T$  – energy loss during a single collision,  $\sigma(T)$  – collision cross section. A theoretical description of nuclear energy loss was provided by (Biersack, 1968):

$$S_n = \frac{4\pi a N M_p Z_p Z_t e^2}{M_p + M_t} \frac{\ln \varepsilon}{2\varepsilon(1-\varepsilon^{-1.49})}, \quad \text{eq. (1.5)}$$

where  $a$  is universal screening length and  $\varepsilon$  is the reduced energy, which can be calculated as:

$$a = \frac{0.8853 a_0}{(Z_p^2 + Z_t^2)^{\frac{1}{2}}}, \quad \text{eq. (1.6)}$$

$$\varepsilon = \frac{a M_t}{Z_p Z_t e^2 (M_p + M_t)} E, \quad \text{eq. (1.7)}$$

where  $M_p$  and  $M_t$  – atomic masses of the projectile and the target material,  $a_0 = 0.529 \text{ \AA}$  is the Bohr radius,  $N$  – number of atoms in the target per  $\text{cm}^3$ .

### 1.3.1.2 Electronic stopping power

Due to the low mass of electrons, the energy loss per single collision is always negligible compared to the energy of the incoming particle. At velocities below the maximum of the energy loss curve, the deceleration is therefore continuous and resembles stopping under the

effect of a frictional force. For the same reason that the electron mass is small, the transfer of momentum to the electrons is negligible.

The projectile will be completely stripped in the high velocity limit. The interaction of the bare nucleus with electrons occurs due to Coulomb forces and the electronic energy loss can be described by the Bethe-Bloch formula (Bethe, 1930) (Figure 1.10 ① regime):

$$S_e = \frac{4\pi n z_p^2 z_t e^4}{m_e v^2} \left[ \ln \frac{2m_e v^2}{I(1-\beta^2)} - \beta^2 - \frac{c}{z_t} \right], \quad \text{eq. (1.8)}$$

where  $n$  is the electron density in the matter,  $z_p$  and  $z_t$  are charge of the projectile and the nuclei of the target,  $m_e$  is the electron mass,  $v$  is the ion velocity,  $c$  is the speed of light,  $\beta = \frac{v}{c}$ ,  $I$  is the ionization potential of atoms of the matter.

The maximum of the electronic energy loss leads to the Bragg peak of maximum energy deposition at the end of the projectile range. In hadrontherapy, the ion energy is calculated so that this peak coincides with the cancer cells, thereby causing maximum damage to them (D'Auria, 2019). At energies near the maximum of the electronic energy curve (Figure 1.10 ② regime), the ion has begun capturing electrons. In order to determine electronic losses, a so-called effective charge  $z_{eff}$  is substituted into the Bethe-Bloch formula instead of the  $z_p$  (Spohr, 1990):

$$z_{eff} = z_p \left( 1 - e^{-125\beta z_p \frac{2}{3}} \right). \quad \text{eq. (1.9)}$$

After losing some of the energy and slowing down in the material (Figure 1.10 ③ regime – friction mode), electron capture by the projectile becomes dominant and the electronic energy loss is proportional to the speed of ion (Lindhard, et al., 1963), resembling a friction force:

$$S_e = Z_p^{1/6} 8\pi a_0 n \frac{z_p z_t}{(z_p^{2/3} - z_t^{2/3})^{3/2}} \frac{v}{v_e}, \quad \text{eq. (1.10)}$$

where  $v_e = 2.2 \cdot 10^6 \text{ m/s}$  is the speed of orbital electrons (Bohr velocity).

## 1.3.2 Radiation damage

This section will provide a description of the different types of damage that ions can induce in materials.

### 1.3.2.1 Amorphization

Under ion irradiation, crystalline ice can undergo a transformation into an amorphous state. Generally, there are two mechanisms for the amorphization of crystalline solids under ion irradiation, depending on the stopping power regime (Trinkaus, 1997).

When ions transfer energy to the target material through nuclear elastic collisions, amorphization takes place as a result of the defect accumulation (Pelaz, et al., 2004), (Wesch, 2016), (Gibbons, 1972). The incident ion induces primary recoils of target atoms, which in turn generates secondary recoils and so on, a phenomenon known as a collision cascade. This leads to the displacement and excitation of the target atoms and defects accumulation. If the deposited

energy reaches a sufficient level, it becomes energetically favourable for the defective lattice to undergo a transformation into an amorphous state (Pelaz, et al., 2004). This mechanism leads to the quasi-homogenous amorphization.

In the regime of electronic energy deposition, energy is supposed to be transferred from the electronic system to the ionic system via the so-called thermal spike mechanism (Toulemonde, et al., 1993), (Wang, et al., 1994), (Szenes, 1995), (Wesch, 2016). The core concept of the thermal spike model is that the energy introduced by a projectile in a confined area can rapidly heat the solid to a liquid or gaseous state. This is followed by exceptionally rapid cooling rates, leading to the creation of an amorphous phase along the ion trajectory, which is called the latent track (Famá, et al., 2010). In Figure 1.13 schema of latent track formation is illustrated. The sequence of energy transfer begins with incident ions imparting their energy to the electrons of the target through ion-electron collisions. Following this, through electron-electron collisions, the energy is shared among other cold electrons. Thirdly, energy is transmitted to the lattice via electron-phonon coupling, and lastly, it disperses among the atoms, creating a spike along the ion trajectory. The energy is deposited to the electrons within a timeframe ranging from  $10^{-16}$  to  $10^{-15}$  seconds, and subsequently, it is transferred to the lattice atoms within a period spanning from  $10^{-13}$  to  $10^{-11}$  seconds. The morphology of the latent track is highly dependent on the electronic stopping  $S_e$ , as is the track radius, which increases with higher  $S_e$ . It is evident that in this case, amorphization is inhomogeneous; however, at high ion fluence, individual tracks overlap, resulting in the formation of a specific microstructure in the material (Wesch, 2016).

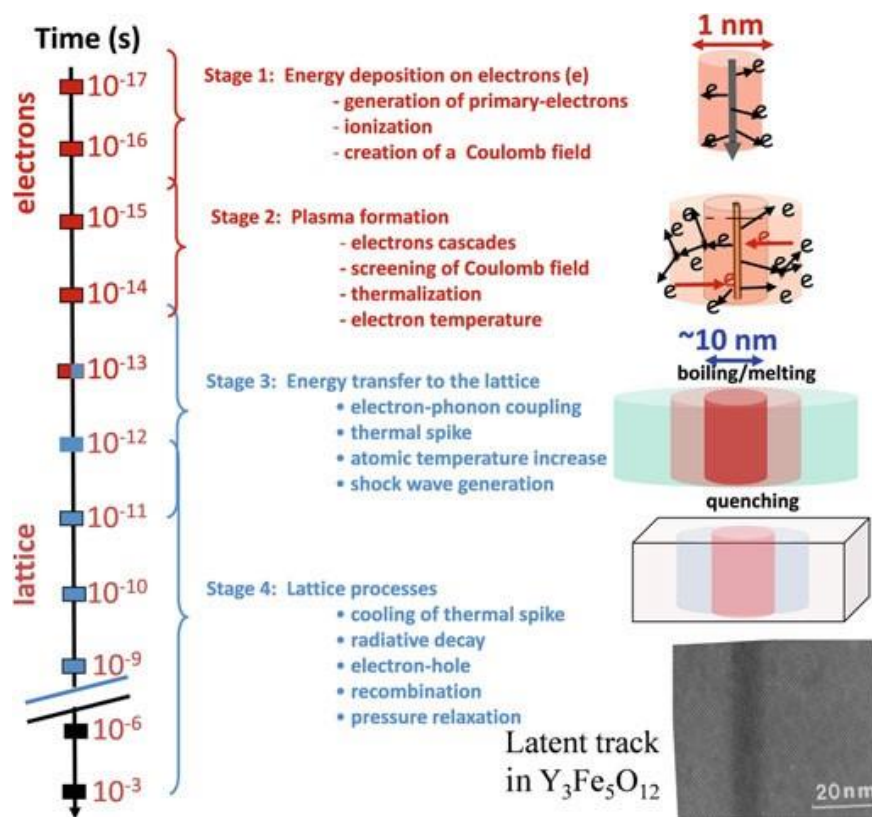


Figure 1.13. Latent track formation. Extracted from (Wesch, 2016).

In the “electronic regime”, amorphization is possible if  $S_e$  is above threshold value  $S_{e,t}$ , which depend on the properties of the target material. In materials where ion-induced amorphization is possible through electronic excitations, it can also occur through elastic collisions, although the opposite may not necessarily be true (Trinkaus, 1997). In case of molecular solids amorphization is driven by electronic interactions. Conversely, in covalent solids, amorphization is only observed in the presence of elastic collisions (Strazzulla, et al., 1992).

### 1.3.2.2 Compaction

Compaction is the process leading to a decrease in the porosity of amorphous ice under ion irradiation. In several studies (Palumbo, 2006), (Pilling, et al., 2010), (Mejía, et al., 2015), (Dartois, et al., 2013) the alteration of water porosity under the influence of ion irradiation was investigated based on the changes in the so-called OH-dangling bonds in the infrared spectra, which are considered as indicators of porosity of H<sub>2</sub>O (Rowland & Devlin, 1991). It has been observed that when the growth of the OH dangling bonds band area stops, compaction also finishes, and the density of the sample reaches its maximum value. In space, OH-dangling bonds were recently observed in the dense cloud Chamaeleon (Noble, et al., 2024).

While the precise mechanisms governing the process of compaction remain not completely understood, (Raut, et al., 2007) proposed that compaction occurs due to the reduction of the surface energy of ice resulting from local heating along the path of ions and the collision cascade with target molecules.

### 1.3.2.3 Radiolysis

Ionizing radiation interacting with molecules can induce dissociation of initial compounds and generate reactive radicals. This is referred to as “radiolysis”, which subsequently can lead to the formation of new molecular species. It is evident that radiolysis depends on the energy of the incident particles as well as on their nature; for example, heavy ions will cause significantly more damage than photons or electrons.

In the case of ion irradiation, the extent of destruction depends on the amount of energy the particle transfers to the material, which is mainly determined by its stopping power. Figure 1.14 presents the evolution of the number of pyrene molecules (column density) during irradiation with 39.2 MeV <sup>56</sup>Fe<sup>10+</sup>. The column density was calculated for the 3042 cm<sup>-1</sup> infrared band of pyrene (see Chapter 4 for details). The column density decreases due to its radiolysis under heavy ion irradiation. The fitting of the decrease follows exponential decay:

$$N(F) = N_0 e^{-\sigma_d F}, \quad \text{eq. (1.11)}$$

where  $N$  is the pyrene column density at the fluence  $F$ ,  $N_0$  is the initial column density (at  $F=0$ ),  $\sigma_d$  represents the destruction cross section, serving as a crucial indicator of the probability of molecule destruction. This parameter depends on the energy and nature of the incident ion, as well as the nature of the target. As previously noted, most experiments reported here were conducted in the high velocity “electronic stopping power” regime, when the sample thickness was significantly smaller than the projected range. Consequently, the ion energy can be

considered constant throughout its entire path within the material, and thus, the destruction cross section  $\sigma_d$  remains constant as well.

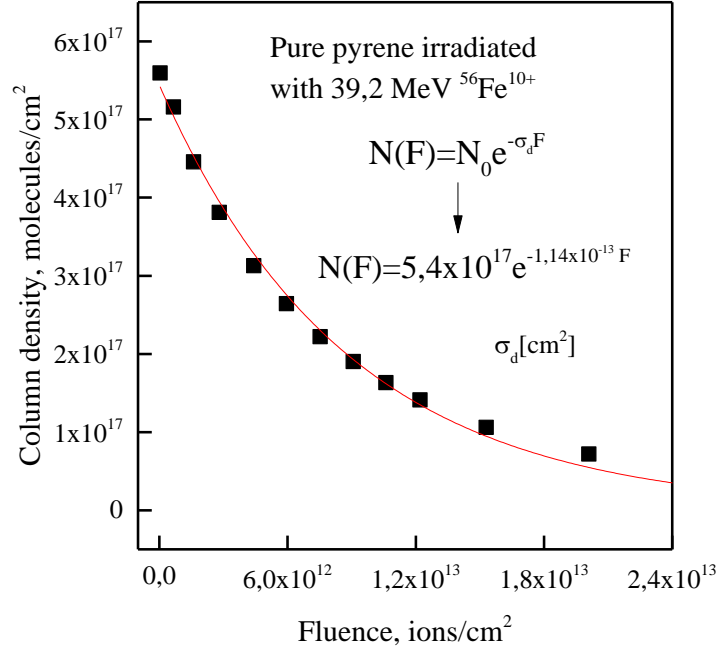


Figure 1.14. The fitted evolution of pyrene column density during irradiation with 39.2 MeV  $^{56}\text{Fe}^{10+}$ .

### 1.3.2.4 Sputtering

Sputtering is the emission of atoms from the surface of a solid body under bombardment by heavy charged or neutral particles. Sputtering of a target atom occurs when it receives an energy component perpendicular to the surface that exceeds the surface binding energy. Sputtering can be quantitatively assessed via the sputtering yield, defined as is the number of atoms removed from the surface per incident particle (Behrisch & Eckstein, 2007):

$$Y = \frac{\text{number of removed atoms}}{\text{number of incident particles}} \quad \text{eq. (1.12)}$$

In the interstellar medium and dense clouds sputtering leads to the transfer of solid phase species into the gas phase. Therefore, the chemical composition of the grains can significantly influence the evolution of molecules in the gas phase. Figure 1.15 presents sputtering yields for CO, CO<sub>2</sub> and H<sub>2</sub>O molecules as a function of electronic stopping power of the projectile. The quadratic dependence  $Y \sim S_e^2$  was observed in different experiments (Boduch, et al., 2015), (Dartois, et al., 2015), (Dartois, et al., 2023).

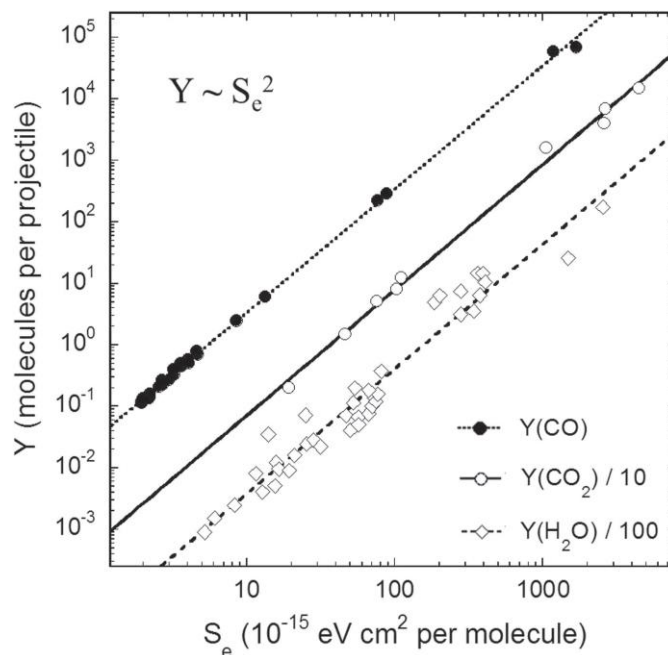


Figure 1.15. Sputtering yields for CO, CO<sub>2</sub> and H<sub>2</sub>O as a function of electronic stopping power of the projectile. The values for CO<sub>2</sub> were divided by 10 and for H<sub>2</sub>O by 100 for clarity. Extracted from (Rothard, et al., 2017).

## 1.4 Objective of the work

Grains in dense clouds and ISM are of the great astrochemical interest, as they participate in the carbon life cycle in space. Carbon can form carbonaceous grains itself or can freeze out inside the ice layer on the surface of solid grains. In time, these solid grains can be incorporated into planetary systems.

Ion bombardment of the solid grains results in the dissociation of the initial molecules, the formation of other complex species, structural changes within the lattice, and the release of the molecules into the gas phase. Although the majority of ions in space are charged particles of H and He, other heavier ions also affect the evolution of solid particles. Figure 1.16 (left) shows the abundance of different cosmic ray nuclei, with H and He being the most common. However, since the radiolysis effect is proportional to the square of the atomic number (Figure 1.16 middle), the impact of other ions can be just as significant as that of H and He. For sputtering (Figure 1.16 right), which depends on the atomic number to the power to four, the effect of heavy ions is much greater than that of lighter ions. Figure 1.16 clearly shows why it is important to study how heavy ions interact with matter in space.



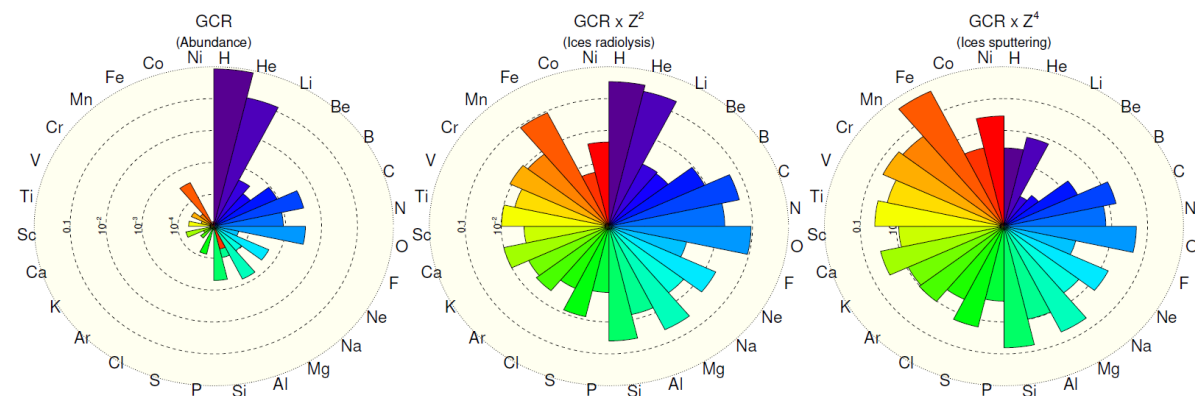


Figure 1.16. Fractional proportion of galactic cosmic ray elements. Left: abundance. Middle: radiolytic destruction of ices. Right: sputtering. Extracted from (Dartois, et al., 2023).

In this work, we investigated the radiolysis of carbonaceous films, made of two different aromatic molecules, pyrene and pyridine, induced by swift (mostly heavy) ions. Although grains involve in most cases a mixture of various molecules, this initial approximation provides insight into the overall radioresistance of these molecules. We studied the process of pyridine amorphization by several ionic projectiles and revealed the influence of temperature on the radiolysis rate. Another important focus of this work was studying the effects during icy mantles irradiation. As mentioned, water is the most abundant molecule in icy mantles, so we investigated the influence of the water matrix on the radiolysis of pyridine and pyrene.

## References

- Allamandola, L. J., Tielens, A. G. G. M. & Barker, J. R., 1985. Polycyclic aromatic hydrocarbons and the unidentified infrared emission bands-Auto exhaust along the Milky Way. *Astrophysical Journal, Part 2-Letters to the Editor (ISSN 0004-637X)*, pp. L25-L28.
- Allamandola, L. J., Tielens, A. G. G. M. & Barker, J. R., 1989. Interstellar polycyclic aromatic hydrocarbons-The infrared emission bands, the excitation/emission mechanism, and the astrophysical implications. *Astrophysical Journal Supplement Series (ISSN 0067-0049)*, pp. 733-775.
- Altaf, A. A. et al., 2015. A review on the medicinal importance of pyridine derivatives. *J. Drug Des. Med. Chem.*, pp. 1-11.
- Altwegg, K. et al., 2016. Prebiotic chemicals—amino acid and phosphorus—in the coma of comet 67P/Churyumov-Gerasimenko. *Science advances*, 2(5), p. e1600285.
- Anders, E., 1989. Pre-biotic organic matter from comets and asteroids. *Nature*, pp. 255-257.
- Appel, J., Bockhorn, H. & Frenklach, M., 2000. Kinetic modeling of soot formation with detailed chemistry and physics: laminar premixed flames of C2 hydrocarbons. *Combustion and flame*, 121(1-2), pp. 122-136.
- Behrisch, R. & Eckstein, W., 2007. *Sputtering by particle bombardment: experiments and computer calculations from threshold to MeV energies*. Berlin Heidelberg: Springer Science & Business Media.
- Berné, O., Montillaud, J. & Joblin, C., 2015. Top-down formation of fullerenes in the interstellar medium. *Astronomy & Astrophysics*, p. A133.
- Berné, O. & Tielens, A. G., 2012. Formation of buckminsterfullerene (C60) in interstellar space. *Proceedings of the National Academy of Sciences*, 109(2), pp. 401-406.
- Bethe, H., 1930. Zur theorie des durchgangs schneller korpuskularstrahlen durch materie. *Annalen der Physik*, pp. 325-400.
- Bibang, P. A., 2021. *Molécules organiques complexes sous irradiation: effets de la matrice et de la température*. Caen: Normandie Université.
- Bibang, P. A. et al., 2021. Radiolysis of pyridine in solid water. *The European Physical Journal D*, pp. 1-12.
- Biersack, J. P., 1968. Range of recoil atoms in isotropic stopping materials. *Zeitschrift für Physik A Hadrons and nuclei*, pp. 495-501.
- Blasi, P., 2013. The origin of galactic cosmic rays. *The Astronomy and Astrophysics Review*, pp. 1-73.
- Boduch, P. et al., 2015. Radiation effects in astrophysical ices. *Journal of Physics: Conference Series*, 629(1), p. 012008.
- Boogert, A. A., Gerakines, P. A. & Whittet, D. C., 2015. Observations of the icy universe. *Annual Review of Astronomy and Astrophysics*, pp. 541-581.

- Bouwman, J., Mattioda, A. L., Linnartz, H. & Allamandola, L. J., 2011. Photochemistry of Polycyclic Aromatic hydrocarbons in cosmic water ice-I. Mid-IR Spectroscopy and Photoproducts. *Astronomy & Astrophysics*, p. A93.
- Burke, D. J. & Brown, W. A., 2010. Ice in space: surface science investigations of the thermal desorption of model interstellar ices on dust grain analogue surfaces. *Physical Chemistry Chemical Physics*, pp. 5947-5969.
- Burkhardt, A. M. et al., 2021. Discovery of the pure polycyclic aromatic hydrocarbon indene (c-C<sub>9</sub>H<sub>8</sub>) with GOTHAM observations of TMC-1. *The Astrophysical Journal Letters*, 913(2), p. L18.
- Candian, A., Zhen, J. & Tielens, A. G., 2018. The aromatic universe. *Physics today*, pp. 38-43.
- Cernicharo, J. et al., 2021. Pure hydrocarbon cycles in TMC-1: Discovery of ethynyl cyclopropenylidene, cyclopentadiene, and indene. *Astronomy & Astrophysics*, Volume 649, p. L15.
- Cherchneff, I., Barker, J. R. & Tielens, A. G., 1992. Polycyclic aromatic hydrocarbon formation in carbon-rich stellar envelopes. *The Astrophysical Journal*, pp. 269-287.
- Cronin, J. W., Gaisser, T. K. & Swordy, S. P., 1997. Cosmic rays at the energy frontier. *Scientific American*, pp. 44-49.
- Dartois, E. et al., 2015. Heavy ion irradiation of crystalline water ice-Cosmic ray amorphisation cross-section and sputtering yield. *Astronomy & Astrophysics*, Volume 576, p. A125.
- Dartois, E. et al., 2023. Cosmic-ray sputtering of interstellar ices in the electronic regime-A compendium of selected literature yields. *Astronomy & Astrophysics*, Volume 671, p. A. 156.
- Dartois, E. et al., 2013. Swift heavy ion irradiation of water ice from MeV to GeV energies-Approaching true cosmic ray compaction. *Astronomy & Astrophysics*, Volume 557, p. A97.
- Dartois, E. et al., 2024. Spectroscopic sizing of interstellar icy grains with JWST. *Nature astronomy*, 8(3), pp. 359-367.
- D'Auria, S., 2019. *Introduction to nuclear and particle physics*. s.l.:Springer.
- Duley, W. W. & Williams, D. A., 1981. The infrared spectrum of interstellar dust: Surface functional groups on carbon. *Monthly Notices of the Royal Astronomical Society*, pp. 269-274.
- Ehrenfreund, P. et al., 2002. Astrophysical and astrochemical insights into the origin of life. *Reports on progress in physics*, 65(10), p. 1427.
- Famá, M., Loeffler, M. J., Raut, U. & Baragiola, R. A., 2010. Radiation-induced amorphization of crystalline ice. *Icarus*, pp. 314-319.
- Frenklach, M., Clary, D. W., Gardiner Jr, W. C. & Stein, S. E., 1985. Detailed kinetic modeling of soot formation in shock-tube pyrolysis of acetylene. *Symposium (International) on Combustion*, 20(1), pp. 887-901.
- Gaisser, T. K., Enger, R. & Resconi, E., 2016. *Cosmic Rays and Particle Physics*. Cambridge: Cambridge University Press.

- Galliano, F., Galametz, M. & Jones, A. P., 2018. The interstellar dust properties of nearby galaxies. *Annual Review of Astronomy and Astrophysics*, pp. 673-713.
- Garrod, R. T., Weaver, S. L. W. & Herbst, E., 2008. Complex chemistry in star-forming regions: An expanded gas-grain warm-up chemical model. *The Astrophysical Journal*, p. 283.
- Gibb, E. L., Whittet, D. C. B., Boogert, A. C. A. & Tielens, A. G. G., 2004. Interstellar ice: the infrared space observatory legacy. *The astrophysical journal supplement series*, p. 35.
- Gibbons, J. F., 1972. Ion implantation in semiconductors—Part II: Damage production and annealing. *Proceedings of the IEEE*, pp. 1062-1096.
- Gielen, C. et al., 2008. SPITZER survey of dust grain processing in stable discs around binary post-AGB stars. *Astronomy & Astrophysics*, 490(2), pp. 725-735.
- Gillett, F. C., Low, F. J. & Stein, W. A., 1967. Infrared observations of the planetary nebula NGC 7027. *Astrophysical Journal*, p. L97.
- Hansen, C. S., Peeters, E., Cami, J. & Schmidt, T. W., 2022. Open questions on carbon-based molecules in space. *Communications Chemistry*, 5(1), p. 94.
- Keane, J. V. et al., 2001. Bands of solid CO in the 2-3 $\mu$ m spectrum of S 140: IRS1. *Astronomy & Astrophysics*, pp. L43-L46.
- Krestinin, A. V. et al., 2000. On the mechanism of soot particle formation. *Kinetics and Catalysis*, Volume 41, pp. 90-98.
- Leger, A. & Puget, J. L., 1984. Identification of the 'unidentified' IR emission features of interstellar dust?. *Astronomy and Astrophysics (ISSN 0004-6361)*, pp. L5-L8.
- Lindhard, J., Scharff, M. & Schiøtt, H. E., 1963. *Range concepts and heavy ion ranges*. s.l.:Copenhagen : Munksgaard.
- Marin, L. G. et al., 2020. Low-temperature formation of carbonaceous dust grains from PAHs. *The Astrophysical Journal*, p. 101.
- Maté, B., Rodríguez-Lazcano, Y. & Herrero, V. J., 2012. Morphology and crystallization kinetics of compact (HGW) and porous (ASW) amorphous water ice. *Physical Chemistry Chemical Physics*, 14(30), pp. 10595-10602.
- Materese, C. K., Nuevo, M. & Sandford, S. A., 2015. N- and O-heterocycles produced from the irradiation of benzene and naphthalene in H<sub>2</sub>O/NH<sub>3</sub>-containing ices. *The Astrophysical Journal*, p. 116.
- McClure, M. K. et al., 2023. An Ice Age JWST inventory of dense molecular cloud ices. *Nature astronomy*, 7(4), pp. 431-443.
- McGuire, B. A. et al., 2021. Detection of two interstellar polycyclic aromatic hydrocarbons via spectral matched filtering. *Science*, 371(6535), pp. 1265-1269.
- McKay, A. J. & Roth, N. X., 2021. Organic matter in cometary environments. *Life*, p. 37.
- McKellar, A., 1940. Evidence for the molecular origin of some hitherto unidentified interstellar lines. *Publications of the Astronomical Society of the Pacific*, pp. 187-192.

- Mejía, C. et al., 2015. Compaction of porous ices rich in water by swift heavy ions. *Icarus*, pp. 222-229.
- Miller, J. A. & Klippenstein, S. J., 2003. The recombination of propargyl radicals and other reactions on a C<sub>6</sub>H<sub>6</sub> potential. *The Journal of Physical Chemistry A*, 107(39), pp. 7783-7799.
- Mukherjee, J., Sarofim, A. F. & Longwell, J. P., 1994. Polycyclic aromatic hydrocarbons from the high-temperature pyrolysis of pyrene. *Combustion and Flame*, 96(3), pp. 191-200.
- Muniz, G., 2017. *Irradiation of aromatic heterocyclic molecules at low temperature: a link to astrochemistry*. s.l.:PhD thesis.
- Naraoka, H. et al., 2023. Soluble organic molecules in samples of the carbonaceous asteroid (162173) Ryugu. *Science*, 379(6634), p. eabn9033.
- Nastasi, M., Mayer, J. W. & Hirvonen, J. K., 1996. *Ion-solid interactions: fundamentals and applications*. s.l.:Cambridge University Press.
- Noble, J. A. et al., 2024. Detection of the elusive dangling OH ice features at ~ 2.7 μm in Chamaeleon I with JWST NIRCam. *Nature Astronomy*, pp. 1-12.
- Palumbo, M. E., 2006. Formation of compact solid water after ion irradiation at 15 K. *Astronomy & Astrophysics*, pp. 903-909.
- Pelaz, L., Marqués, L. A. & Barbolla, J., 2004. Ion-beam-induced amorphization and recrystallization in silicon. *Journal of applied physics*, pp. C. 5947-5976.
- Pilling, S. et al., 2010. Radiolysis of ammonia-containing ices by energetic, heavy, and highly charged ions inside dense astrophysical environments. *Astronomy & Astrophysics*, p. A87.
- Pino, T. et al., 2019. Release of large polycyclic aromatic hydrocarbons and fullerenes by cosmic rays from interstellar dust-Swift heavy ion irradiations of interstellar carbonaceous dust analogue. *Astronomy & Astrophysics*, Volume 623, p. A134.
- Pizzarello, S., Cooper, G. W. & Flynn, G. J., 2006. The nature and distribution of the organic material in carbonaceous chondrites and interplanetary dust particles. *Meteorites and the early solar system II*, pp. 625-651.
- Prudence, C. J. A. B., 2021. *Molécules organiques complexes sous irradiation: effets de la matrice et de la température*. Caen: PhD thesis.
- Raj, A., Prada, I. D. C., Amer, A. A. & Chung, S. H., 2012. A reaction mechanism for gasoline surrogate fuels for large polycyclic aromatic hydrocarbons. *Combustion and Flame*, 159(2), pp. 500-515.
- Rapacioli, M. et al., 2006. Formation and destruction of polycyclic aromatic hydrocarbon clusters in the interstellar medium. *Astronomy & Astrophysics*, 460(2), pp. 519-531.
- Raut, U. et al., 2007. Compaction of microporous amorphous solid water by ion irradiation. *The Journal of chemical physics*, p. 244511.
- Reames, D. V., 2021. *Solar energetic particles: a modern primer on understanding sources, acceleration and propagation*. s.l.:Springer Nature.

- Reizer, E., Viskolcz, B. & Fiser, B., 2022. Formation and growth mechanisms of polycyclic aromatic hydrocarbons: A mini-review. *Chemosphere*, Volume 291, p. 132793.
- Rothard, H. et al., 2017. Modification of ices by cosmic rays and solar wind. *Journal of Physics B: Atomic, Molecular and Optical Physics*, 50(6), p. 062001.
- Rothery, D. A., Gilmour, I. & Sephton, M. A., 2018. *An introduction to astrobiology*. s.l.:Cambridge University Press.
- Rowland, B. & Devlin, J. P., 1991. Spectra of dangling OH groups at ice cluster surfaces and within pores of amorphous ice. *The Journal of chemical physics*, pp. 812-813.
- Sandford, S. A., Nuevo, M., Bera, P. & Lee, T. J., 2020. Prebiotic astrochemistry and the formation of molecules of astrobiological interest in interstellar clouds and protostellar disks. *Chemical reviews*, pp. 4616-4659.
- Sephton, M. A. & Botta, O., 2005. Recognizing life in the Solar System: guidance from meteoritic organic matter. *International Journal of Astrobiology*, pp. 269-276.
- Smith, K. E. et al., 2014. Investigation of pyridine carboxylic acids in CM2 carbonaceous chondrites: Potential precursor molecules for ancient coenzymes. *Geochimica et Cosmochimica Acta*, pp. 1-12.
- Spohr, R., 1990. *Ion tracks and microtechnology*. Braunschweig: Friedr. Vieweg & Sohn Verlagsgesellschaft mbH.
- Strazzulla, G., Baratta, G. A., Leto, G. & Foti, G., 1992. Ion-Beam-Induced Amorphization of Crystalline Water Ice. *Europhysics Letters*, p. 517.
- Szenes, G., 1995. General features of latent track formation in magnetic insulators irradiated with swift heavy ions. *Physical Review B*, pp. 8026-8029.
- Tanabashi, M. et al., 2018. Review of Particle Physics: particle data groups. *Physical Review D*, pp. 1-1898.
- Theulé, P. et al., 2013. Thermal reactions in interstellar ice: A step towards molecular complexity in the interstellar medium. *Advances in Space Research*, pp. 1567-1579.
- Tielens, 2008. Interstellar polycyclic aromatic hydrocarbon molecules. *Annu. Rev. Astron. Astrophys.*, pp. 289-337.
- Tielens, A. G. G. M., 2013. The molecular universe. *Reviews of Modern Physics*, p. 1021.
- Toulemonde, M., Paumier, E. & Dufour, C., 1993. Thermal spike model in the electronic stopping power regime. *Radiation Effects and Defects in Solids*, 126(1-4), pp. 201-206.
- Trinkaus, H., 1997. Ion beam induced amorphization of crystalline solids: mechanisms and modeling. *Materials Science Forum*. Vol. 248. Trans Tech Publications Ltd.
- Vernhet, D. et al., 1996. Excitation in swift heavy ion-atom collisions. *Nuclear Instruments and Methods in Physics Research Section B: Beam Interactions with Materials and Atoms*, 107(1-4), pp. 71-78.

Wang, Z. G., Dufour, C., Paumier, E. & Toulemonde, M., 1994. The Se sensitivity of metals under swift-heavy-ion irradiation: a transient thermal process. *Journal of Physics: Condensed Matter*, p. 6733.

Wenzel, G., 2020. *Relaxation of Energized Polycyclic Aromatic Hydrocarbons: A Laboratory Astrophysical Study*. s.l.:Université toulouse.

Wesch, W., 2016. *Ion beam modification of solids*. s.l.:Springer Ser. Surf. Sci..

Woon, D. E., 2024. *Interstellar and Circumstellar Molecules*. [Online] Available at: [http://www.astrochymist.org/astrochymist\\_ism.html](http://www.astrochymist.org/astrochymist_ism.html) [Accessed 20 November 2024].

Wurz, P., 2005. *Solar wind composition*. s.l., s.n.

Zhen, J., Chen, T. & Tielens, A. G., 2018. Laboratory photochemistry of pyrene clusters: An efficient way to form large PAHs. *The Astrophysical Journal*, 863(2), p. 128.

Zhen, J. et al., 2019. Laboratory Formation and Photochemistry of Fullerene/Anthracene Cluster Cations. *The Astrophysical Journal*, 887(1), p. 70.

Ziegler, J. F., Ziegler, M. D. & Biersack, J. P., 2010. SRIM—The stopping and range of ions in matter. *Nuclear Instruments and Methods in Physics Research Section B: Beam Interactions with Materials and Atoms*, pp. 1818-1823.

## 2. Experimental methodology

### 2.1 Ion beam facilities

This section presents a brief overview of the ion beam facilities employed in this study. The experiments were conducted at two nuclear research centres: *Grand Accélérateur National d'Ions Lourds* (GANIL), located in Caen, France and *Atommagkutató Intézet* (ATOMKI), located in Debrecen, Hungary. Three GANIL beamlines were used in this work: *Irradiation Sud* (IRRSUD), *Sortie Moyenne Energie* (SME), and *Accélérateur pour la Recherche avec les Ions de Basse Energie* (ARIBE), with average ion energies of 1 MeV/nucleon, 10 MeV/nucleon and 100 keV, respectively. The IRRSUD and SME beamlines produce ions with energies corresponding to GCR, while the ARIBE beamline produces ions with energies corresponding to SW particles. Table 2.1 presents projectiles that were utilized for the experiments in this thesis. At GANIL, only the 90 keV  $^{16}\text{O}^{6+}$  ions correspond to SW, while the rest represent GCR. At the ATOMKI facility, the ion beams used were produced by the Tandetron accelerator, and the ions correspond to both SW and GCR particles.

Table 2.1. The projectiles used in the experiments conducted in this thesis.

Facility	Projectile	Energy, MeV	Energy, MeV/u	Average flux, $10^8$ ions/(s·cm <sup>2</sup> )
GANIL	$^{12}\text{C}^{4+}$	11.76	0.98	200
	$^{16}\text{O}^{6+}$	0.09	5.625 keV/u	5000
	$^{36}\text{Ar}^{17+}$	396.0	11.00	5
	$^{56}\text{Fe}^{10+}$	39.20	0.70	50
	$^{58}\text{Ni}^{26+}$	626.40	11.19	5
	$^{84}\text{Kr}^{15+}$	60.00	0.71	5
ATOMKI	$^1\text{H}^+$	2.00	2.00	Was not recorded
		0.20	0.20	
		0.80	0.80	
	$^4\text{He}^+$	0.40	0.10	
		0.80	0.20	
	$^{12}\text{C}^{2+}$	2.00	0.167	
		2.40	0.20	
	$^{32}\text{S}^{3+}$	4.00	0.125	
	6.40	0.20		

#### 2.1.1 GANIL

GANIL (*Grand Accélérateur National d'Ions Lourds*) is a heavy-ion accelerator, operating in Caen, France since 1983. Research is conducting in diverse fields including nuclear physics, radiobiology, material science and astrophysics. GANIL facility provides a wide range of ion beams, spanning from  $^{12}\text{C}$  to  $^{238}\text{U}$ , with maximum energy ranging from 95 MeV/u for lighter ions to 24 MeV/u for uranium beams (Chautard, 2010). The flux varies within the range of  $10^8$  to  $10^{13}$  ions/(s·cm<sup>2</sup>). The energy loss for ions from each beamline in amorphous pyridine is indicated in Figure 2.1. At ARIBE energy loss is dominated by nuclear stopping power, whereas at IRRSUD and SME electronic stopping power dominates.



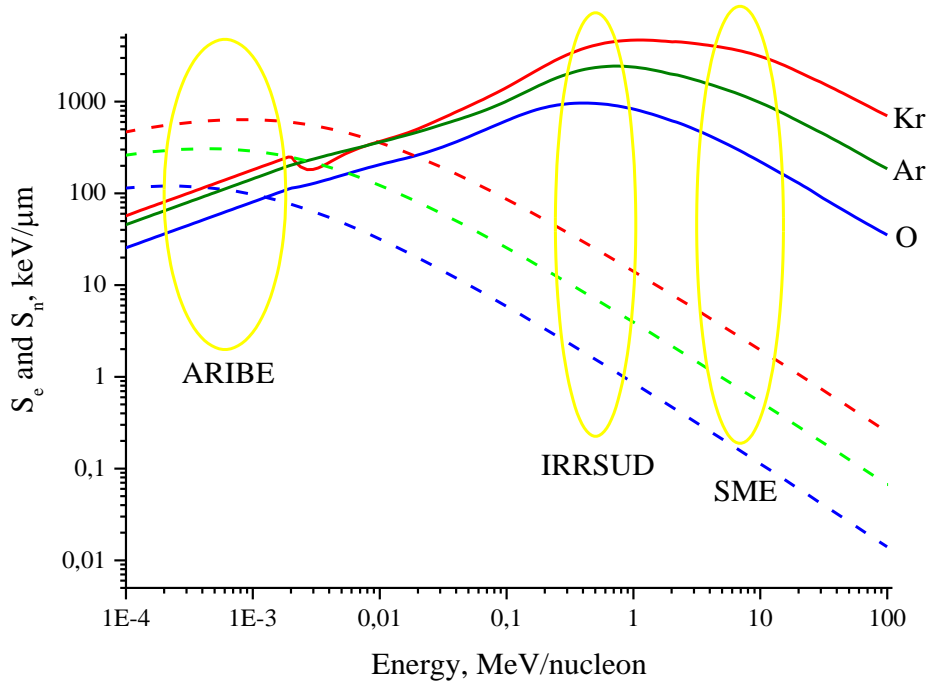


Figure 2.1. Energy ranges of ions produced in the beam lines of ARIBE, IRRSUD and SME of GANIL. The figure presents electronic stopping power  $S_e$  (solid line) and nuclear stopping power  $S_n$  (dashed line) in  $\text{keV}/\mu\text{m}$ , as a function of the projectile energy ( $\text{MeV}/\text{nucleon}$ ) for pure amorphous pyridine target ( $\rho=0.781 \text{ g}/\text{cm}^3$ ). Calculations were performed using SRIM software (Ziegler, et al., 2010).

### 2.1.1.1 IRRSUD and SME

Two high energy beamlines of GANIL were used in the experiments of this thesis: SME and IRRSUD.

Multi-charged ions are generated in the Electron Cyclotron Resonance (ECR) ion source (Figure 2.2). A gas or solid target is ionized by electrons, and the resulting ions are extracted using a high potential difference of several thousand volts. Subsequently, after leaving the source, the ions are directed to either the C01 or C02 cyclotrons.

Within these accelerators, the ion beam undergoes acceleration in a spiral path of approximately twenty turns, with an increasing radius, driven by an electric field of tens of thousands of volts per meter. The ions are bunched and injected at a frequency of approximately one ion bunch every  $\sim 100$  billionth of a second. The mass-to-electrical charge ratio of the ions plays a crucial role in influencing the acceleration and curvature of the ion trajectory, while the chemical nature has no impact on these characteristics.

The maximum energy attainable at the C01/C02 cyclotrons is  $1 \text{ MeV}/u$ . Subsequently, the beam can be delivered to the IRRSUD beamline, where ions typically have energies ranging from  $0.25$  to  $1 \text{ MeV}/\text{nucleon}$  (Hasley, 2024).

To reach higher energies, the beam is directed to CSS1 (*Cyclotron à Secteurs Séparés*), enabling ions to be accelerated to energies around  $10 \text{ MeV}/u$ .

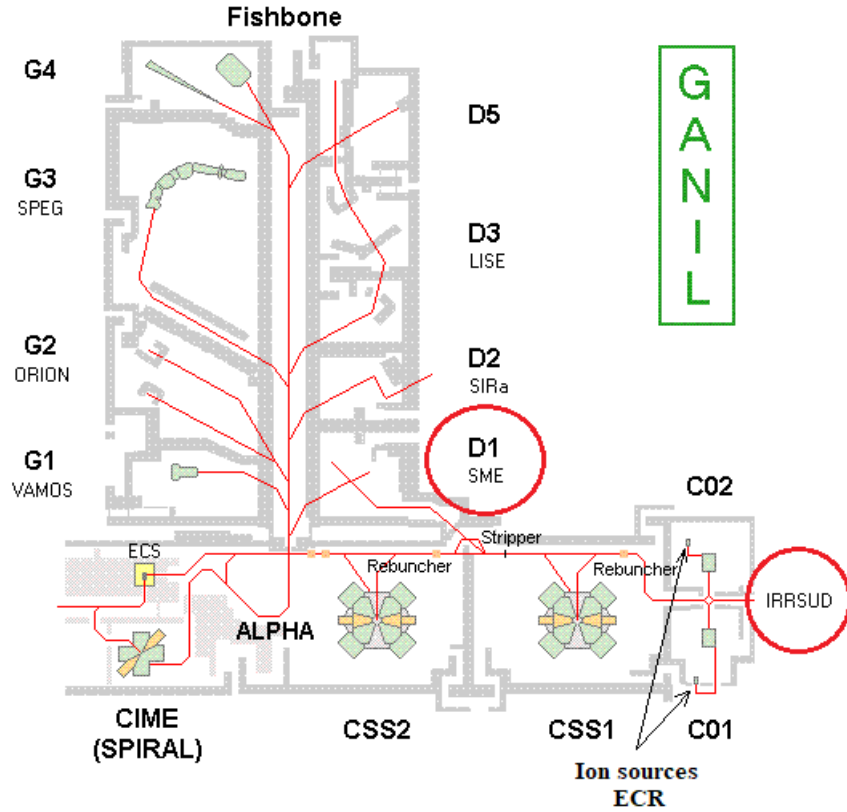


Figure 2.2. GANIL layout. Adapted from (Chautard, 2010). The beamlines used in this thesis are highlighted within the red circle.

Following the CSS1 cyclotron, a thin carbon stripper foil is employed to enhance the charge state of the ions. This stripping process introduces a distribution of charge states. Ions possessing the charge state  $q$  are directed to SME, while those with higher charges are introduced into the subsequent cyclotron, CSS2. The ion energies upon exiting CSS2 will attain several tens of MeV/u (Hasley, 2024), while the standard energies of ions delivered to the SME beam-line fall within the range of 4-13 MeV/u (Chautard, 2010).

### 2.1.1.2 ARIBE platform

Inaugurated at 2005, ARIBE (*Accélérateur pour la Recherche avec des Ions de Basse Energie*) is a platform dedicated to interdisciplinary research with low energy multi-charged ions (Figure 2.3). At very low energies, ions interact with matter through multiple electron capture processes that cause significant disruptions in the electronic system of the material.

The ECR ion source, with a working principle similar to the one delivering beams for IRRSUD and SME beamlines, produces stable ion beams over a broad range of masses (from He to Xe) and energies (5-25 keV/ $q$ ).

The ion beam can be guided and shaped by a combination of electromagnetic multipole units that apply the Lorentz force to the passing ions (green units in Figure 2.3).

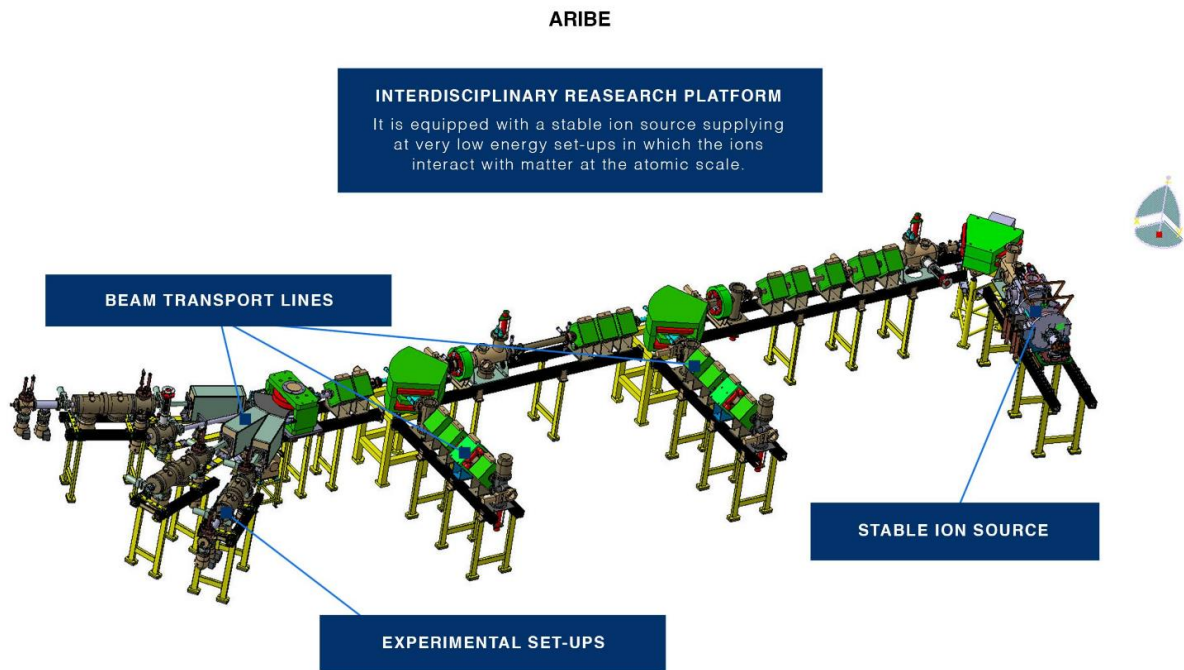


Figure 2.3. ARIBE beam-line. Extracted from (Roussel-Chomaz, 2024).

### 2.1.1.3 Flux calibration

The schematic representation of flux calibrating device is presented in Figure 2.4. To achieve a homogeneous distribution of ions across the irradiated surface, a pair of magnets is employed to sweep the ion beam both horizontally and vertically (Duarte, et al., 2009), (Ding, 2014) at SME, IRRSUD and ARIBE beamlines. A collimator is installed to ensure a parallel ion beam, and the current on the collimator will be utilized to determine the number of incoming ions. A Faraday cup is employed to measure the final current downstream of the collimator. The ratio  $\frac{I_{coll}}{I_{fc}}$  is measured before the experiments. During the experiments, the Faraday cup is removed.

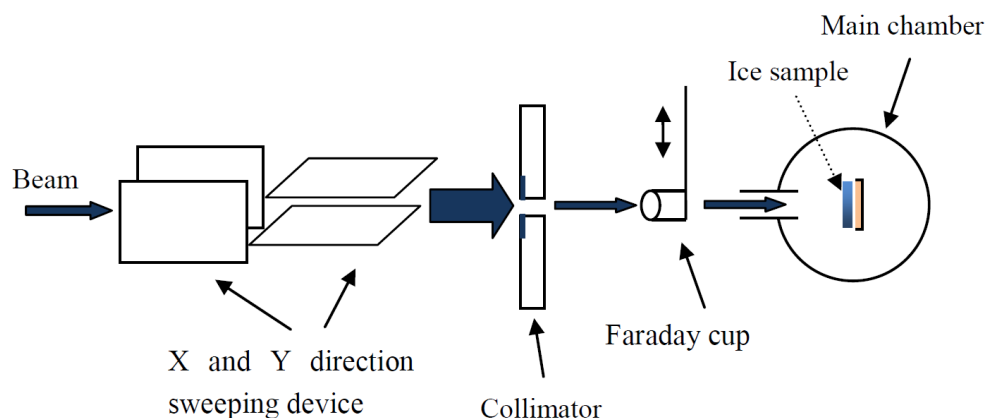


Figure 2.4. Diagram illustrating the flux calibration devices at ARIBE. Adapted from (Ding, 2014).

The total number of ions  $F$  (fluence) bombarding the sample can be calculated using the previously measured  $\frac{I_{coll}}{I_{fc}}$  ratio with the following formula:

$$F = \frac{Q}{1.6 \cdot 10^{-19} \cdot z_q \frac{I_{coll}}{I_{fc}} \cdot (\text{area of FC})} \left[ \frac{\text{ions}}{\text{cm}^2} \right], \quad \text{eq. (2.1)}$$

where  $Q$  is the current accumulated at collimator,  $z_q$  is charge of incoming ions.

### 2.1.2 ATOMKI

ATOMKI is the Institute for Nuclear Research, established in 1954. It is situated in Debrecen, Hungary. Atomki serves as a multidisciplinary research center, focusing on key research areas such as atom, nuclear, and particle physics, ion beam analytics, detection and signal processing techniques, environmental analytics, radioactive dating, radiochemistry, and solid-state physics (Máté & Rajta, 2009). The four Atomki accelerators are "small" facilities, but their wide energy range enables the conduction of numerous experiments across various fields.

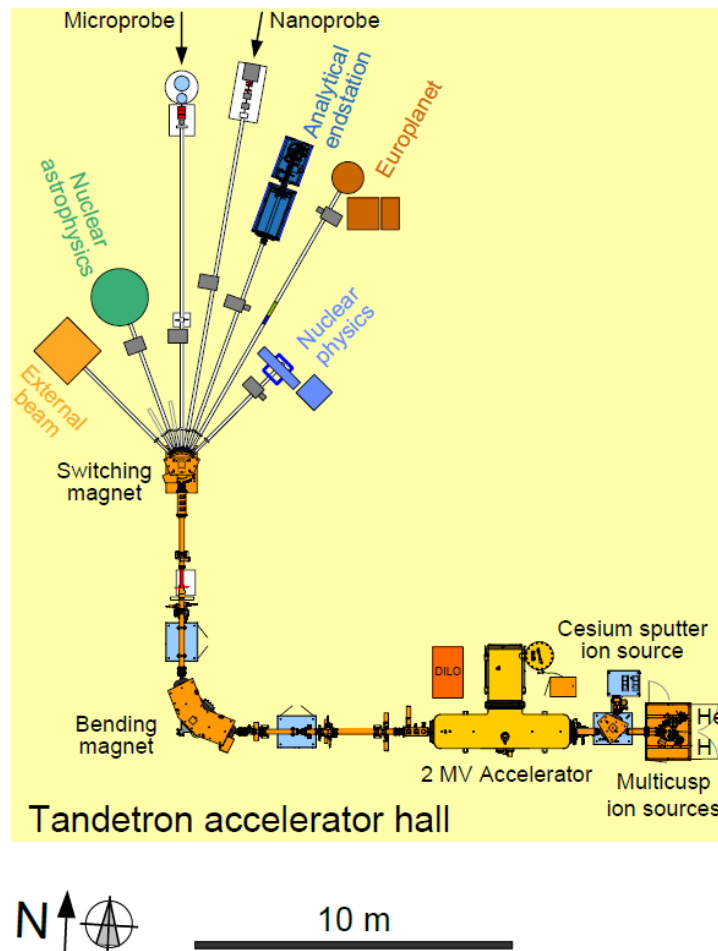


Figure 2.5. Tandatron accelerator layout. Adapted from (Biri, et al., 2021).

In this study, only the Tandatron accelerator was employed. The Tandatron accelerator beamline, installed in 2015, is capable of delivering beams of H, He, C, O, S, B, Si, Cu, and other elements with energies ranging from 0.2 to 4 MeV/u. Equipped with a cesium sputter ion source, the accelerator can also generate negative ion beams from most heavy elements.

Additionally, there are two multicusp ion sources for hydrogen and helium beams, each with a 90-degree analyzing magnet. An advantage of Tandatron is the ability to keep the multicusp and sputtering ion sources in standby mode simultaneously, allowing for quick changes in ion species or energies (Biri, et al., 2021). In Figure 2.5, the layout of the Tandatron accelerator is presented. The experiments for this study were conducted at the Europlanet beamline.

There are two main reasons why a Tandatron accelerator was used in addition to experiments conducted at GANIL. Firstly, Tandatron provides intermediate projectile energies between those available at ARIBE and SME. Additionally, Tandatron accelerate high energy light projectiles (H, He), not available at GANIL.

Figure 2.6 illustrates the ion beam irradiation system at the Europlanet beamline. Ions pass through the sweeping devices DP<sub>y</sub> and DP<sub>x</sub>, and subsequently, the beam is shaped by collimator C<sub>1</sub> into a circular form with a diameter of 14 mm. The current can be measured at Faraday cup F<sub>1</sub>, which is equipped with a second collimator reducing beam diameter to 12.6 mm. The removable cup F<sub>2</sub> enables the measurement of the current right before the beam reaches the sample, S (Herczku , et al., 2021).

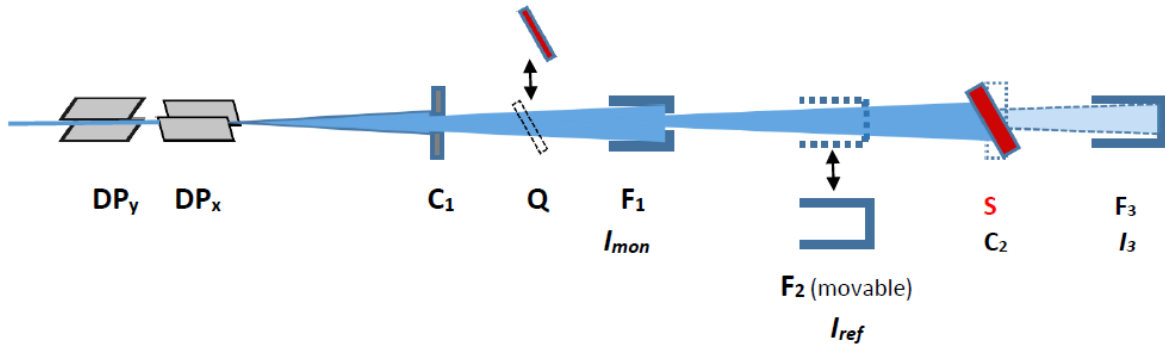


Figure 2.6. Diagram illustrating the controlled ion beam irradiation system. Extracted from (Herczku , et al., 2021).

The fluence calculated as follows: during the experiment, the total charge  $Q_{FC1}^{exp}$  ( $\mu\text{C}$ ) is measured on the Faraday cup F<sub>1</sub>. After the experiment, the Faraday cup F<sub>2</sub> is inserted into the beamline, and the ratio  $\frac{Q_{FC1}}{Q_{FC2}}$  is measured during a fixed time. The final fluence is calculated using following formula:

$$F = \frac{Q_{FC1}^{exp} \cdot 0,000001}{1,6 \cdot 10^{-19} \cdot z_q \cdot \frac{Q_{FC1} \cdot 1,13}{Q_{FC2}}} \left[ \frac{\text{ions}}{\text{cm}^2} \right], \quad \text{eq. (2.2)}$$

where 1.13 cm<sup>2</sup> is area of the Faraday cup F<sub>2</sub>.

## 2.2 Infrared spectroscopy

The main technique used in this study to investigate the evolution of the sample under irradiation is Fourier-transform infrared spectroscopy (FTIR). Infrared Spectroscopy involves the investigation of how infrared light interacts with molecules present in the sample. The molecule is exposed to a whole range of mid-infrared frequencies (wavelength range used in this study is 4000-600 cm<sup>-1</sup>). Molecules exclusively absorb radiation energy at particular

frequencies corresponding to their vibrational frequencies. While the absorption frequency relies on the molecular vibrational frequency, the absorption intensity relies on the efficiency of transferring infrared photon energy to the molecule. This efficiency depends on the change in the dipole moment of the molecule caused by molecular vibrations. In other words, to absorb infrared radiation a molecular vibration must induce a modification in the dipole moment of the molecule. This implies a limitation in the use of infrared spectroscopy. If molecule has center/plane/axis of symmetry, vibrations where the center/plane/axis of symmetry remains conserved will be infrared inactive (Colthup, 2012).

Vibrational bands of certain groups of atoms (C=N, C=C, C=O) have the same or similar frequencies, regardless of the groups surrounding them. This often allows rapid and unambiguous confirmation of the presence or absence of the fragment responsible for the vibrational band. In Figure 2.7, main vibrations of various groups of atoms with different bonds and the corresponding frequency range are listed.

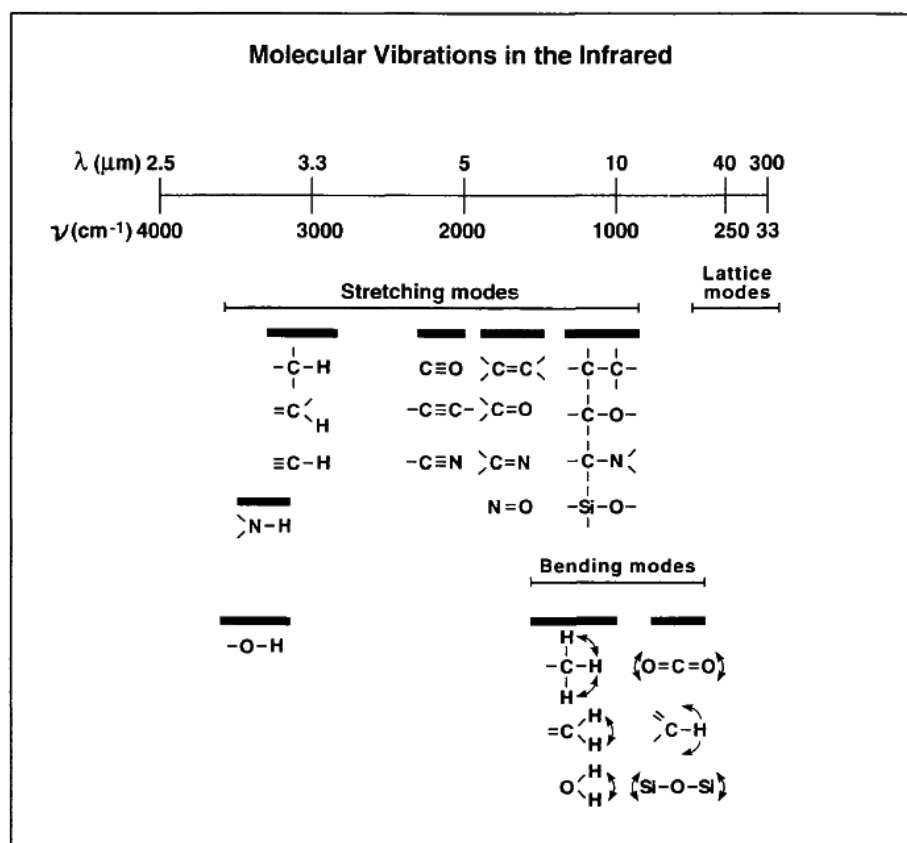


Figure 2.7. General regions of infrared spectrum, where different types of vibrational bands are observed. Extracted from (Sandford, 1996).

Figure 2.8 displays an IR spectrum of pyrene molecules in amorphous phase. The spectra was obtained at the IGLIAS setup, which will be described later. Each band corresponds to a particular vibration of the molecule (Chakraborty, et al., 2019).

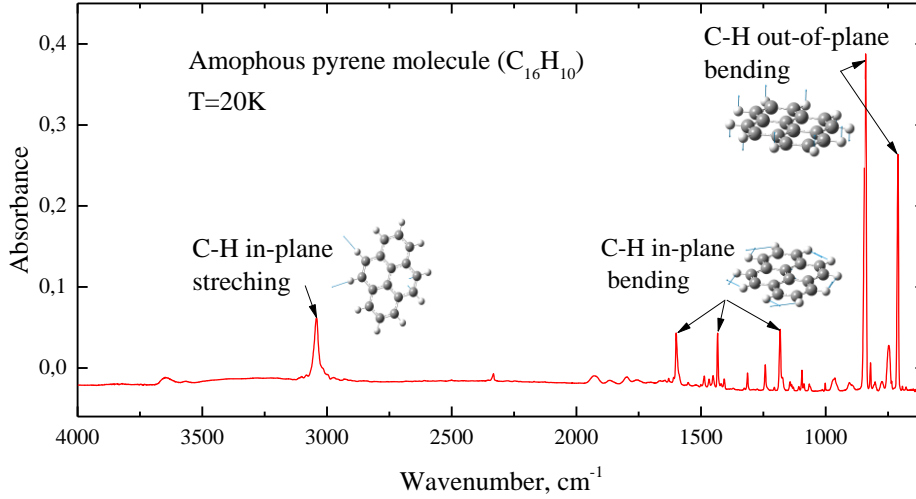


Figure 2.8. Infrared spectrum of pyrene molecule made at IGLIAS setup at  $T=20K$  with indicating the type of vibration. Pictures for vibrations extracted from (Chakraborty, et al., 2019).

IR spectroscopy also allows estimating the column density (number of molecules per  $cm^2$ ) of the molecules in the sample. The Lambert-Beer equation outlines the connection between the quantity of molecules and the intensity of absorbed light at a specific frequency (Mehta, 2012):

$$I(\lambda) = I_0(\lambda)e^{-\sigma_{ab}(\lambda)N}, \quad \text{eq. (2.3)}$$

where  $I_0(\lambda), I(\lambda)$  – intensity at a given wavenumber  $\lambda$  of infrared light before and after transmission through the sample, respectively,  $\sigma_{ab}(\lambda)$  – absorption cross section,  $N$  – column density of the sample. Transmission  $T(\lambda)$  and absorbance  $Abs(\lambda)$  can be expressed as follows:

$$T(\lambda) = \frac{I(\lambda)}{I_0(\lambda)}, \quad \text{eq. (2.4)}$$

$$Abs(\lambda) = \log_{10} \frac{I_0(\lambda)}{I(\lambda)}. \quad \text{eq. (2.5)}$$

In this study, we employed the absorption mode for data analysis. By combining the equations (2.4) and (2.5), column density  $N$  can be calculated as:

$$N = \ln 10 \frac{\int Abs(\lambda)d\lambda}{\int \sigma_{ab}(\lambda)d\lambda} = 2,3 \frac{\int Abs(\lambda)d\lambda}{Avalue} \left[ \frac{molecules}{cm^2} \right], \quad \text{eq. (2.6)}$$

where  $\int Abs(\lambda)d\lambda$  is area of selected absorption band at IR spectra;  $\int \sigma_{ab}(\lambda)d\lambda$  is band strength or *A-value* of a given vibration mode, quantifies how strongly a particular vibrational mode of a molecule interacts with electromagnetic radiation. *A-values* were not calculated in this study, they were extracted from existing literature sources. Equation (2.6) signifies that the column density is directly proportional to the area of the absorption peak.

By knowing the column density, it is possible to determine the sample thickness from the formula:

$$h = \frac{N \cdot M}{\rho \cdot N_A} \quad [\text{cm}], \quad \text{eq. (2.7)}$$

where  $M$  is molar mass (g/mol),  $\rho$  is density of the sample (kg/m<sup>3</sup>),  $N_A = 6.02 \cdot 10^{23}$  is the Avogadro constant (mol<sup>-1</sup>).

Furthermore, another parameter that we will use in order to assess the radiolysis is local dose:

$$L_D = \frac{h \cdot (S_e + S_n) \cdot F}{N_0}, \quad \left[ \frac{\text{eV}}{\text{molecule}} \right] \quad \text{eq. (2.8)}$$

where  $S_e, S_n$  are the electronic and nuclear stopping powers (eV/μm) of the projectile, respectively,  $N_0$  is the initial column density of the sample (at  $F=0$ ),  $F$  is the ion fluence (ions/cm<sup>2</sup>).

## 2.3 Experimental setup

This section provides a brief overview of the equipment used for conducting the experiments. The primary objective of the experimental setups is to reproduce space conditions and monitor the sample's evolution under various exposures.

### 2.3.1 CASIMIR

A detailed description of CASIMIR was made earlier in the following works (Muniz, 2017), (Auge, 2017), (Seperuelo Duarte, 2009). Here, only a brief overview will be provided.

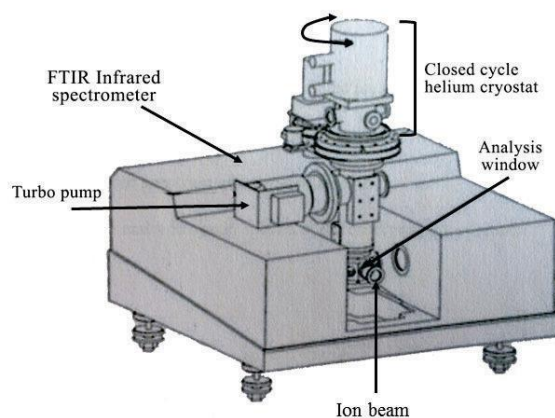


Figure 2.9. Scheme of CASIMIR. Extracted from (Muniz, 2017).

CASIMIR (French acronym from **C**hambre d'**A**nalyse par **S**pectroscopie **I**nfrarouge des **M**atériaux **I**Rradiés), presented at Figure 2.9, was constructed at the middle of 1990. This setup could be installed at both IRRSUD and SME beamlines. The CASIMIR comprises a high-vacuum chamber with a sample holder inside, a cryogenic cold head, a Fourier-Transform infrared spectrometer (Nicolet Magna 550), and a ramp for mixture preparation. This set-up enables the preparation of ice mixtures containing various molecules and the monitoring of their chemical evolution during irradiation using infrared spectroscopy.



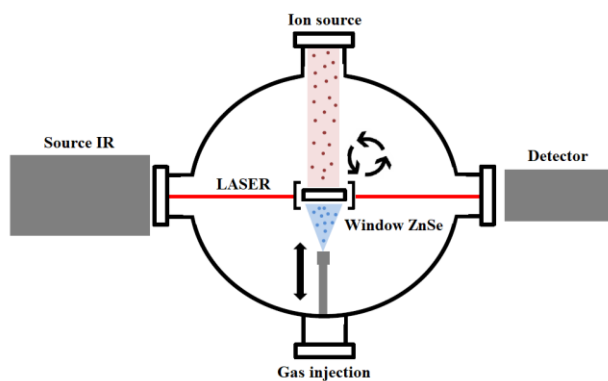


Figure 2.10. Top view on the inside of the CASIMIR chamber. Adapted from (Auge, 2017).

The sample holder with one window is connected to a helium cryostat, operating in a closed cycle. The cryostat enables maintaining the temperature of the sample holder within the range from 12 to 300 K. The minimum achievable pressure in the chamber using both a primary and a turbomolecular pump at ambient temperature is around  $10^{-7}$  mbar and  $10^{-8}$  mbar at 12 K. During deposition, the pressure in the chamber rises to around  $10^{-6}$  mbar.

The sample is obtained by condensing molecules via a nozzle from the ramp onto a cold window. The cryostat with the sample holder can be rotated. Irradiations are conducted at  $0^\circ$ , IR spectra are acquired at  $90^\circ$ , and gas deposition takes place at  $180^\circ$ , as illustrated in Figure 2.10.

### 2.3.2 IGLIAS

IGLIAS (Auge, 2017) (Augé, et al., 2018) (French acronym: **I**rradiation de **GL**aces d'Intérêt **AS**trophysique) is an improved version of CASIMIR. IGLIAS represents an experimental set-up designed for the investigation of radiation-induced damage on different samples, which could be mounted on different beam lines at GANIL facility. Most of the experiments in this thesis were performed on the IGLIAS setup. In this thesis for experiments that were done at IGLIAS setup at the IRRSUD beam line.

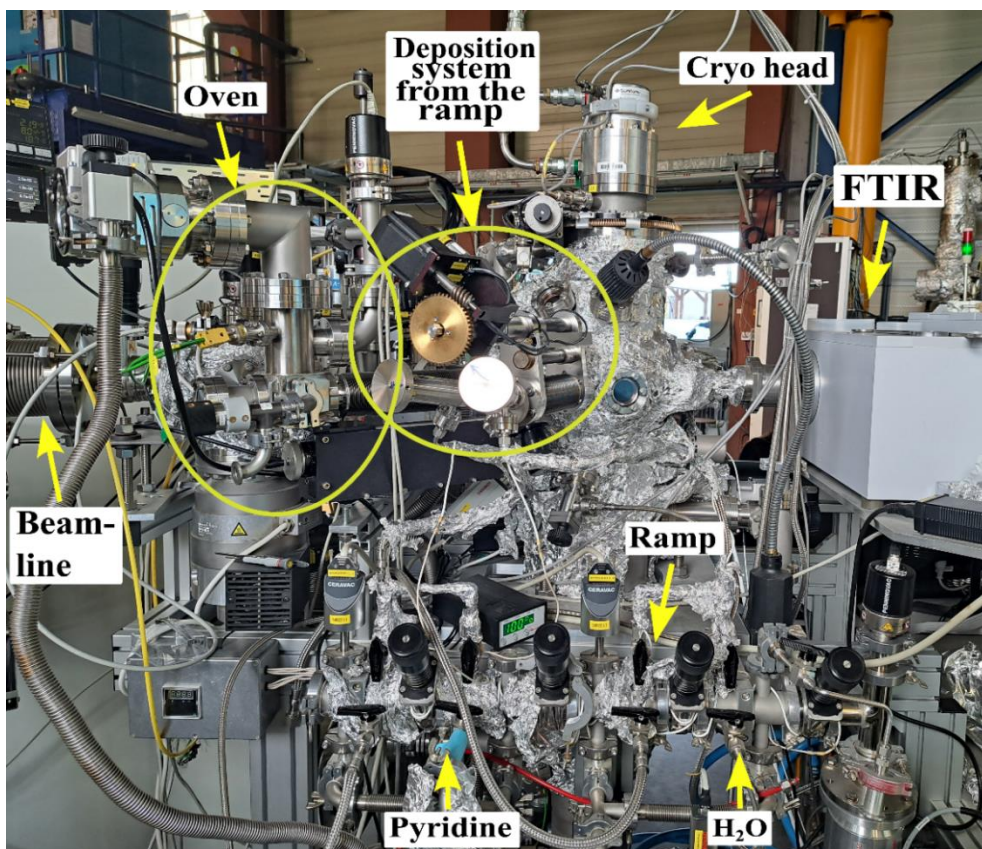


Figure 2.11. Photo of IGLIAS.

IGLIAS, presented in Figure 2.11, comprises an ultra-high vacuum chamber, a cryohead with an attached sample holder; an infrared spectrometer (Brucker Vertex 70v), which is capable to record spectra from  $500$  to  $6000\text{ cm}^{-1}$ , a ramp for preparing molecular mixtures, and an oven. IGLIAS is equipped with three windows, allowing for an increased number of experiments compared to CASIMIR without opening the chamber. The spectral resolution was  $1\text{ cm}^{-1}$ . The pumping system of IGLIAS achieves an ultra-high vacuum of approximately  $10^{-10}$  mbar at  $10\text{ K}$ .

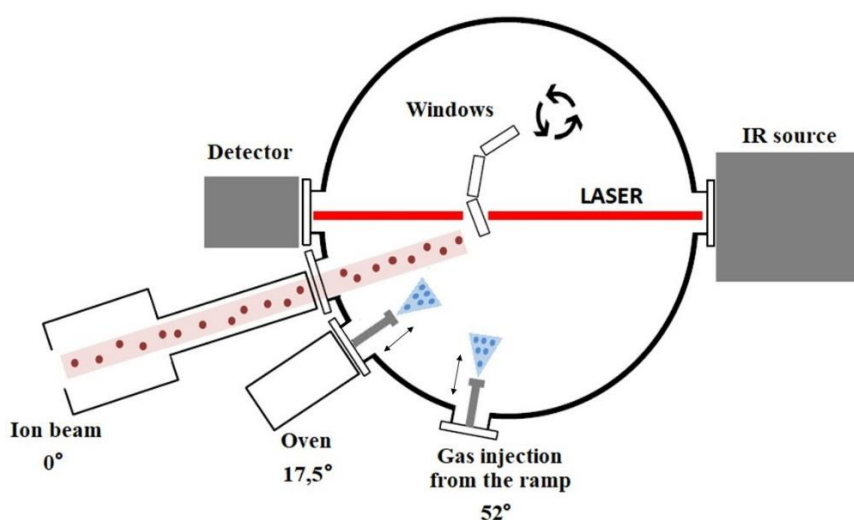


Figure 2.12. Top view on the IGLIAS chamber. Adapted from (Augé, et al., 2018).

Similar to CASIMIR, samples are prepared by gas condensation onto one of the windows. A closed-cycle helium cryohead connected to the sample holder can cool the windows to temperatures ranging from 300K to 10K. Temperature control of the windows is achieved using two thermoresistors: one is more accurate at low temperatures, while the other is more precise at high temperatures. The molecules under investigation are deposited either from the ramp via nozzles (gas phase), or from an oven (powders), as illustrated in Figure 2.12. Several tubes containing different molecules can be connected to the ramp and then be mixed in specific proportions. The injection nozzle of the ramp moves in close proximity to the window, and the injection is performed by opening a micrometric valve. By comparing the pressure in the ramp before and after deposition, it is possible to estimate the quantity of gas released into the vacuum chamber. The pressure in the vacuum chamber during deposition rises up to around  $3 \cdot 10^{-7}$  mbar.

Molecules that are solid at room temperature and have high vapour pressure can be deposited into the vacuum chamber from the oven. This oven has recently been installed at IGLIAS, and a detailed description of it is presented in the next subsection (2.3.2.1). The pressure in the vacuum chamber during deposition from the oven depends on the temperature inside the oven and typically falls to about  $10^{-8}$  mbar at 10 K.

After deposition, the windows are rotated to the irradiation position, which coincides with the position for acquiring the infrared spectrum. This functionality enables experiments to be conducted in automatic mode, eliminating the need to manually rotate the windows after each irradiation step as in CASIMIR. During automatic mode, human intervention is not required, as the ions bombard the sample and infrared spectra are acquired at predetermined time intervals. The only time constraint in the automatic mode is that the infrared detector must be cooled with liquid nitrogen to be refilled approximately every 6 hours.

### 2.3.2.1 Oven

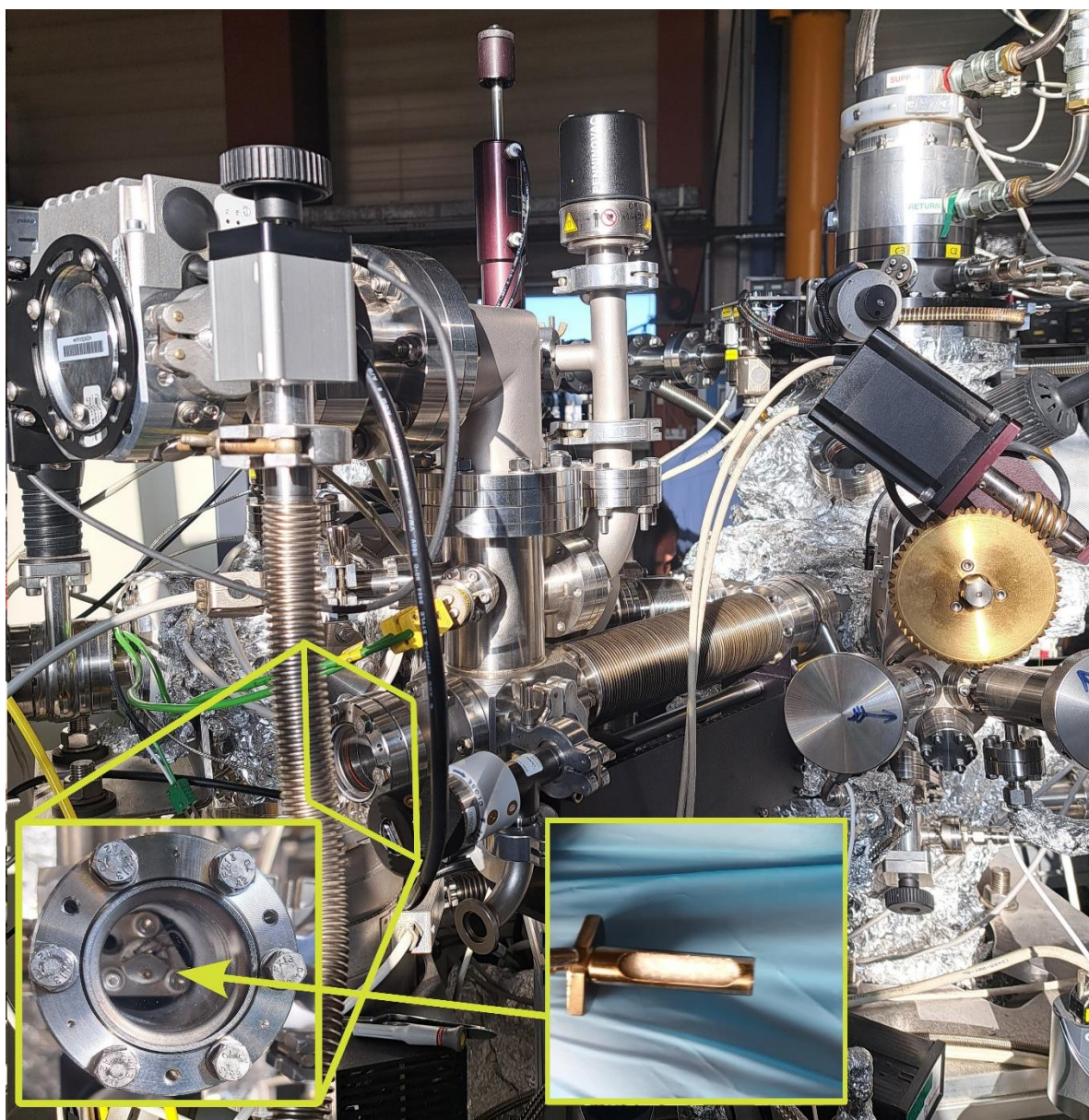


*Figure 2.13. Photo of the oven.*

The oven, shown in Figure 2.13, was installed at IGLIAS in 2022. It was specifically designed to facilitate the deposition of molecules that are in a solid phase at room temperature. The operating principle is as follows: after loading the powder of the investigated molecules into the evaporator (Figure 2.14), the oven is pumped by primary and turbo pumps. The pressure typically drops to  $10^{-6}$  mbar. The oven is heated by three heating elements, which are located on the evaporator, on the screen and on the tube. The temperature can be monitored at two points: the first thermocouple is positioned inside the evaporator, 15 mm from the evaporator end (pointer at the left bottom picture in Figure 2.13), and the second is located at the middle of the tube.

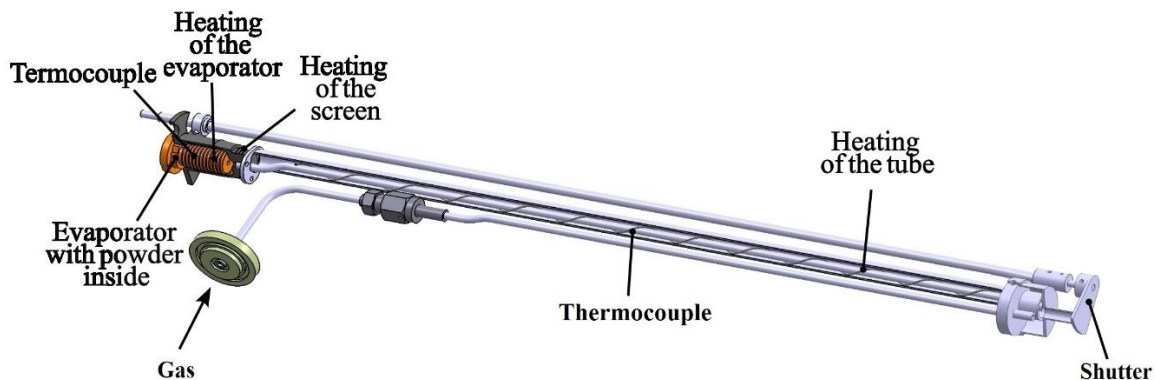


Figure 2.14. Schematic view of the interior of the oven.

Each heating element has its own power supply, and the current is adjusted to ensure that the temperature at both thermocouples is approximately equal. The resistances of the elements are approximately 6.3 Ohm for the evaporator, 3.6 Ohm for the screen, and 11.3 Ohm for the tube. Deposition takes place when the tube is within a minimum distance of 10 mm from the window and the shutter is in the open position. The position of the shutter is externally controlled using a lever.

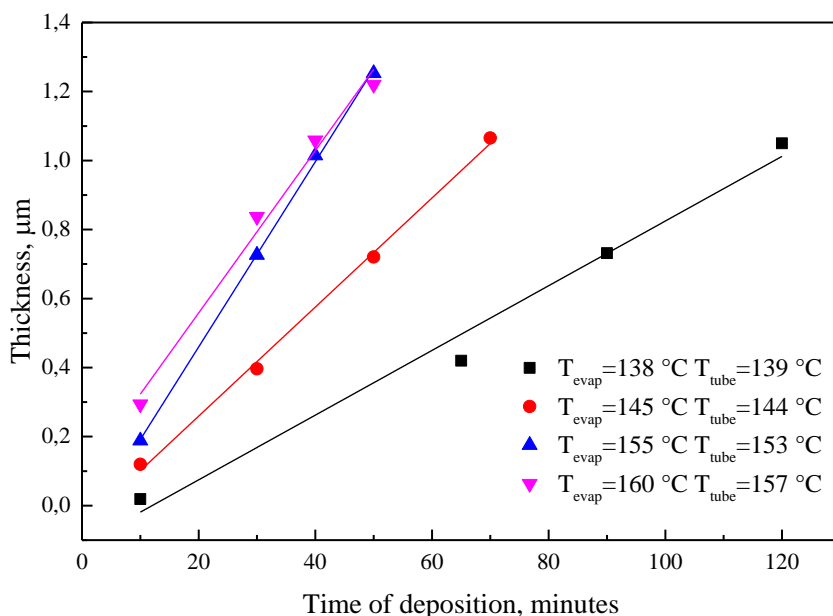


Figure 2.15. Thickness of pyrene as a function of deposition time at different heating temperatures.

The rate of the deposition from the oven usually depends on the heating temperature. In Figure 2.15, the thickness of pyrene is presented as a function of deposition time for various thermocouple temperatures. The higher the temperature, the more molecules transition into the gas phase, resulting in a faster deposition rate. However, increasing the temperature should be done with caution, as the powder can easily be burned.

### 2.3.3 ICA setup

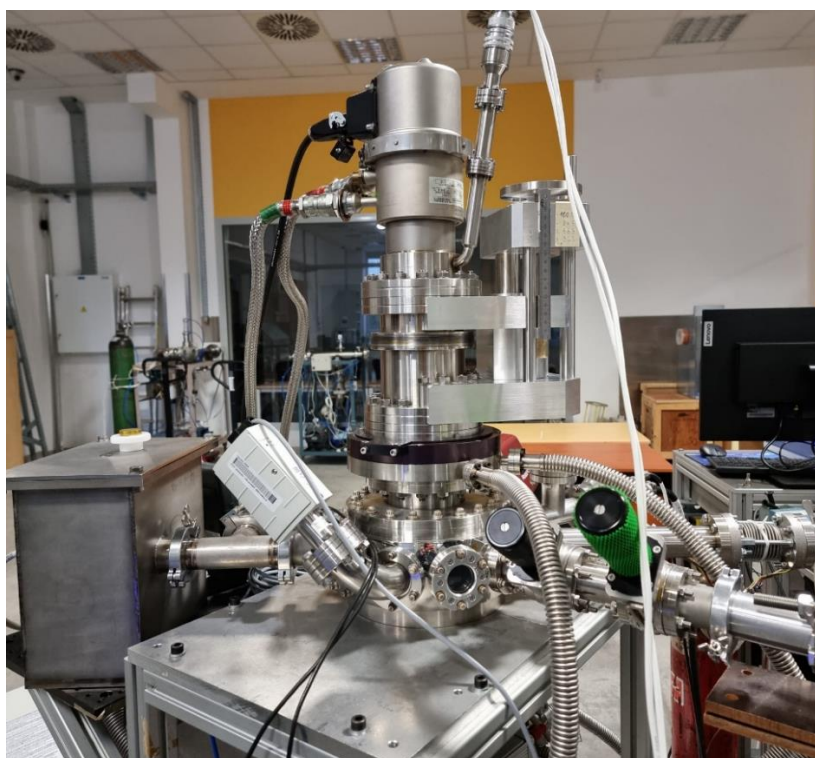


Figure 2.16. Photo of ICA chamber.

The ICA (Ice Chamber for Astrophysics-Astrochemistry) (Herczku , et al., 2021), presented in figure 2.16, is a novel setup situated at the Institute for Nuclear Research (ATOMKI) in Debrecen, Hungary. Top-view schematic representation of ICA is illustrated in Figure 2.17. ICA comprises a high-vacuum chamber with a base pressure of  $10^{-9}$  mbar, a cryohead with an attached sample holder, a ramp, an oven, and an infrared spectrometer. The spectral resolution was  $2\text{ cm}^{-1}$ .

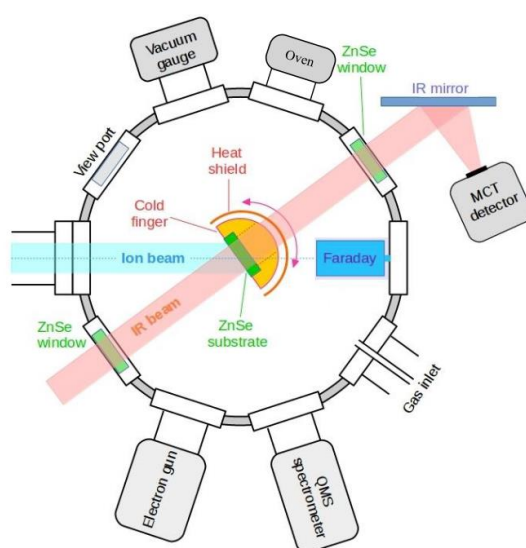


Figure 2.17. A top-view schematic diagram of the ICA chamber. Adapted from (Herczku , et al., 2021).

The samples are arranged vertically, and the sample holder moves along the vertical axis of the chamber. This arrangement enables four independent irradiations under identical conditions. The sample holder has the capability to rotate around a vertical axis as well, facilitating deposition on the sample from solid powders or liquids. Additionally, this rotation capability enables the processing of the sample with different exposures.

The majority of experiments with pyrene were conducted using this setup. Since pyrene is solid at room temperature, a commercial oven OLED Effusion Cell was used to prepare the samples. Pyrene was heated in the oven to around 50 °C and subsequently deposited onto a pre-cooled window inside the chamber. The distance between the tube outlet and the window is approximately 10 mm. Deposition of pure pyrene typically took 5-15 minutes for samples with thicknesses ranging from 0.8 to 1.1  $\mu\text{m}$ . Meanwhile, the deposition of the pyrene mixtures with water take 10-40 minutes, with sample thicknesses ranging from 0.1 to 0.9  $\mu\text{m}$ . The typical pressure in the chamber during irradiation is approximately  $10^{-8}$  mbar, and during depositions, it drops to around  $3 \cdot 10^{-7}$  mbar. The temperature of the sample holder was maintained at 20 K during both deposition and irradiation in all experiments. The infrared beam is oriented perpendicular to the sample, while the ion beam is positioned at a  $36^\circ$  angle from the perpendicular. This factor was considered in the calculation of the fluence of the incident ions.

## References

- Auge, B., 2017. *Effets du rayonnement cosmique galactique sur les petits corps glacés du système solaire externe : indices pour la formation de la matière organique des micrométéorites antarctiques ultracarbonées*. s.l.:PhD thesis.
- Augé, B. et al., 2018. IGLIAS: A new experimental set-up for low temperature irradiation. *Review of Scientific Instruments*, 89(7).
- Biri, S., Vajda, I., Hajdu, P. & Rácz, R., 2021. The atomki accelerator centre. *The European Physical Journal Plus*, 136(2), p. 247.
- Chakraborty, S., Mulas, G., Demyk, K. & Joblin, C., 2019. Experimental Approach to the Study of Anharmonicity in the Infrared Spectrum of Pyrene from 14 to 723 K. *J Phys Chem A*, 123(19), pp. 4139-4148.
- Chautard, F., 2010. *GANIL Operation Status and Developments*. Lanzhou,China, CYCLOTRONS.
- Colthup, N., 2012. *Introduction to infrared and Raman spectroscopy*. s.l.:Elsevier.
- Ding, J.-J., 2014. *Irradiation de glace d'eau et implications astrophysiques*. s.l.:PhD thesis: Normandy University.
- Duarte, E. S. et al., 2009. Heavy ion irradiation of condensed CO: sputtering and molecule formation. *Astronomy & Astrophysics*, pp. 599-603.
- Hasley, D., 2024. *Centre de recherche sur les Ions, les MAériaux et la Photonique*. [En ligne] Available at: <https://cimap.ensicaen.fr/?lang=fr>
- Herczku, P. et al., 2021. The Ice Chamber for Astrophysics–Astrochemistry (ICA): A new experimental facility for ion impact studies of astrophysical ice analogs. *Review of Scientific Instruments*, 92(8).
- Máté, . Z. & Rajta, I., 2009. *Institute of Nuclear Research of the Hungarian Academy of Sciences*, Debrecen: Bouklet.
- Mehta, A., 2012. *Ultraviolet-Visible (UV-Vis) Spectroscopy – Derivation of Beer-Lambert Law*. [En ligne] Available at: <https://pharmaxchange.info/2012/04/ultraviolet-visible-uv-vis-spectroscopy-%e2%80%93-derivation-of-beer-lambert-law/>
- Muniz, G., 2017. *Irradiation of aromatic heterocyclic molecules at low temperature: a link to astrochemistry*. s.l.:PhD thesis.
- Reusch, W., 2013. *Infrared Spectroscopy*. [En ligne] Available at: <https://www2.chemistry.msu.edu/faculty/reusch/virttxtjml/spectrpy/infrared/infrared.htm>
- Roussel-Chomaz, P., 2024. *Virtual tour of the Grand Accélérateur National d'Ions Lourds*. [En ligne] Available at: <https://www.ganil-spiral2.eu/>



Sandford, S. A., 1996. The inventory of interstellar materials available for the formation of the solar system. *Meteoritics & Planetary Science*, 31(4), pp. 449-476.

Seperuelo Duarte, E., 2009. *Estudo por espectrometria de infravermelho dos efeitos da irradiação de gelos astrofísicos por ions pesados e rápidos*. s.l.:PhD thesis.

Ziegler, J. F., Ziegler, M. D. & Biersack, J. P., 2010. SRIM—The stopping and range of ions in matter. *Nuclear Instruments and Methods in Physics Research Section B: Beam Interactions with Materials and Atoms*, pp. 1818-1823.

### 3. Ion irradiation of pyridine ice

Pyridine is a heterocyclic aromatic molecule with the chemical formula  $C_5H_5N$ . Structurally, it is related to benzene, with a CH group replaced by a nitrogen atom (Figure 3.1). Pyridine derivatives play a crucial role in biological processes. They act as catalysts for many biochemical reactions and can target a variety of biological problems by interacting with proteins, enzymes and DNA (Altaf, et al., 2015). In addition, a large number of nitrogen heterocycles are components of RNA and DNA. All of this makes pyridine of great interest for the study of the origin of life and astrobiology.

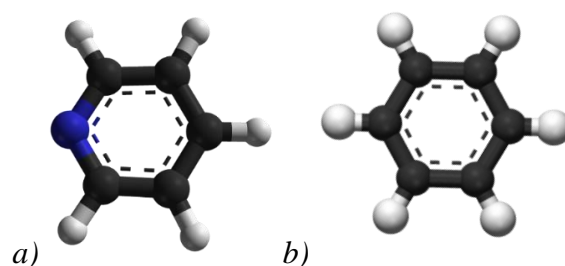


Figure 3.1. Scheme of a) pyridine and b) benzene molecule.

Pyridine has not yet been detected in space; however, studies suggest its potential formation from molecules identified in space. (Morales, et al., 2011) and (Sun, et al., 2014) demonstrated the possibility of pyridine formation through the reaction of cyano radical (CN) and 1,3-butadiene ( $C_4H_6$ ) at low temperature. (Materese, et al., 2015) detected pyridine in residues after UV irradiation of a benzene-water-ammonia ice mixture, while benzene has been detected in the interstellar medium (Cernicharo, et al., 2001). Additionally, the presence of pyridine derivatives in carbonaceous chondrites discovered in Antarctica (Smith, et al., 2014) supports this hypothesis. Therefore, it is crucial to investigate the behaviour of pyridine under astrophysical conditions, specifically its radiolysis under different types of ionizing radiation, in order to predict its survivability and its interactions with other species, present in space.

Several studies had been dedicated to pyridine radiolysis in the solid phase. During the experiment involving electron irradiation of pyridine- $CO_2$  ice (McMurtry, et al., 2016), the same pyridinecarboxylic acids, including niacin, an essential human nutrient, were identified as those found in Murchison and Tagish Lake meteorites, as well as in CM2-type meteorites. Additionally, amorphous pure pyridine was irradiated at GANIL with CASIMIR with different heavy ions: 116 MeV  $U^{32+}$  (Muniz, 2017), 650 MeV  $^{70}Zn^{26+}$  and 90 keV  $^{16}O^{6+}$  (Bibang, et al., 2021), (Bibang, 2021). They found that destruction cross section of pyridine (see section 1.3.2.3) exhibits a power dependence on the electronic stopping power of the projectile, with power coefficient close to 1 (1,07), indicating that the dependence is nearly linear. Also (Muniz, 2017) conducted time-of-flight measurements of the secondary cation emission while pure pyridine irradiated with 90 keV  $^{16}O^{6+}$ . He found that the most abundant cation fragment is  $C_5H_5N^+$ , followed by  $C_4H_4^+$  (or  $C_3H_3N^+$ ), and then  $(Py)^{+2}$ . Additionally, (Bibang, et al., 2021) and (Bibang, 2021) studied the influence of the water matrix on pyridine destruction at low temperature. They found that the probability of pyridine destruction increases with a decrease in the pyridine concentration in the mixture, regardless of the projectile. The infrared spectrum

and corresponding band strengths of pyridine molecule were reported in (Hudson & Yarnall , 2022).

However, there are still unsolved problems. It is well established, that crystalline ice has been identified in various extraterrestrial environments (Jewitt & Luu, 2004), (Hansen & McCord, 2004), (Cable, et al., 2021). Therefore, it is necessary to determine whether the crystalline structure of water matrix and pyridine itself affect the radiolysis of pyridine. It is also important to understand the influence of temperature on the radioresistance of pyridine.

This chapter will serve as a continuation of the works (Muniz, 2017), (Bibang, 2021) and (Bibang, et al., 2021). We investigated the radiolysis of pure pyridine and pyridine-water mixtures with different initial structures (amorphous/crystalline), irradiated at different temperatures with heavy ions 396 MeV  $^{36}\text{Ar}^{17+}$ , 626,4 MeV  $^{58}\text{Ni}^{26+}$ , 61,3 MeV  $^{84}\text{Kr}^{15+}$  and 90 keV  $^{16}\text{O}^{6+}$ . Experiments were conducted at GANIL facility.

### 3.1 Sample preparation

Experiments with pyridine were carried out with both IGLIAS and CASIMIR. The procedure for preparing mixtures and depositing samples is similar for both setups. Pyridine is liquid at room temperature, and its vapour pressure, similar to that of water, is 25.6 mbar at 25 °C (Herington & Martin, 1953). The tubes containing liquid pyridine (Sigma-Aldrich, purity 99.8%) and water were connected to the ramp. Subsequently, the liquids undergo multiple freeze-thaw cycles using liquid nitrogen, followed by pumping, to ensure the extraction of the volatile contaminants.

A certain quantity of pyridine vapour from the tube was introduced into the ramp before the deposition. In the case of preparing a pyridine-water mixture, water was also introduced into the ramp. The pyridine-water ratio was set by pressure measurements (barocel) in the ramp. Deposition begins by opening a fine valve, when the deposition tube is at the closest position to the window (around 10 mm). The precise ratio of water to pyridine is determined using the IR spectrum of the deposited sample.

To prepare amorphous samples, pyridine was deposited at low temperature of 10-15 K. At this temperature, molecules form a disordered amorphous structure when they condense at the window. Crystalline samples of pure pyridine were prepared at 130 K, since pyridine begins to crystallize above 120 K, and sublimation occurs above 160 K (Hudson & Yarnall , 2022). At higher temperature when molecules condense, they retain some energy to oscillate until they reach a position of minimum energy in relation to neighbouring molecules. Crystalline samples of pyridine – water mixtures were prepared when temperature of the sample holder was 150 K. The increase in temperature by 20 degrees is related to the fact that water has crystalline structure at 150 K (Kofman, et al., 2019). The time of deposition typically took from 5 to 40 minutes, depending of the required sample thickness and pressure in the ramp.

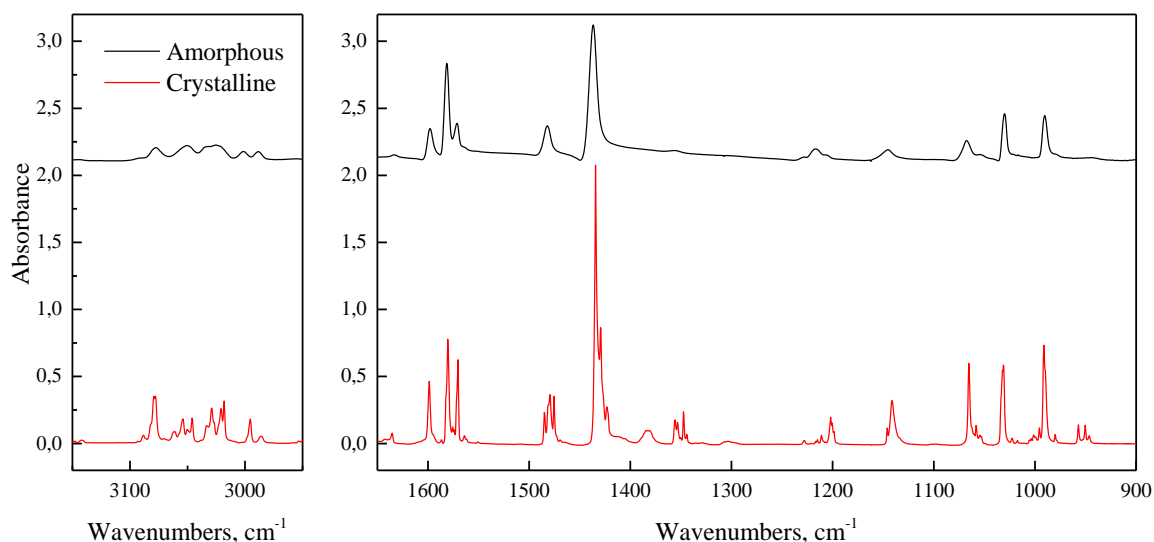


Figure 3.2. Infrared spectrum of crystalline (red) and amorphous (black) pure pyridine. The spectra were acquired with CASIMIR setup at 15 K.

It was reported in the literature that crystalline structure distinguishes itself from the amorphous one with sharpening and splitting of the peaks (Moore & Hudson, 1994), (Hudson & Yarnall, 2022). These changes in the IR spectrum are attributed to the geometric restrictions imposed on the molecules within the crystalline lattice (Timón, et al., 2021). In Figure 3.2 the IR spectra of amorphous and crystalline pure pyridine are presented.

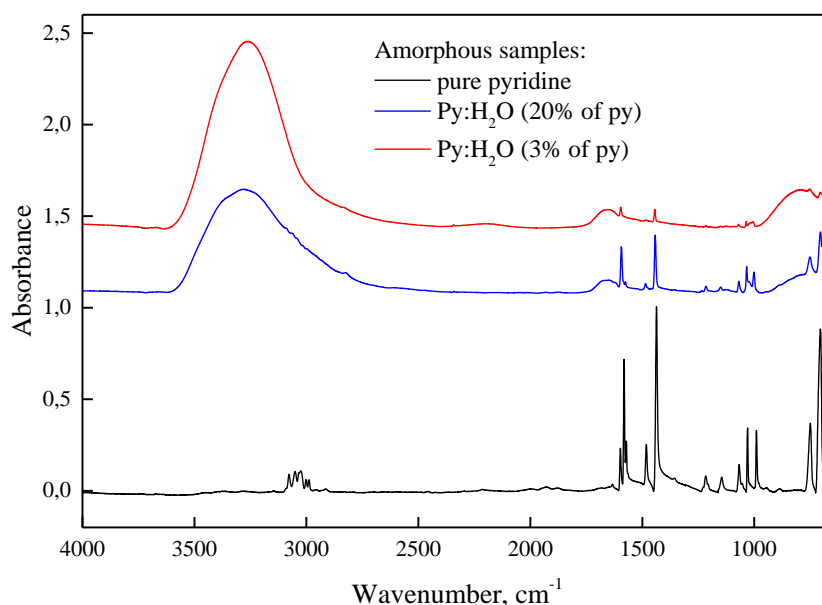


Figure 3.3. IR spectra of amorphous samples. Pure pyridine – black line, Py:H<sub>2</sub>O (20% of pyridine) – blue line, Py:H<sub>2</sub>O (3% of pyridine) – red line. The spectra were obtained at 15 K with CASIMIR setup.

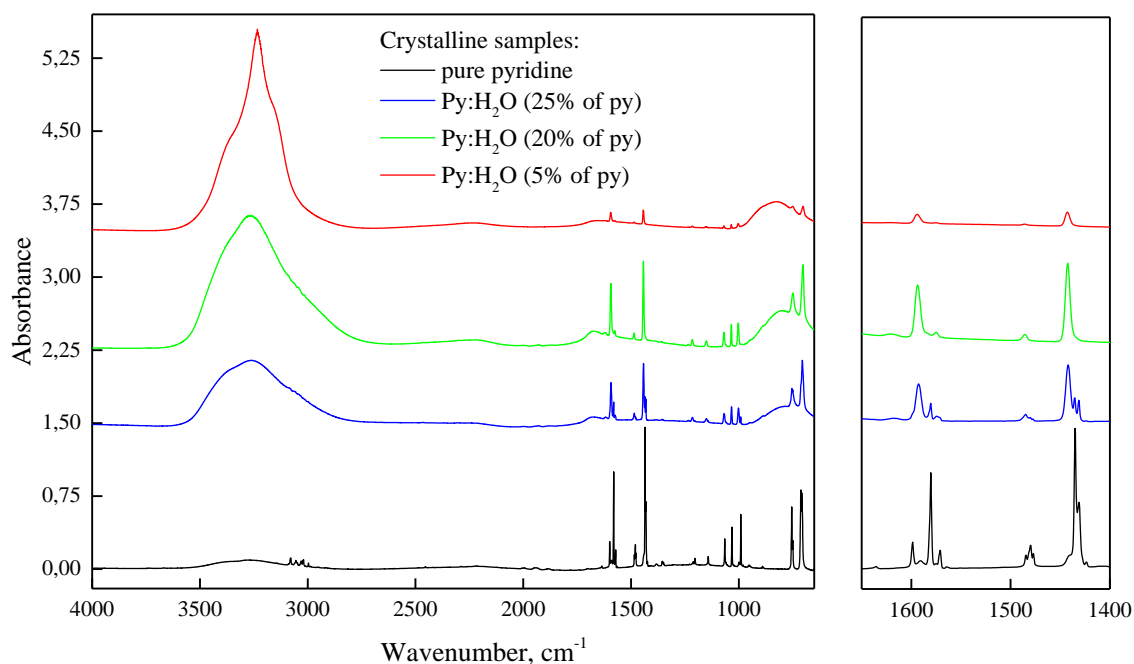


Figure 3.4. IR spectra of crystalline samples. Pure pyridine – black line, Py:H<sub>2</sub>O (25% of Py) – blue line, Py:H<sub>2</sub>O (20% of Py) – green line, Py:H<sub>2</sub>O (5% of Py) – red line. The spectra were acquired with the IGLIAS setup at 150 K.

Figure 3.3 displays infrared spectra of amorphous pyridine – water mixtures, with different pyridine concentrations, obtained at CASIMIR setup. Figure 3.4 displays infrared spectra of crystalline samples of pyridine – water mixtures obtained with IGLIAS. An important feature was observed during preparation of crystalline samples: pyridine forms a crystalline structure only at the concentrations in the mixture equal to or exceeding 25%. This can be discerned by comparing two lines in Figure 3.4 – green (20% of pyridine) and blue (25% of pyridine), the multiple peaks are still present in blue spectrum, but absent in green one. This phenomenon can be explained by the fact that crystalline clusters of pyridine cannot be formed at lower concentrations, as water molecules interfere with the pyridine crystalline lattice (Figure 3.5a), disrupting its order and leading to the formation of an amorphous structure. (Feng, et al., 2021) reported a computational study, where the authors showed that the pyridine molecule orients its nitrogen atom towards the water molecule (Figure 3.5b), leading to the formation of a hydrogen bond. The same phenomenon occurs with water, with concentrations of pyridine higher than 20% the sharp water band becomes smoother (Figure 3.4).

Tables 3.1 and 3.2 present vibrational modes of amorphous/crystalline pyridine and water with corresponding band strengths (*A*-values) and assignments in the wavenumber range from 500 to 5000 cm<sup>-1</sup>. The density of amorphous pyridine is 0.781 g/cm<sup>3</sup>, while the density of crystalline pyridine is 1.149 g/cm<sup>3</sup> (Hudson & Yarnall, 2022). The density of amorphous and crystalline water ice is 0.94 g/cm<sup>3</sup> (Ghormley & Hochanadel, 1971) and 0.93 g/cm<sup>3</sup> (Feistel & Wagner, 2006), respectively.

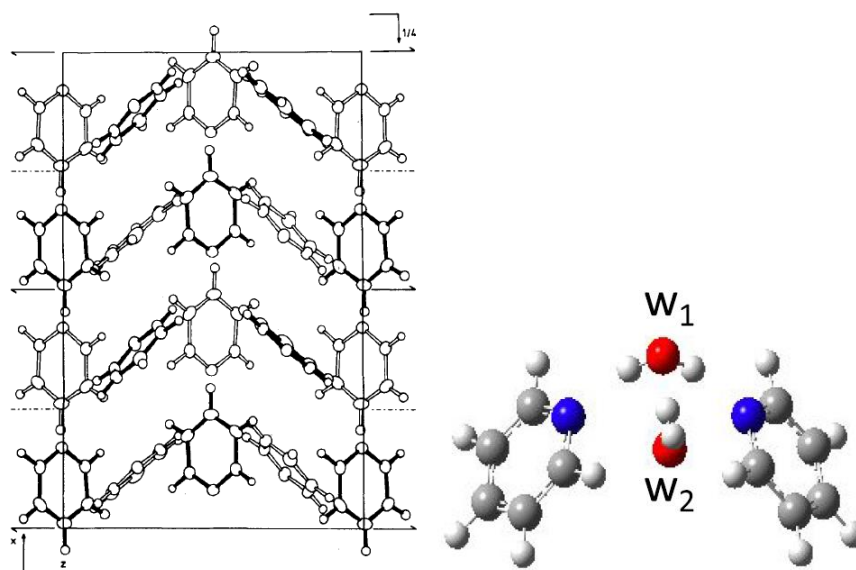


Figure 3.5. a) Crystal structure of pyridine, extracted from (Mootz & Wussow, 1981).  
 b) Structure of a stable pyridine-water cluster  $(\text{Pyridine})_2(\text{H}_2\text{O})_2$ , extracted from (Feng, et al., 2021).

Table 3.1. Peak positions of amorphous and crystalline pyridine with assignments and A-values. Peaks indicated in bold values were used in the analysis.

Wavenumber (amorphous) <sup>a</sup> , cm <sup>-1</sup>	Amorphous <sup>a</sup>		Wavenumber (crystalline) <sup>a</sup> , cm <sup>-1</sup>	Crystalline <sup>a</sup>		Assignment <sup>b</sup>
	Integration range	A-value, 10 <sup>-18</sup> cm/molecule		Integration range	A-value, 10 <sup>-18</sup> cm/molecule	
3026	3110-2970	5.05	3030	3100-2970	2.772	C-H stretch
1582	1610-1558	5.46	1580	1585-1573	3.07	C-C ring stretch
<b>1483</b>	1500-1460	1.30	1480	1490-1446	1.86	
<b>1438</b>	1460-1400	7.47	1435	1446-1360	10.1	
1146	1173-1124	0.776	1142	1150-1125	0.552	C-H deformation
<b>1068</b>	1086-1040	1.11	1065	1072-1040	1.35	
<b>1031</b>	1040-1025	1.19	1031	1040-1007	1.75	trigonal ring breathing
991	1007-982	1.27	991	997-981	1.76	ring breathing
750	780-740	3.08	750, 754	765-726	4.02	ring twist
705	740-690	8.84	712, 705	726-657	11.5	C-H out-of- plane deformation

a - (Hudson & Yarnall, 2022), b - (McMurtry, et al., 2016)

Table 3.2. Peak positions of amorphous water with assignments and A-values (Gerakines, et al., 1995). The wavenumber indicated in bold was used in the analysis.

Wavenumber, cm <sup>-1</sup>	Assignment	A-value, 10 <sup>-17</sup> cm/molecule
<b>3280</b>	O-H stretch	20.0
1660	O-H bend	1.2
760	libration	3.1

### 3.2 Pure pyridine irradiations – effect of initial ice structure

The amorphous and crystalline pure pyridine was irradiated with different projectiles at ARIBE and IRRSUD beamlines using IGLIAS and at SME beamline using CASIMIR. Amorphous samples were irradiated at 10 K and crystalline samples were irradiated at 10 and 130 K. The summary of the experimental parameters is presented in Table 3.3. The column densities were calculated with eq. (2.6) using the band strengths presented in Table 3.1. The values, indicated in Table 3.3 are the average values, calculated for four pyridine bands: 1030, 1068, 1438 and 1483 cm<sup>-1</sup>. These peaks were selected to facilitate comparison of the results, as they have been used in other studies (Muniz, 2017) and (Bibang, 2021). Additionally, they are convenient for the analysis in the case of pyridine-water mixtures because they do not overlap with the water peaks. The thicknesses were calculated using eq. (2.7). Stopping powers and penetration depths were calculated with the SRIM code (Ziegler, et al., 2010).

Table 3.3. Pure pyridine irradiations.

Ion	Setup/ beamline	T <sub>dep</sub> , K	T <sub>irr</sub> , K	S <sub>e</sub> , keV/μm	S <sub>n</sub> , keV/μm	Penetration depth, μm	Column density (10 <sup>17</sup> cm <sup>-2</sup> )	Initial thickness, μm
396 MeV <sup>36</sup> Ar <sup>17+</sup>	CASIMIR/ SME	15	15	978.7	0.54	284.7	33.8	5.69
		130	15	1440	0.78	193.5	35.5	4.07
626,4 MeV <sup>58</sup> Ni <sup>26+</sup>		15	15	1950	1.14	246.1	48.5	8.18
		130	15	2869	1.68	167.3	26.9	3.08
		130	130	2869	1.68	167.3	32.5	3.72
61,3 MeV <sup>84</sup> Kr <sup>15+</sup>		IGLIAS/ IRRSUD	10	10	4538	18.3	24.4	7.7
	130		10	6677	26.9	16.4	19.8	2.26
	130		130	6677	26.9	16.4	33.6	3.84

In all experiments, penetration depth is significantly greater than the sample thickness. Hence, deceleration primarily occurs due to the electronic stopping power. We can also assume that the energy of the ion remains nearly constant throughout the entire path within the material.

#### 3.2.1 Results on amorphous samples irradiation

Amorphous pyridine samples were deposited and irradiated at the same temperature 10 K (Figure 3.6). The radiolysis of pyridine was examined through modifications in the infrared spectrum. The destruction of pyridine was assessed by monitoring the evolution of four

pyridine bands: 1030, 1068, 1438 and 1483  $\text{cm}^{-1}$ , which were also used for the column density calculations.

The evolution of column density of amorphous pyridine as a function of ion fluence is fitted using the following formula (Mejía, et al., 2015):

$$N(F) = N_0 e^{-\sigma_d F} - (N_0 - N_p) e^{-(\sigma_c + \sigma_d) F}. \quad \text{eq. (3.1)}$$

The first term of eq. (3.1) is a solution of  $\frac{dN}{dF} = -\sigma_d F$ , where  $\sigma_d$  is destruction cross section, as was mentioned at the Chapter 2. The second term of eq. (3.1) is stands for the compaction. Compaction is characterized by an increase in the peak area at the beginning of the irradiation.  $\sigma_c$  is a compaction cross section;  $N_p$  is the column density of the porous ice (before irradiation) and  $N_0$  is the column density of compacted ice (when peak area is maximum). Without compaction occurring,  $N_0 = N_p$ . Figure 3.7 presents best fits of the column density evolution of amorphous pyridine irradiated with 396 MeV  $^{36}\text{Ar}^{17+}$  by using eq. (3.1). The vertical error bars represent the uncertainty in the A-value arising from the changes of the sample density during the irradiation, and are estimated to be around 20%. The horizontal error bars are estimated to be around 10%, attributed to the uncertainties in the flux calculation.



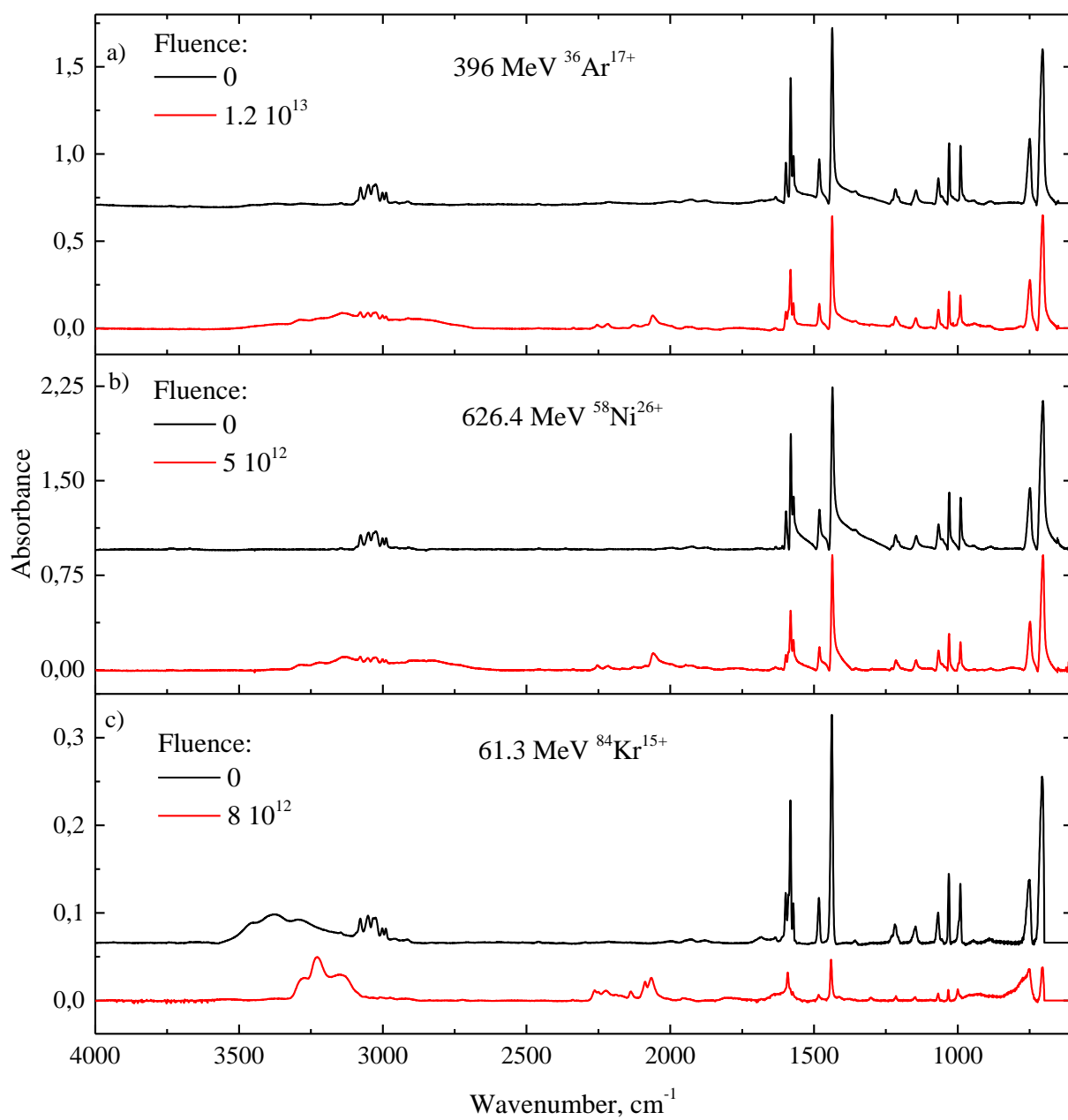


Figure 3.6. Infrared spectra of unirradiated amorphous pure pyridine (black line) and irradiated (red line) at low temperature with final fluence a)  $1.2 \cdot 10^{13}$  ions/cm<sup>2</sup> with 396 MeV  $^{36}\text{Ar}^{17+}$ , b)  $5 \cdot 10^{12}$  ions/cm<sup>2</sup> with 626.4 MeV  $^{58}\text{Ni}^{26+}$ , c)  $8 \cdot 10^{12}$  ions/cm<sup>2</sup> with  $^{84}\text{Kr}^{15+}$ .

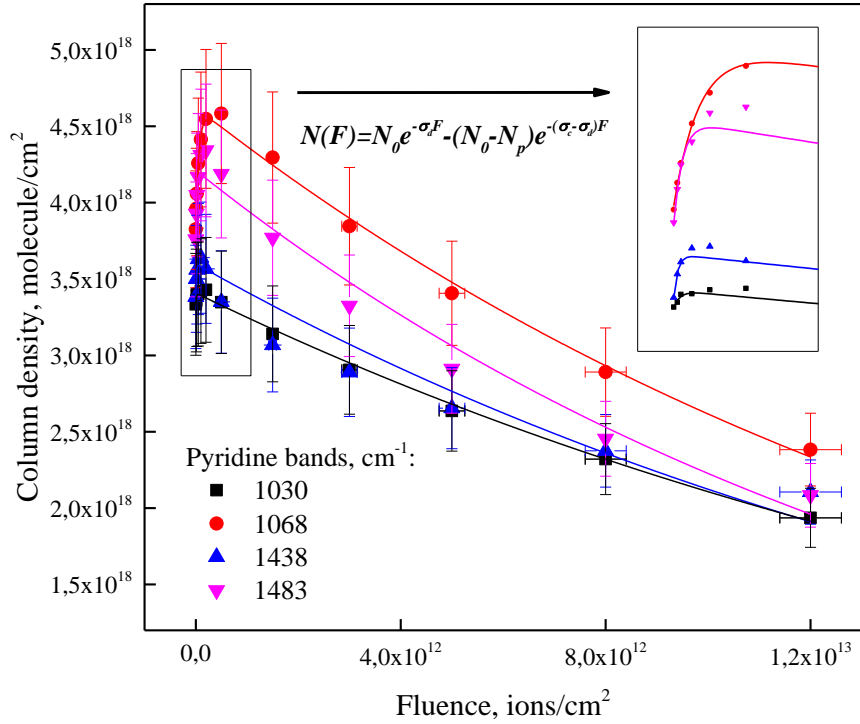


Figure 3.7. Fitting of column density evolution as a function of the projectile fluence for pyridine irradiated with 396 MeV  $^{36}\text{Ar}^{17+}$ .

Table 3.4 presents results on destruction cross section of amorphous pyridine, irradiated with different ions for four bands. It includes the average value across four bands, along with the standard deviation, calculated as  $SD = \sqrt{\frac{\sum |\sigma_d^i - \text{average}|^2}{4}}$ , which represent around 15% of the value. Additionally, the table includes results from previous studies (Bibang, 2021) and (Muniz, 2017).

Table 3.4. Destruction cross section of amorphous pyridine, irradiated with different ions.

Ion	Destruction cross section, $\text{cm}^2$				Average $\pm$ SD
	1030 $\text{cm}^{-1}$	1068 $\text{cm}^{-1}$	1438 $\text{cm}^{-1}$	1483 $\text{cm}^{-1}$	
396 MeV $^{36}\text{Ar}^{17+}$	$4.89 \cdot 10^{-14}$	$5.85 \cdot 10^{-14}$	$5.28 \cdot 10^{-14}$	$6.80 \cdot 10^{-14}$	$5.71 \pm 0.83 \cdot 10^{-14}$
626,4 MeV $^{58}\text{Ni}^{26+}$	$1.44 \cdot 10^{-13}$	$1.21 \cdot 10^{-13}$	$1.00 \cdot 10^{-13}$	$1.63 \cdot 10^{-13}$	$1.32 \pm 0.27 \cdot 10^{-13}$
61,3 MeV $^{84}\text{Kr}^{15+}$	$2.56 \cdot 10^{-13}$	$2.23 \cdot 10^{-13}$	$2.47 \cdot 10^{-13}$	$2.96 \cdot 10^{-13}$	$2.56 \pm 0.30 \cdot 10^{-13}$
90 keV $^{16}\text{O}^{6+}$					$5.52 \cdot 10^{-15a}$
650 MeV $^{65}\text{Zn}^{26+}$					$1.14 \cdot 10^{-13a}$
116 MeV $^{238}\text{U}^{32+}$					$6.50 \cdot 10^{-13b}$

a - (Bibang, 2021) , b – (Muniz, 2017)

Table 3.5 presents the results on the compaction dose and compaction cross section of pyridine, calculated for different bands, along with the average values. The compaction dose was determined as an average dose across four peaks, as the maximum peak area for different peaks corresponds to different doses. It should be noted that the error bars for the compaction

dose are quite large, as the measurements were taken discretely with a step size of around 0.3 eV/molecule. It can also be observed from Table 3.5 that the compaction cross section for different projectiles does not change significantly.

In the previous works (Dartois, et al., 2013) and (Mejía, et al., 2015) authors investigated compaction of porous water ice induced by ion irradiation by tracing the evolution of OH-dangling bonds, which are present for the porous water ice. They concluded that compaction rate is directly proportional to the stopping power of the projectile. The compaction of water occurs at deposited dose around 0.17-0.24 eV/molecule. Considering that the average value for the compaction of pyridine over three projectiles from Table 3.5 is 0.46, it can be concluded that in space the compaction of pyridine takes two times longer than compaction of water. This difference in dose can be attributed to the different sizes of the molecules. Since pyridine molecule is significantly larger than water molecule, more energy is required to reorganize the structure of the sample.

*Table 3.5. Compaction dose and cross section of amorphous pyridine irradiated with different ions.*

Ion	Stopping power, keV/ $\mu\text{m}$	Compaction dose, eV/molecule	Compaction cross section, $10^{-11} \text{ cm}^2$				Average $\pm$ SD
			1030 $\text{cm}^{-1}$	1068 $\text{cm}^{-1}$	1438 $\text{cm}^{-1}$	1483 $\text{cm}^{-1}$	
396 MeV $^{36}\text{Ar}^{17+}$	979.2	0.33	6.03	1.45	8.92	4.14	$5.13 \pm 3.15$
626,4 MeV $^{58}\text{Ni}^{26+}$	1951.1	0.42	1.87	1.58	10.97	4.93	$4.84 \pm 4.36$
61,3 MeV $^{84}\text{Kr}^{15+}$	4556.3	0.59	-	4.96	6.53	7.18	$6.22 \pm 1.14$

The main objective of our experiments is to predict the molecule's survivability in space. Since it is impossible to conduct experiments with all the ions present in space, it is necessary to identify the pattern of pyridine degradation based on the properties of the projectiles. The main characteristic that influences the level of destruction is the energy of the particle, related particularly to the electronic stopping power. The destruction cross section of molecular ice as a function of electronic stopping power of the projectile obeys a power law (De Barros, et al., 2012), (Andrade, et al., 2013), (Costa, et al., 2020):

$$\sigma_d = CS_e^n. \quad \text{eq. (3.2)}$$

For amorphous pyridine the values C and n are equal to  $5.79 \cdot 10^{-17} \left[ \frac{10^{-10}}{\text{keV}} \right]$  and  $0.98 \pm 0.13$ , respectively (Figure 3.8). The power coefficient value obtained in this study differs from that reported by (Bibang, et al., 2021). This difference is attributed to the increased number of projectiles used in our experiments, which resulted in a more constrained value. The obtained value is in good agreement with the literature (Rothard, et al., 2017). Power coefficient close to 1.0 (linear dependence) have been observed for  $\text{CO}_2$  (Mejía, et al., 2015) and more complex species such as thymine (Mejía, et al., 2023) and valine (Costa, et al., 2020).

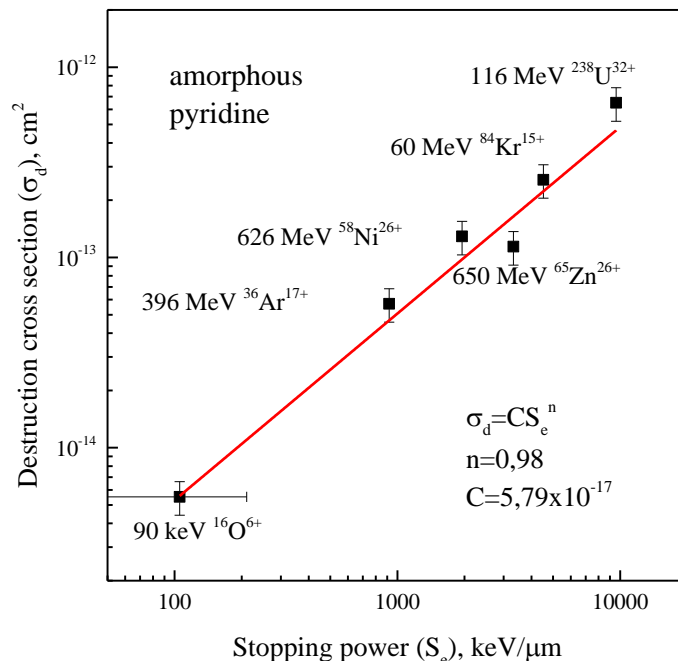


Figure 3.8. Destruction cross section as a function of electronic stopping power for pure pyridine irradiated with different ion beams: 90 keV  $O^{6+}$ , 396 MeV  $Ar^{17+}$ , 626.4 MeV  $Ni^{26+}$ , 650 MeV  $Zn^{26+}$ , 60 MeV  $Kr^{15+}$ , 116 MeV  $U^{32+}$ .

Figure 3.9 illustrates the normalized area  $A/A_0$  as a function of deposited dose for amorphous pyridine for two bands, 1438 and 1030  $cm^{-1}$ . The local dose, calculated using the eq. (2.8), is considered as a key parameter (Costa, et al., 2020), (Muniz, 2017), the evolution of the sample under ion bombardment depends on the deposited energy. In Figure 3.9, it is observed that the degradation of pyridine as a function of deposited dose follows a consistent trend across different projectiles, despite only heavy ions being employed in pyridine experiments. In the next chapter about pyrene, we will address this issue in detail; in particular we will see that local dose is not a key parameter for less ionizing projectiles (H and He). To gain a better understanding of pyridine radiolysis under ion irradiation, it will be necessary to conduct experiments with lighter ions in the future.

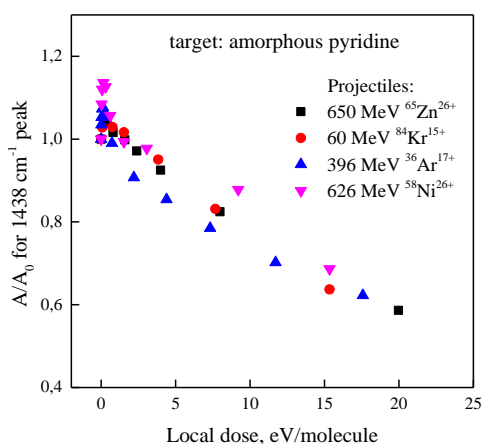


Figure 3.9. 1438  $cm^{-1}$  peak area normalized to the initial area as a function of deposited dose for amorphous pyridine irradiated with different projectiles.

### 3.2.2 Results on crystalline samples irradiation

Crystalline samples of pure pyridine were deposited at 130 K and irradiated at different temperatures, 10 K and 130 K, as outlined in Table 3.3. Infrared spectra of crystalline pyridine before and after irradiation are presented in Figure 3.10. The irradiation process induces three primary processes in the crystalline pyridine samples: the destruction of the molecules forming the crystalline structure, the transition from crystalline to an amorphous phase (amorphization) and the destruction of the molecules forming the amorphous structure. This can be described by the following equations:

$$\frac{dN^{cr}}{dF} = -\sigma_d^{cr}N^{cr} - \sigma_a N^{cr}, \quad \text{eq. (3.2)}$$

$$\frac{dN^{am}}{dF} = -\sigma_d^{am}N^{am} + \sigma_a N^{cr}, \quad \text{eq. (3.3)}$$

where  $N^{cr}$  is the number of molecules forming the crystalline structure per  $\text{cm}^2$ ,  $N^{am}$  is the number of molecules forming the amorphous structure per  $\text{cm}^2$ , so the total column density  $N = N^{am} + N^{cr}$ .  $\sigma_d^{cr}$  is the destruction cross section of the molecules forming the crystalline structure,  $\sigma_d^{am}$  is the destruction cross section of the molecules forming the amorphous structure and  $\sigma_a$  is the amorphization cross section. There is no compaction observed for crystalline samples.

As previously discussed, the crystalline structure distinguishes itself from the amorphous one in the infrared spectrum by exhibiting multiple sharp peaks rather than a single broad peak. In Figure 3.11 the evolution of the pyridine bands under irradiation with various projectiles is depicted. It is evident from the Figure 3.11 that the initially crystalline structure transforms into an amorphous state for all of the projectiles used.

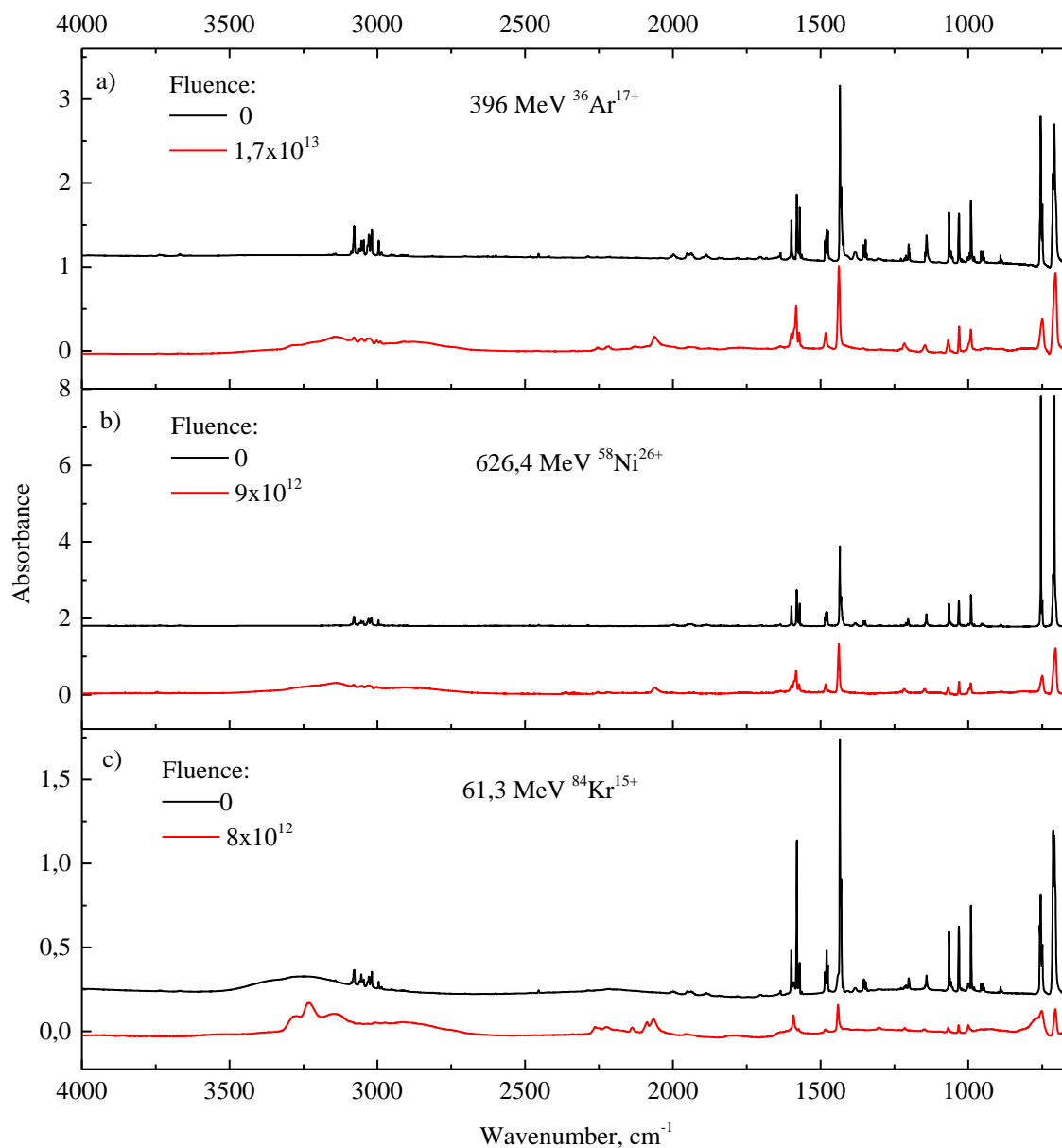


Figure 3.10. Infrared spectra of pure crystalline pyridine (black line) and irradiated (red line) to final fluence a)  $1.7 \cdot 10^{13}$  ions/cm<sup>2</sup> with 396 MeV  $^{36}\text{Ar}^{17+}$  at 15K, b)  $9 \cdot 10^{12}$  ions/cm<sup>2</sup> with 626.4 MeV  $^{58}\text{Ni}^{26+}$  at 130 K, c)  $8 \cdot 10^{12}$  ions/cm<sup>2</sup> with  $^{84}\text{Kr}^{15+}$  at 10K.

During irradiation, the crystalline structure of pyridine undergoes degradation through two processes: amorphization and destruction. Using only IR spectrometry, it is impossible to differentiate between these two processes. Additionally, it is challenging to accurately determine the ratio of the remaining crystalline to the appearing amorphous fraction. Fortunately, in the case of pyridine, there is one band, which is present only for the crystalline material –  $1354 \text{ cm}^{-1}$  (range  $1360\text{-}1340 \text{ cm}^{-1}$ ) with A-value  $0.388 \cdot 10^{-18} \text{ cm/molecule}$  (Hudson & Yarnall, 2022). Following the evolution of this band we can determine  $\sigma_a + \sigma_d^{cr}$  (Figure 3.12).

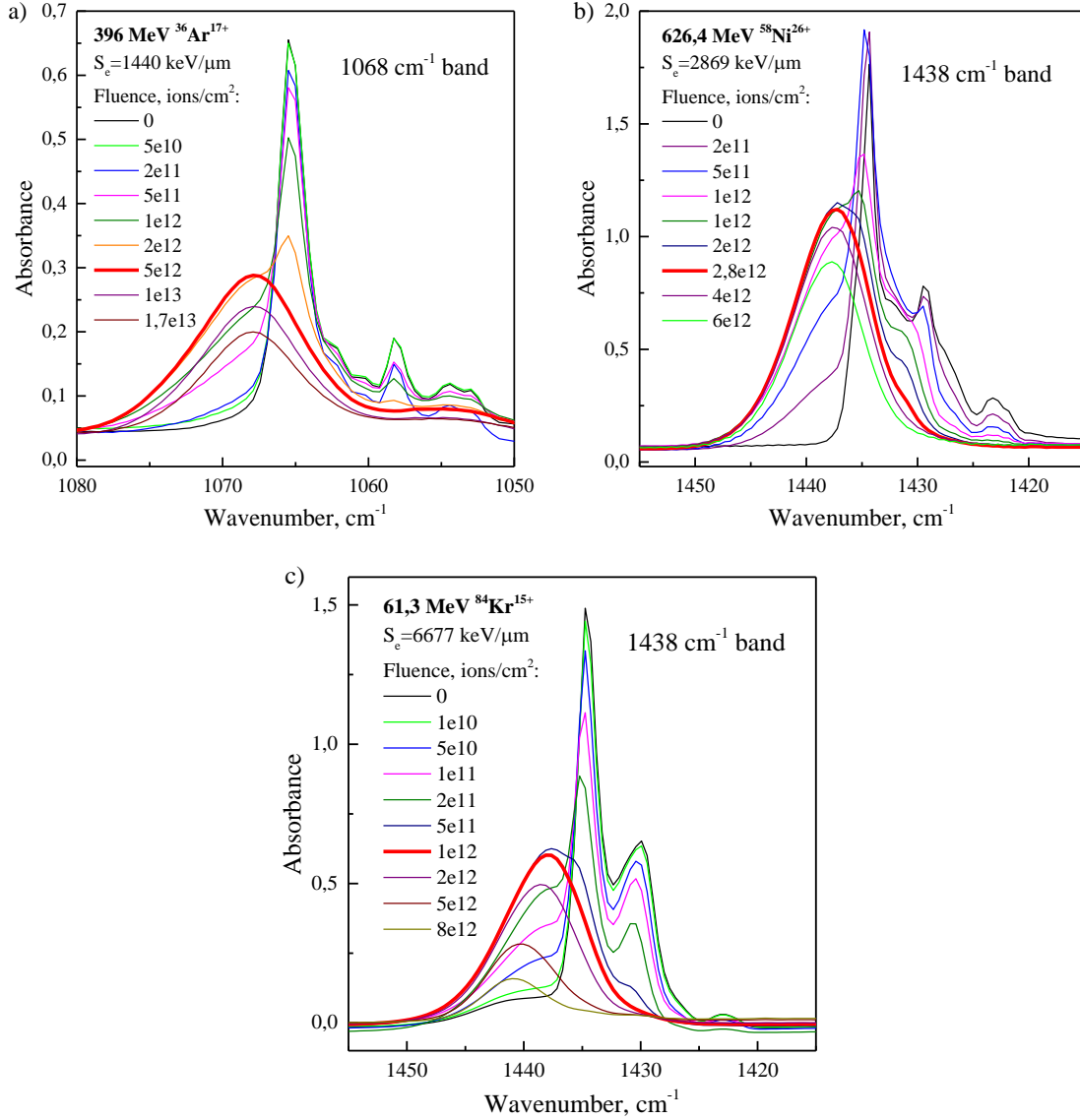


Figure 3.11. 1068 and 1438  $\text{cm}^{-1}$  pyridine band evolution under irradiation with a) 396 MeV  $^{36}\text{Ar}^{17+}$ , b) 626.4 MeV  $^{58}\text{Ni}^{26+}$ , c) 61.3 MeV  $^{84}\text{Kr}^{15+}$  at low temperature. The red line is the first spectrum of fully amorphous sample.

Additionally, it is possible to estimate the cross section  $\sigma_d^{cr}$ . As discussed earlier the destruction cross section increase with electronic stopping power obeys a power law, with the power coefficient for pyridine equal to 0.98:  $\sigma_d \sim S_e^{0.98}$ . In our experiments, ions are in the Bethe-Bloch regime (Section 1.3.1), when electronic stopping power is directly proportional to the target density  $S_e \sim \rho$ . The density ratio of crystalline pyridine to amorphous  $\frac{\rho_{crystal}}{\rho_{amorphous}}$  is 1.47. Thus, the destruction cross section of crystalline pyridine should be around 1.46 times higher than destruction cross section of amorphous pyridine:  $\left(\frac{\sigma_d^{crystal}}{\sigma_d^{amorphous}}\right) = \left(\frac{\rho_{crystal}}{\rho_{amorphous}}\right)^{0.98} = 1.47^{0.98} = 1.46$ . For example, the destruction cross section for a 396 MeV  $^{36}\text{Ar}^{17+}$  in amorphous pyridine is  $4.76 \cdot 10^{-14} \text{ cm}^2$ , and in crystalline pyridine, it is  $6.94 \cdot 10^{-14} \text{ cm}^2$  (Table 3.6).

Table 3.6 presents results on pure pyridine irradiations. The destruction cross sections of the amorphous phase  $\sigma_d^{am}$  for crystalline samples were calculated when full amorphization of samples was reached. The column  $\sigma_d^{am}$  of Table 3.6 indicates the average value obtained for four bands (1030, 1068, 1438, 1483  $\text{cm}^{-1}$ ) for both crystalline and amorphous samples. It should be noted that the values for  $\sigma_d^{am}$  are close to each other for different initial structures. Therefore, it can be concluded that after amorphization, the crystalline samples behave similarly to the samples, initially already being amorphous. Amorphization cross sections  $\sigma_a$  were calculated as a difference between  $\sigma_d^{cr} + \sigma_a$ , obtained from 1354  $\text{cm}^{-1}$  band and  $\sigma_d^{cr}$ , which is equal to  $1.46 \cdot \sigma_d^{am}$ .

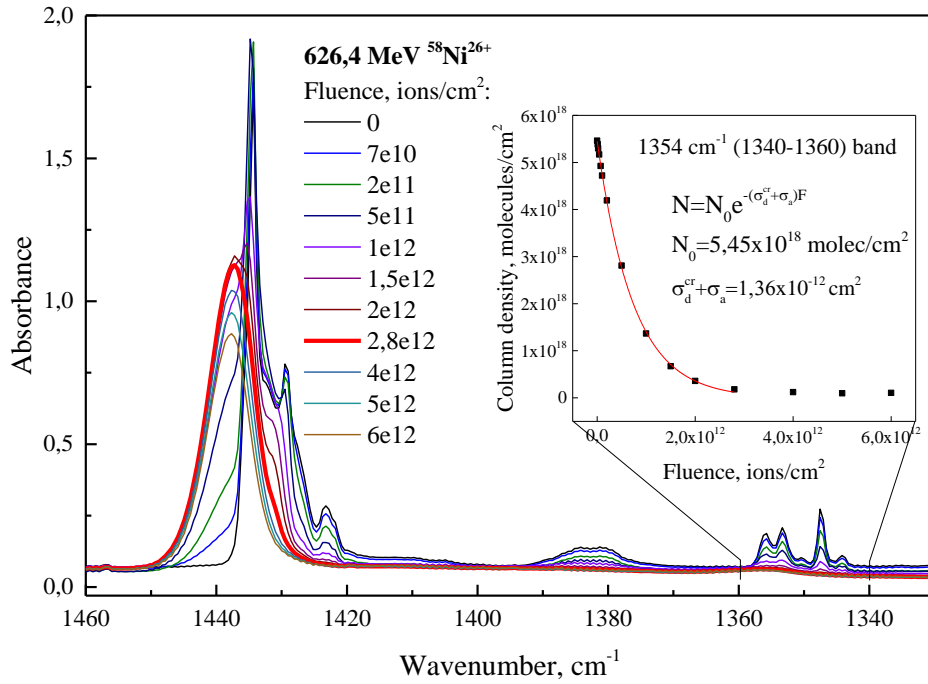


Figure 3.12. Evolution of the infrared spectra of crystalline pyridine during irradiation with 626.4 MeV  $^{58}\text{Ni}^{26+}$  in the range 1335-1460  $\text{cm}^{-1}$  and the fitting of the column density evolution of 1354  $\text{cm}^{-1}$  crystalline band.

Table 3.6. Destruction and amorphization cross sections, amorphization fluences and doses obtained during experiments with pure pyridine irradiation.

Ion	Initial structure of pyridine	$T_{\text{irr}}$	Amorphization fluence, ions/ $\text{cm}^2$	Amorphization dose, eV/molecule	$\sigma_d^{am}$ , $\text{cm}^2$ average over 4 bands	$\sigma_d^{cr} = 1,46 \cdot \sigma_d^{am}$ , $\text{cm}^2$	$\sigma_d^{cr} + \sigma_a$ , $\text{cm}^2$ obtained from 1354 $\text{cm}^{-1}$ band	$\sigma_a$ , $\text{cm}^2$
396 MeV $^{36}\text{Ar}^{17+}$	cr	15K	$5 \cdot 10^{12}$	7.7	$4.76 \pm 0.21 \cdot 10^{-14}$	$6.95 \cdot 10^{-14}$	$8.65 \cdot 10^{-13}$	$7.96 \cdot 10^{-13}$
	am	15K			$5.71 \pm 0.83 \cdot 10^{-14}$			
626,4 MeV $^{58}\text{Ni}^{26+}$	cr	15K	$2.8 \cdot 10^{12}$	9.2	$9.57 \pm 1.69 \cdot 10^{-14}$	$1.39 \cdot 10^{-13}$	$1.36 \cdot 10^{-12}$	-
	cr	130K	$5.5 \cdot 10^{12}$	18.1	$7.06 \pm 2.23 \cdot 10^{-14}$	$1.03 \cdot 10^{-13}$	$0.53 \cdot 10^{-12}$	$0.43 \cdot 10^{-12}$
	am	15K			$13.2 \pm 2.71 \cdot 10^{-14}$			
61,3 MeV $^{84}\text{Kr}^{15+}$	cr	10K	$1.0 \cdot 10^{12}$	7.6	$2.08 \pm 0.13 \cdot 10^{-13}$	$3.04 \cdot 10^{-13}$	$5.91 \cdot 10^{-12}$	$5.61 \cdot 10^{-12}$
	cr	130K	$1.4 \cdot 10^{12}$	10.7	$2.52 \pm 0.25 \cdot 10^{-13}$	$3.68 \cdot 10^{-13}$	$2.38 \cdot 10^{-12}$	$2.01 \cdot 10^{-12}$
	am	15K			$2.56 \pm 0.30 \cdot 10^{-13}$			



By comparing the data from columns “amorphization dose” and “ $\sigma_a$ ,” in Table 3.6, it can be concluded that amorphization occurs more rapidly at lower temperatures 10-15 K, than at high temperature 130 K. A similar result was obtained in previous studies dedicated to ion-induced amorphization of water ice (Dartois, et al., 2015), (Famá, et al., 2010). They reported an increase in the amorphization dose with an increase in irradiation temperature. (Famá, et al., 2010) attributed this effect to the alternation in the specific heat of the ice with temperature.

(Dartois, et al., 2015) reported that the amorphization dose for water ice irradiated with four different heavy ions – 3640 MeV Ni<sup>26+</sup>, 19.6 MeV Ne<sup>6+</sup>, 46 MeV Ni<sup>11+</sup> and 81 MeV Ta<sup>24+</sup> – at temperatures 13-15 K, is approximately 0.82 eV/molecule. For pyridine ice, the amorphization dose at 10-15 K across three projectiles, indicated in Table 3.6, is 8.2 eV/molecules, which is ten times higher than for water. This can be explained by the fact that the pyridine molecule is larger in size, and thus it requires more energy to dislodge all the atoms from the crystal lattice.

We conducted experiments on the irradiation of amorphous pyridine in addition to the previous works (Bibang, et al., 2021), (Muniz, 2017), and refined the value of the power coefficient for the destruction cross section dependence on the electronic stopping power of the ion. The obtained coefficient will be used in Chapter 6 to calculate the half-life time of pyridine in dense clouds. Additionally, we obtained values for the compaction cross section of pyridine and found that pyridine compaction requires twice the dose compared to water compaction. We also showed that the destruction cross section for crystalline pyridine is higher than for amorphous pyridine, due to the higher density of the crystalline structure. Furthermore, we assessed the amorphization dose for crystalline pyridine and showed that at high temperatures, the amorphization requires more energy.

### 3.3 Pyridine-water mixtures irradiation

Pyridine-water mixtures were prepared and irradiated at different temperatures with three different ions: 626.4 MeV <sup>58</sup>Ni<sup>26+</sup>, 60 MeV <sup>84</sup>Kr<sup>15+</sup> and 90 keV <sup>16</sup>O<sup>6+</sup>. Table 3.7 summarizes experimental parameters. The column density of water was calculated for the 3280 cm<sup>-1</sup> band. The percentage of pyridine in the mixture is the ratio of column densities  $N_{\text{pyridine}}/(N_{\text{water}}+N_{\text{pyridine}})$ . Our goal was to investigate whether the destruction rate of pyridine changes in the presence of a water matrix and if it depends on pyridine concentration in the mixture.

As discussed above, when the concentration of pyridine in the mixture with water is low (less than 25%), the crystalline structure of pyridine is not observed. Therefore, the crystalline structure of pyridine was observed only in one case in the present experiment. It was mixture with 25% of pyridine, irradiated with 61.3 MeV <sup>84</sup>Kr<sup>15+</sup> at 150 K (highlighted with \* in Table 3.7).

Table. 3.7. Experimental parameters of pyridine-water irradiations.

Energy/Ion	Percentage of pyridine, %	T <sub>dep</sub> , K	T <sub>irr</sub> , K	Stopping power, keV/μm		Penetration depth, μm	Column density, 10 <sup>17</sup> cm <sup>-2</sup>		Initial thickness of the sample, μm
				Electronic	Nuclear		Pyridine	Water	
626,4 MeV <sup>58</sup> Ni <sup>26+</sup> (March 2023) CASIMIR/ SME	1.5			2528	1.51	195.36	0.28	19.4	0.67
	20	15	15	2360	1.39	206.38	10.3	40.9	3.04
	100			1950	1.14	246.07	48.5	-	8.18
	8	150	15	2434	1.45	201.63	3.29	39.2	1.82
	100	130		2869	1.68	167.3	26.9	-	3.08
	9	150	150	2424	1.44	202.25	2.48	25.3	1.23
61,3 MeV <sup>84</sup> Kr <sup>15+</sup> (May 2022) IGLIAS/ IRRSUD	100	130	130	2869	1.68	167.3	32.5	-	3.72
	9			5523	23.7	20.6	6.0	60.7	2.97
	12	10	10	5479	23.4	20.6	8.0	54.1	2.94
	55			4971	20.7	22.1	37.5	30.8	7.29
	100			4524	18.7	24.1	7.7	-	1.30
	5	150	10	5532	23.9	20.7	2.8	40.3	1.77
	20			5322	22.6	21.1	17.8	66.6	5.15
	100	130		6677	26.9	16.4	19.8	-	2.26
	5			5532	23.9	20.7	2.9	41.1	1.82
	15	150	150	5385	22.9	20.9	7.7	48.8	2.87
25*			5804	24.5	19.2	10.7	30.6	2.21	
100	130	130	6677	26.9	16.4	33.6	-	3.84	
90 keV <sup>16</sup> O <sup>6+</sup> (October 2021) IGLIAS/ ARIBE	1			130.0	58.1	0.43	0.4	41.8	1.40
	3	8	8	135.1	57.6	0.42	1.5	44.7	1.68
	25			158.8	54.4	0.40	8.9	28.4	2.31
	1	150	8	128.6	57.5	0.43	0.3	38.3	1.29
	3			133.7	57.0	0.43	1.3	34.7	1.34
	1	150	150	128.6	57.5	0.43	0.5	41.1	1.41
	20			157.4	53.9	0.41	7.4	28.9	2.21
	1	100	100	130.0	58.1	0.43	0.6	50.8	1.73
20			158.8	54.4	0.40	9.5	35.6	2.64	

Figure 3.13 presents examples of pyridine-water mixtures before and after irradiation with various projectiles, deposited and irradiated at different temperatures.

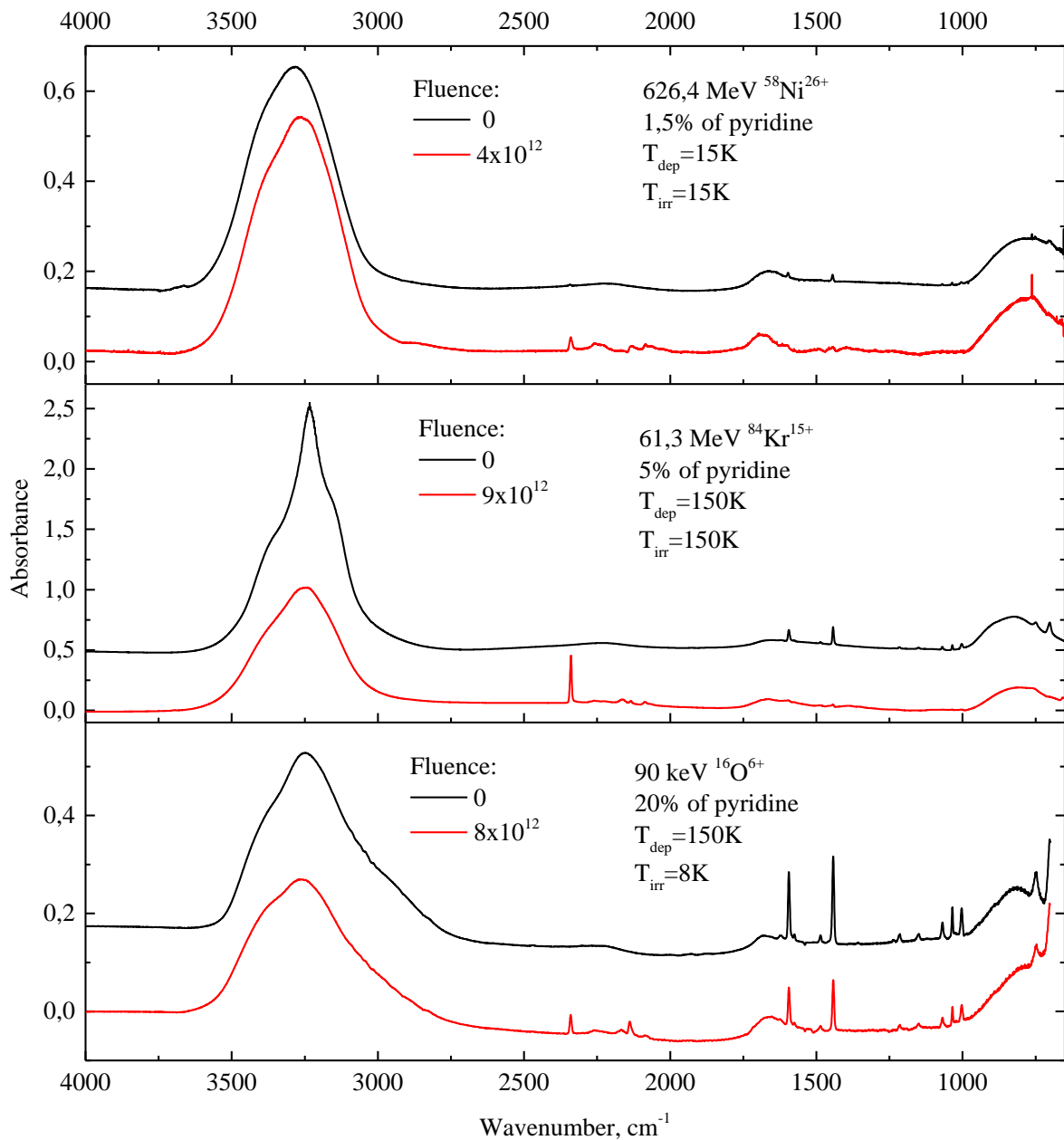


Figure 3.13. Infrared spectra of pyridine-water mixtures before (black line) irradiation and at final fluence (red line). a) 1,5% of pyridine deposited at 15K and irradiated at 15K with 626.4 MeV  $^{58}\text{Ni}^{26+}$ ; b) 5% of pyridine deposited at 150K and irradiated at 150K with 61.3 MeV  $^{84}\text{Kr}^{15+}$ ; c) 20% of pyridine deposited at 150K and irradiated at 8K with 90 keV  $^{16}\text{O}^{6+}$ .

A best fit of eq. (3.1) of the column density evolution as a function of ion fluence was performed as shown in Figure 3.14. Note that the second term, which stands for the compaction was removed as there is no significant compaction observed for pyridine in mixtures with water. In the case of the O projectile, the ions were implanted inside the sample, as the projected range is smaller than sample thickness. Since part of the sample remained unirradiated, the final equation includes an additional term  $N_2$  – number of unirradiated molecules:

$$N(F) = N_0 e^{-\sigma_d F} + N_2. \quad \text{eq. (3.4)}$$

The examples of the  $1438 \text{ cm}^{-1}$  band best fits are presented in Figure 3.14.

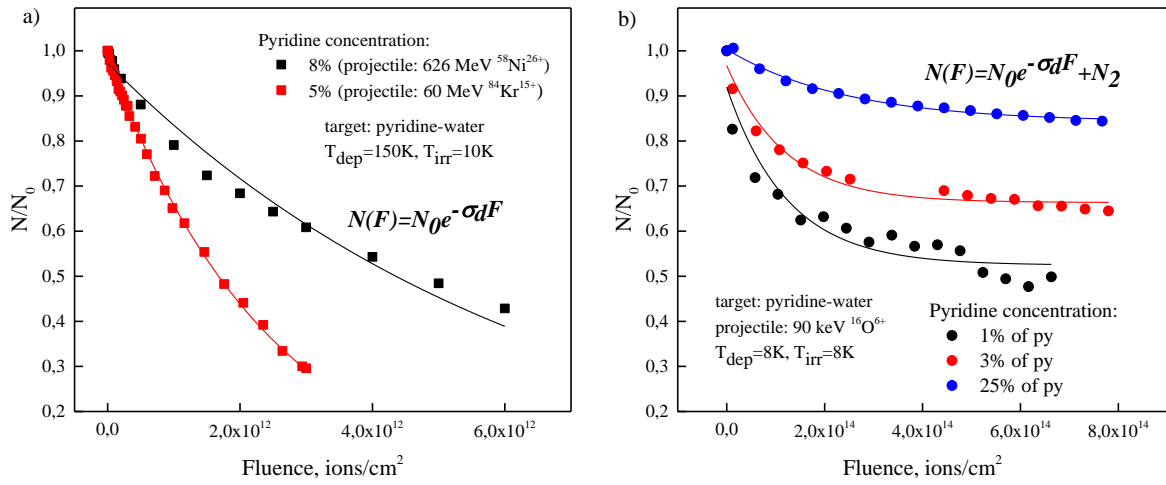


Figure 3.14. Examples of normalized  $1438 \text{ cm}^{-1}$  peak area fitting in pyridine-water mixtures as a function of ion fluence a) for Ni (8% of pyridine) and Kr (5% of pyridine) ion beams and b) for O (1-25% of pyridine) ion beam.

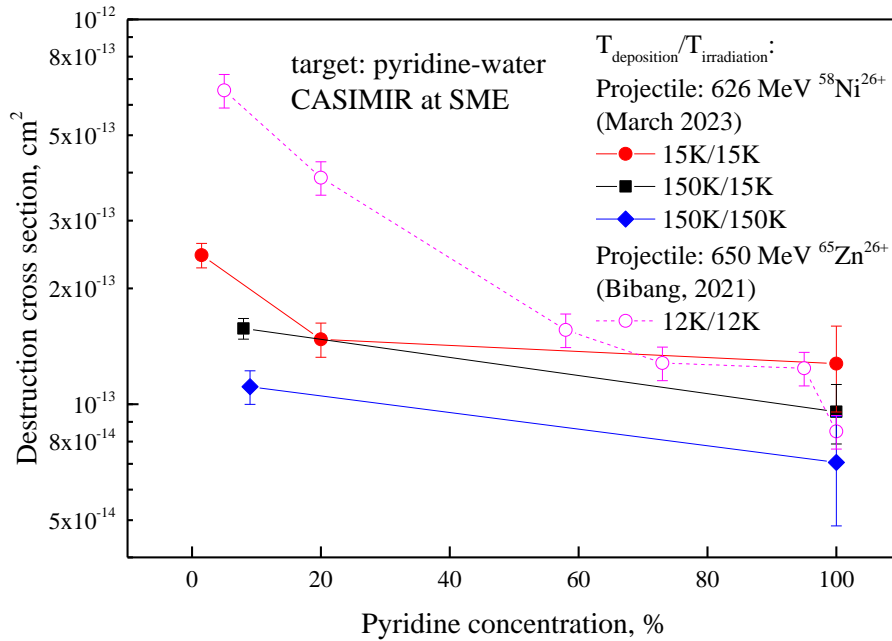


Figure 3.15. Destruction cross section of amorphous pyridine in pyridine-water mixtures, irradiated with 626 MeV  $^{58}\text{Ni}^{26+}$  and 650 MeV  $^{65}\text{Zn}^{26+}$ .

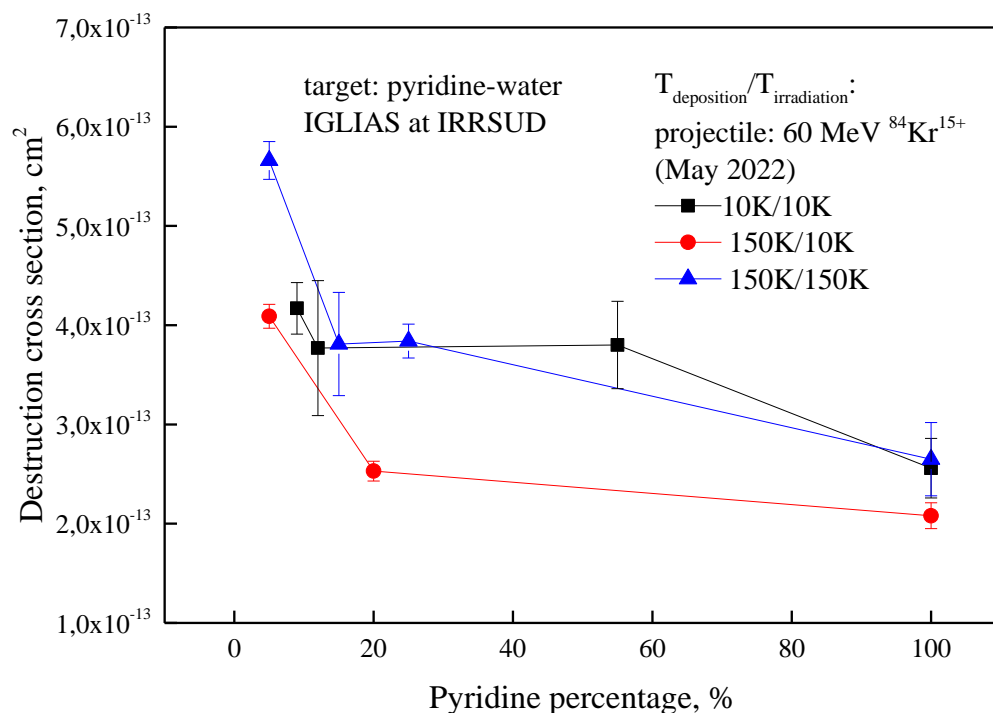


Figure 3.16. Destruction cross section of amorphous pyridine in pyridine-water mixtures, irradiated with 60 MeV  $^{84}\text{Kr}^{15+}$ .

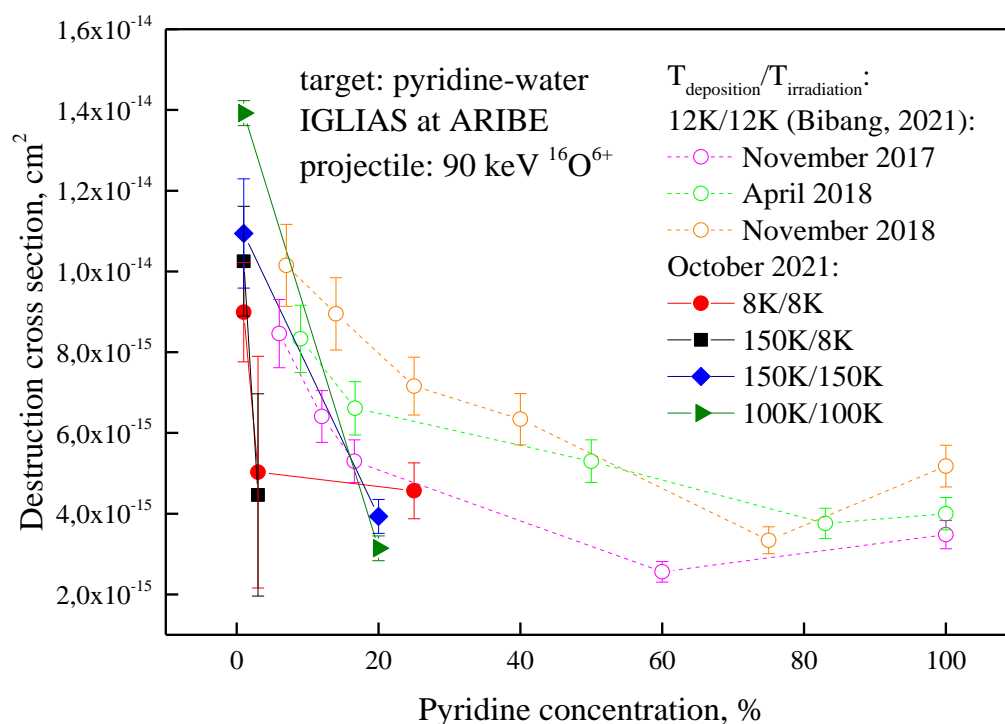


Figure 3.17. Destruction cross section of amorphous pyridine in pyridine-water mixtures, irradiated with 90 keV  $^{16}\text{O}^{6+}$ .

The results on destruction cross sections of pyridine as a function of pyridine concentration in the mixtures are presented in Figures 3.15-3.17 and Table 3.8 for different ion beams. The error bars in the figures represent standard deviation. In the case of crystalline

samples, the value  $\sigma_d^{\text{am}}$  is indicated, which means the destruction cross section of amorphous pyridine after amorphization was complete. Figures 3.15 and 3.17 also present data from previous work (Bibang, 2021) on pyridine-water irradiations.

*Table 3.8. Destruction cross section of amorphous pyridine during pyridine-water mixtures irradiation.*

Energy/Ion	Percentage of pyridine, %	T <sub>dep</sub> , K	T <sub>irr</sub> , K	Destruction cross section, cm <sup>2</sup>					
				1030 cm <sup>-1</sup>	1068 cm <sup>-1</sup>	1438 cm <sup>-1</sup>	1483 cm <sup>-1</sup>	Mean ± SD	
626,4 MeV <sup>58</sup> Ni <sup>26+</sup> (March 2023)	1.5	15	15	2.31·10 <sup>-13</sup>		2.56·10 <sup>-13</sup>		2.44 ± 0.18·10 <sup>-13</sup>	
	20			1.49·10 <sup>-13</sup>	1.61·10 <sup>-13</sup>	1.32·10 <sup>-13</sup>	1.47 ± 0.15·10 <sup>-13</sup>		
	100	150	15	1.44·10 <sup>-13</sup>	1.19·10 <sup>-13</sup>	0.86·10 <sup>-13</sup>	1.60·10 <sup>-13</sup>	1.27 ± 0.32·10 <sup>-13</sup>	
	8			1.51·10 <sup>-13</sup>	1.68·10 <sup>-13</sup>	1.53·10 <sup>-13</sup>		1.57 ± 0.09·10 <sup>-13</sup>	
	100			130	0.89·10 <sup>-13</sup>	0.77·10 <sup>-13</sup>	1.00·10 <sup>-13</sup>	1.16·10 <sup>-13</sup>	0.96 ± 0.17·10 <sup>-13</sup>
		9	150	150	1.07·10 <sup>-13</sup>	1.24·10 <sup>-13</sup>	1.02·10 <sup>-13</sup>		1.11 ± 0.11·10 <sup>-13</sup>
		100	130	130	0.79·10 <sup>-13</sup>	0.98·10 <sup>-13</sup>	0.55·10 <sup>-13</sup>	0.49·10 <sup>-13</sup>	0.71 ± 0.22·10 <sup>-13</sup>
	9	10	10	4.29·10 <sup>-13</sup>	3.88·10 <sup>-13</sup>	4.35·10 <sup>-13</sup>		4.17 ± 0.26·10 <sup>-13</sup>	
	12			3.88·10 <sup>-13</sup>	4.39·10 <sup>-13</sup>	3.05·10 <sup>-13</sup>		3.77 ± 0.68·10 <sup>-13</sup>	
	55			3.60·10 <sup>-13</sup>	3.43·10 <sup>-13</sup>	3.75·10 <sup>-13</sup>	4.43·10 <sup>-13</sup>	3.80 ± 0.44·10 <sup>-13</sup>	
	100			2.56·10 <sup>-13</sup>	2.23·10 <sup>-13</sup>	2.47·10 <sup>-13</sup>	2.96·10 <sup>-13</sup>	2.56 ± 0.30·10 <sup>-13</sup>	
61,3 MeV <sup>84</sup> Kr <sup>15+</sup> (May 2022)	5	150	10	4.23·10 <sup>-13</sup>	4.01·10 <sup>-13</sup>	4.05·10 <sup>-13</sup>		4.09 ± 0.12·10 <sup>-13</sup>	
	20			2.59·10 <sup>-13</sup>	2.41·10 <sup>-13</sup>	2.59·10 <sup>-13</sup>		2.53 ± 0.10·10 <sup>-13</sup>	
	100	130		2.08·10 <sup>-13</sup>	2.07·10 <sup>-13</sup>	1.91·10 <sup>-13</sup>	2.24·10 <sup>-13</sup>	2.08 ± 0.13·10 <sup>-13</sup>	
		5	150	150	5.52·10 <sup>-13</sup>		5.79·10 <sup>-13</sup>		5.66 ± 0.19·10 <sup>-13</sup>
		15			4.17·10 <sup>-13</sup>	4.05·10 <sup>-13</sup>	3.22·10 <sup>-13</sup>		3.81 ± 0.52·10 <sup>-13</sup>
		25*			3.98·10 <sup>-13</sup>	3.64·10 <sup>-13</sup>	3.99·10 <sup>-13</sup>	3.74·10 <sup>-13</sup>	3.84 ± 0.17·10 <sup>-13</sup>
		100	130	130	3.01·10 <sup>-13</sup>	2.41·10 <sup>-13</sup>	2.26·10 <sup>-13</sup>	2.93·10 <sup>-13</sup>	2.65 ± 0.37·10 <sup>-13</sup>
90 keV <sup>16</sup> O <sup>6+</sup> (October 2021)	1	8	8	9.86·10 <sup>-15</sup>		8.13·10 <sup>-15</sup>		8.99 ± 1.23·10 <sup>-15</sup>	
	3			3.00·10 <sup>-15</sup>		7.06·10 <sup>-15</sup>	5.03 ± 2.87·10 <sup>-15</sup>		
	25			5.35·10 <sup>-15</sup>		4.30·10 <sup>-15</sup>	4.05·10 <sup>-15</sup>	4.57 ± 0.69·10 <sup>-15</sup>	
	1	150	8	11.22·10 <sup>-15</sup>		9.29·10 <sup>-15</sup>		10.25 ± 1.36·10 <sup>-15</sup>	
	3			4.45·10 <sup>-15</sup>		6.98·10 <sup>-15</sup>	1.97·10 <sup>-15</sup>	4.46 ± 2.51·10 <sup>-15</sup>	
	1	150	150	11.89·10 <sup>-15</sup>		9.98·10 <sup>-15</sup>		10.94 ± 1.35·10 <sup>-15</sup>	
	20			3.74·10 <sup>-15</sup>		3.64·10 <sup>-15</sup>	4.41·10 <sup>-15</sup>	3.93 ± 0.42·10 <sup>-15</sup>	
	1	100	100	14.14·10 <sup>-15</sup>		13.70·10 <sup>-15</sup>		13.92 ± 0.31·10 <sup>-15</sup>	
	20			3.34·10 <sup>-15</sup>		2.79·10 <sup>-15</sup>	3.30·10 <sup>-15</sup>	3.14 ± 0.31·10 <sup>-15</sup>	

In all cases, an increase in destruction cross section at low concentrations of pyridine in the water is observed. This result confirms the findings of the previous study at low temperature of 15 K (Bibang, 2021), conducted within the same research group on pyridine-water radiolysis. The discussion concerning this phenomenon will be provided in the next chapter. As for the influence of irradiation temperature on pyridine destruction, no significant effect has been observed.

Table 3.9 presents a comparison of amorphization and destruction parameters of crystalline samples of pure pyridine and pyridine-water mixture (25% of pyridine). As mentioned earlier, the value  $\sigma_d^{\text{am}}$  is higher for pyridine, trapped in the water matrix (3.84·10<sup>-13</sup> cm<sup>2</sup>), than for the pure pyridine (2.52·10<sup>-13</sup> cm<sup>2</sup>).  $\sigma_d^{\text{cr}} + \sigma_{\text{am}}$  is 2 times higher for pure pyridine (2.38·10<sup>-12</sup> cm<sup>2</sup>) than for the mixture (1.12·10<sup>-12</sup> cm<sup>2</sup>), which leads to the conclusion that

amorphization occurs four times faster for pure pyridine compared to the mixture. It should also be noted that the 20 K difference in irradiation temperature could have affected the values of the amorphization dose. For a more accurate comparison, additional experiments at the same irradiation temperature are needed.

*Table 3.9. Destruction and amorphization cross sections, amorphization fluences and doses obtained during irradiation of crystalline pure pyridine and crystalline pyridine-water mixture (25% of pyridine) with 61.3 MeV  $^{84}\text{Kr}^{15+}$ .*

	$T_{\text{irr}}$	Amorphization fluence, ions/cm <sup>2</sup>	Amorphization dose, eV/molecule	$\sigma_d^{\text{am}}$ , cm <sup>2</sup> average over 4 bands	$\sigma_d^{\text{cr}} = 1,46 \cdot \sigma_d^{\text{am}}$ , cm <sup>2</sup>	$\sigma_d^{\text{cr}} + \sigma_{\text{am}}$ , cm <sup>2</sup> <sup>1</sup> obtained from 1354 cm <sup>-1</sup> band	$\sigma_{\text{am}}$ , cm <sup>2</sup>
Pure pyridine	130K	$1.4 \cdot 10^{12}$	10.7	$2.52 \pm 0.25 \cdot 10^{-13}$	$3.68 \cdot 10^{-13}$	$2.38 \cdot 10^{-12}$	$2.01 \cdot 10^{-12}$
25% of pyridine	150K	$7 \cdot 10^{11}$	2.2	$3.84 \pm 0.15 \cdot 10^{-13}$	$5.61 \cdot 10^{-13}$	$1.12 \cdot 10^{-12}$	$0.56 \cdot 10^{-12}$

### 3.4 New molecules formation

The new molecules formed during irradiation of pure pyridine with different projectiles are similar regardless the deposition and irradiation temperature of the sample. In the case of pyridine-water mixtures, the same molecules that formed during the irradiation of pure pyridine are present, along with the addition of some oxygen-containing compounds. In addition, in the case of mixtures, the variety of newly formed molecules remains constant irrespective to the deposition or irradiation temperature. Figure 3.18 presents new bands arising from the irradiations. In the wavenumber range from 2340 to 2050 cm<sup>-1</sup>, many new compounds emerge, predominantly containing nitrogen in their composition. Additionally, there is a noticeable emergence of new molecules in the range of 3135-3286 cm<sup>-1</sup>.

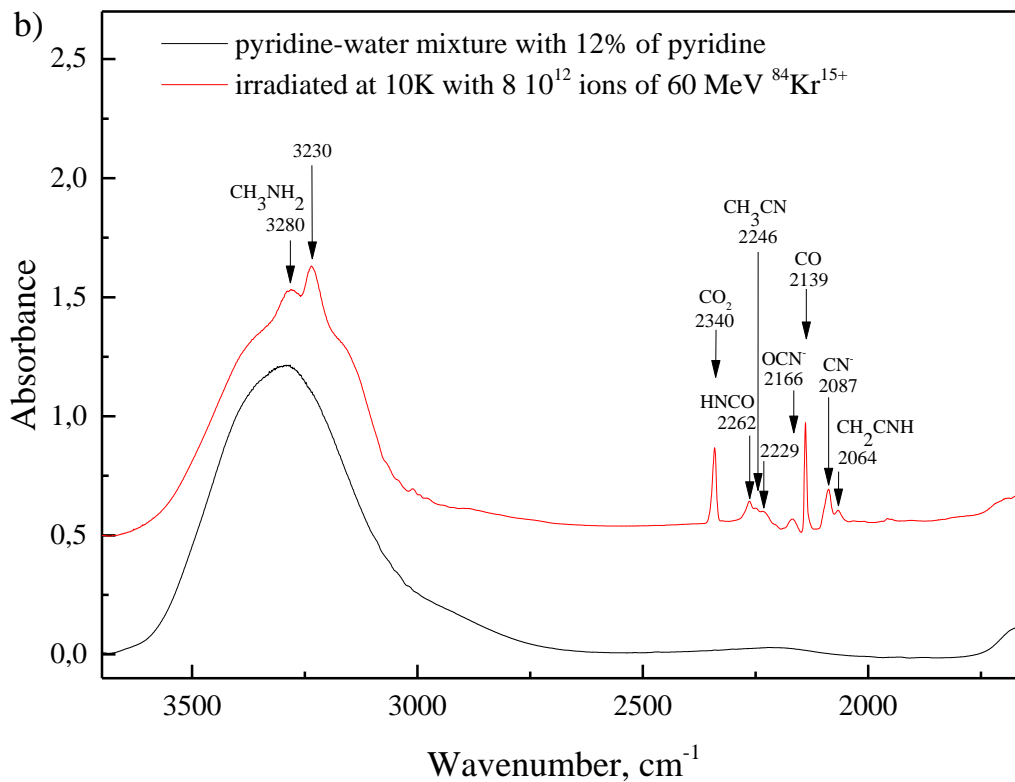
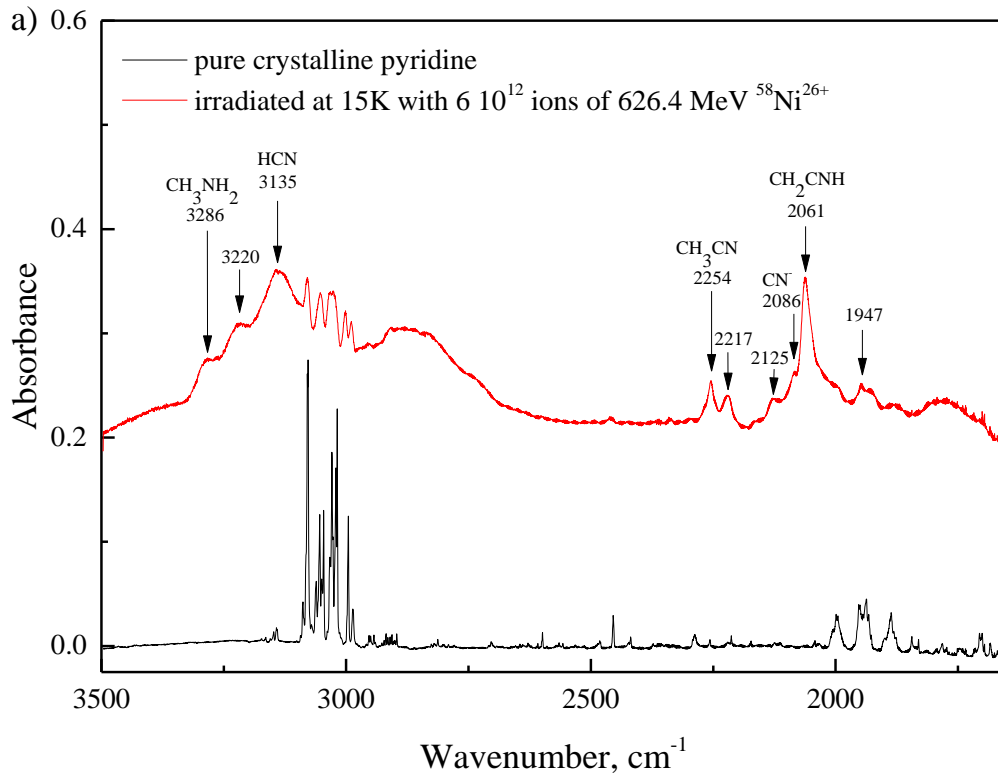


Figure 3.18. New bands arising after irradiation of a) pure crystalline pyridine with  $6 \cdot 10^{12}$  ions/cm<sup>2</sup> of 626.4 MeV  $^{58}\text{Ni}^{26+}$ ; b) amorphous pyridine-water mixture (12% of pyridine) with  $8 \cdot 10^{12}$  ions/cm<sup>2</sup> of 60 MeV  $^{84}\text{Kr}^{15+}$ .



Table 3.10. Wavenumbers, assignments and band strengths of new species arising from irradiations.

Wavenumber, cm <sup>-1</sup>		Assignment	A-value, cm/molecule	Reference
pure C <sub>5</sub> H <sub>5</sub> N	C <sub>5</sub> H <sub>5</sub> N+H <sub>2</sub> O			
	756	unidentified		
999		CH <sub>3</sub> NH <sub>2</sub>		(Van Broekhuizen , et al., 2004)
1230	1235	unidentified		
1300	1300	CH <sub>4</sub>	1.04·10 <sup>-17</sup>	(Gerakines & Hudson, 2015)
1413		CH <sub>3</sub> CH=NH		(Danger, et al., 2011)
	1641	CH <sub>2</sub> NH		(Van Broekhuizen , et al., 2004)
	1668	CH <sub>3</sub> CH <sub>2</sub> NH <sub>3</sub> <sup>+</sup>		(Danger, et al., 2011)
	1691	HCONH <sub>2</sub>	3.3·10 <sup>-17</sup>	(Van Broekhuizen , et al., 2004)
1947	1951	H <sub>2</sub> CNH		(Gerakines, et al., 2004)
1994		unidentified		
	2031	unidentified		
2061	2066	CH <sub>2</sub> =C=NH		(Danger, et al., 2011)
2086	2084	CN <sup>-</sup>		(Gerakines, et al., 2004)
2127	2127	CH <sub>3</sub> - <sup>15</sup> N(?)		(Danger, et al., 2011)
	2133	CO	1.1·10 <sup>-17</sup>	(Gerakines, et al., 1995)
2164	2166	OCN <sup>-</sup>	1.3·10 <sup>-16</sup>	(Van Broekhuizen , et al., 2004)
2188		unidentified		
2219	2230	CH <sub>3</sub> C≡ <sup>15</sup> N(?)		(Danger, et al., 2011)
2254		CH <sub>3</sub> C≡N		(Danger, et al., 2011)
2254	2260	HNCO	7.2·10 <sup>-17</sup>	(Van Broekhuizen , et al., 2004)
2296		unidentified		
2339 (contaminant)	2339	CO <sub>2</sub>	7.6·10 <sup>-17</sup>	(Gerakines, et al., 1995)
2363		unidentified		
2830		unidentified		
2912		unidentified		
2973		unidentified		
3135		HCN	7.4·10 <sup>-17</sup>	(Gerakines, et al., 2022)
3220	3225	unidentified		
3286	3280	CH <sub>3</sub> NH <sub>2</sub>		(Theulé, et al., 2011)

Nevertheless, infrared spectroscopy is not the best technique for new molecule identification in the case of complex organic species. Since new peaks appearing during irradiation have weak intensities, they also overlap with larger peaks of the parent molecules, and peak positions can also shift depending on the surrounding matrix. However, some new compounds were identified with high certainty. Table 3.10 presents the major peaks and their assignments. A question mark placed near some assignments indicates uncertainty, as these assignments involve molecules containing the nitrogen isotope <sup>15</sup>N, whose presence makes their formation unlikely.

Assessing the column density of new compounds is challenging due to the overlapping of bands. Therefore, here we will provide only the evolution of CO<sub>2</sub> molecule for mixtures,

irradiated with 60 MeV  $^{84}\text{Kr}^{16+}$  (Figure 3.19) and the evolution of CO and CO<sub>2</sub> molecules for mixtures irradiated with 90 keV  $^{16}\text{O}^{6+}$  (Figure 3.20). In other cases, the CO and/or CO<sub>2</sub> bands overlap with bands of other new formed compounds.

However, in the case of CO and CO<sub>2</sub>, it should be noted that the evaporation temperature is low. Therefore, the data presented in Figures 3.19-20 in some cases only considers molecules trapped within the matrix. As the pressure in the vacuum chamber is around  $10^{-9}$  mbar, thus, the sublimation temperatures of CO and CO<sub>2</sub> molecules are approximately 25 and 70K, respectively. The sublimation temperature for CO<sub>2</sub> was directly taken from the work (Fray & Schmitt, 2009), while the one for the CO molecule was calculated, based on the polynomial coefficients presented in the same work. Therefore, at high temperatures (100-150K), in the infrared spectrum we observe only those molecules, which are trapped in the matrix.

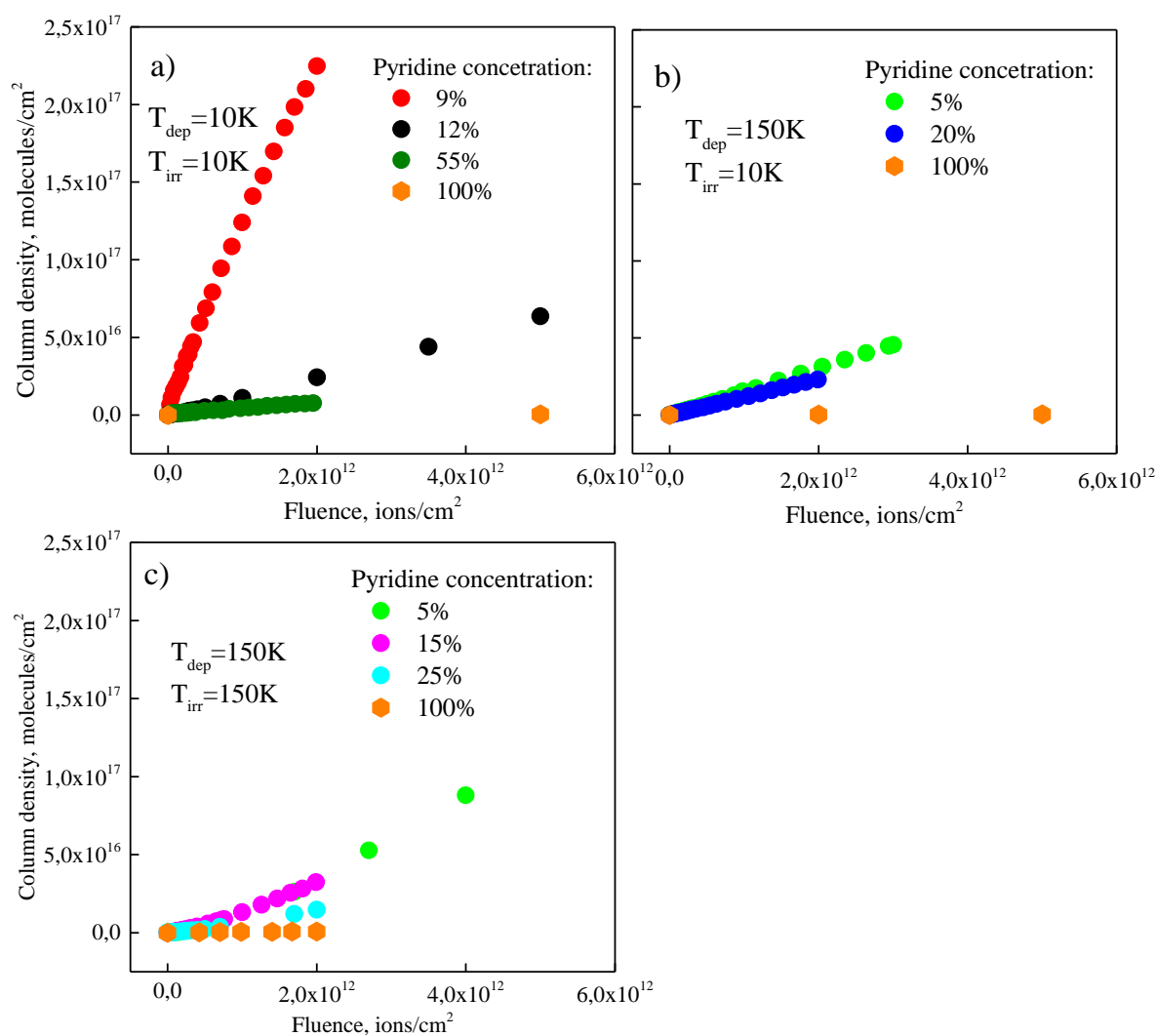


Figure 3.19. CO<sub>2</sub> evolution during pyridine-water mixtures irradiation with 60 MeV  $^{84}\text{Kr}^{16+}$ . Mixtures were deposited and irradiated at a) 10K, 10K; b) 150K, 10K; c) 150K, 150K respectively.

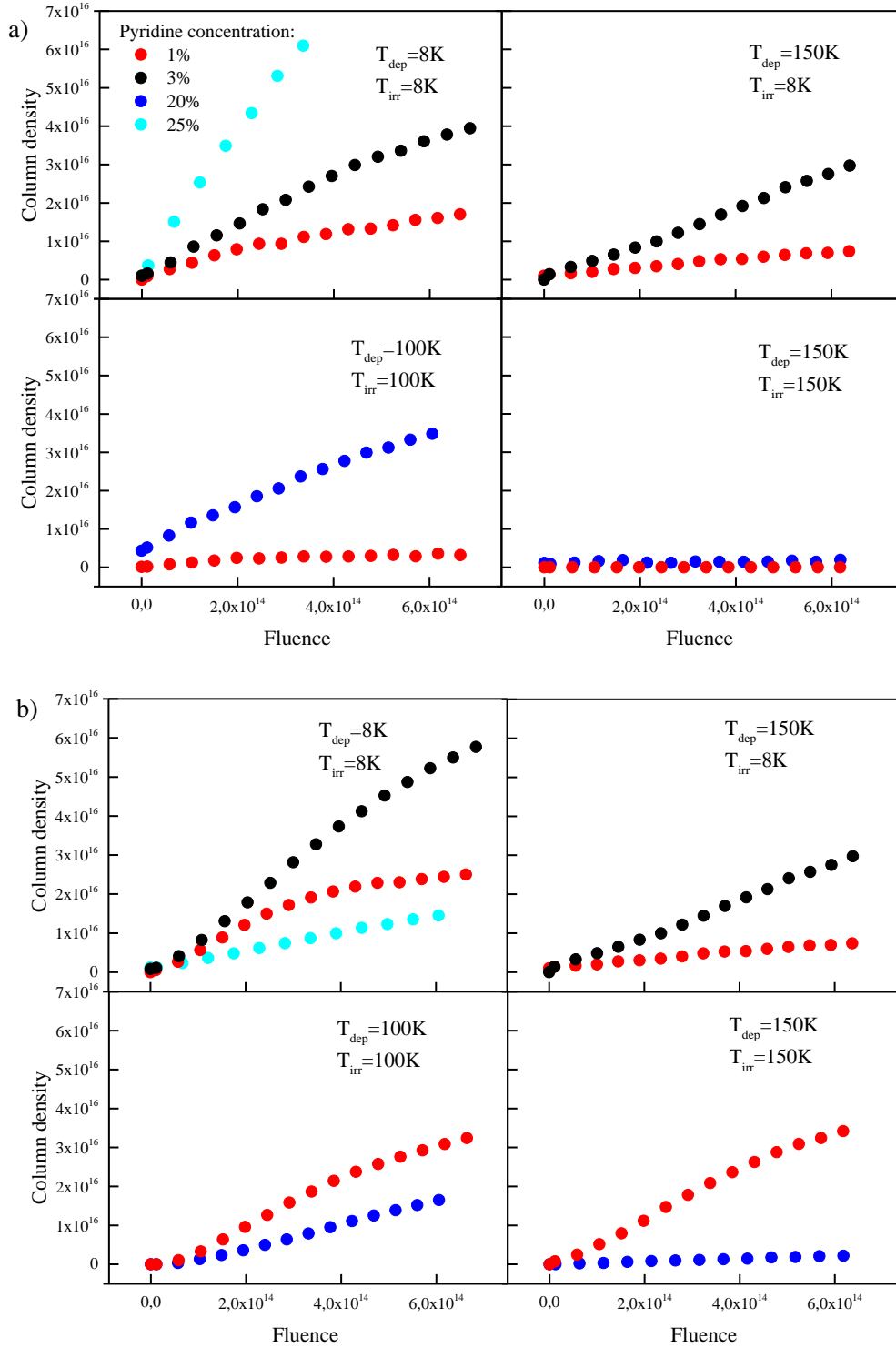


Figure 3.20.  $CO$  (a) and  $CO_2$  (b) molecule evolution during irradiation of pyridine-water mixtures with  $90\text{ keV }^{16}O^{6+}$  at different pyridine concentration and temperatures of deposition/irradiation. Different colours correspond to different pyridine concentrations: 1% (red), 3% (black), 20% (blue), 25% (cyan).

The evolution of new species is well described by the equation (De Barros, et al., 2016):

$$\frac{N_j(F)}{N_{<i>i,0}} = (\sigma_{fj}F) \left[ 1 - \frac{1}{2} \sigma_d^{eff} F \right], \quad \text{eq. (3.5)}$$

where  $N_j$  is column density of daughter molecule  $j$ ,  $N_{<i,0}$  is initial column density of the minority parent molecule,  $\sigma_{fj}$  is formation cross section of daughter molecule  $j$ , respectively and  $\sigma_d^{eff} = \sigma_{d,i} + \sigma_{d,j}$  is effective destruction cross section. Since at the beginning of irradiation destruction of daughter molecules is negligible, the formation cross sections, presented in the Table 3.11 and 3.12 were obtained from the slope for four and five first points (Figure 3.18, 3.19), respectively.

*Table 3.11. Formation cross section of CO<sub>2</sub> molecule during irradiation of pyridine-water mixtures with 60 MeV <sup>84</sup>Kr<sup>16+</sup>.*

Pyridine concentration, %	T <sub>dep</sub>	T <sub>irr</sub>	$\sigma_f$ of CO <sub>2</sub> , 10 <sup>-14</sup> cm <sup>2</sup>
9			22,82
12	10	10	1,38
55			0,068
5	150	10	4,03
20			0,62
5			7,58
15	150	150	2,06
25*			0,67

*Table 3.12. Formation cross section of CO and CO<sub>2</sub> during pyridine-water mixtures irradiation with 90 keV <sup>16</sup>O<sup>6+</sup>.*

Pyridine concentration, %	T <sub>dep</sub>	T <sub>irr</sub>	Formation cross section, 10 <sup>-17</sup> cm <sup>2</sup>	
			CO	CO <sub>2</sub>
1			122,09	153,06
3	8	8	51,37	56,25
25			25,42	2,48
1	150	8	110,96	35,34
3			47,29	32,43
1	150	150	-	110,53
20			0,41	0,53
1	100	100	19,69	93,01
20			7,24	2,37

Tables 3.11 and 3.12 show that the formation cross sections for CO and CO<sub>2</sub> molecules decreases as the concentration of pyridine in the mixture increases for both Kr and O projectiles. This can be explained by the decreasing amount of available oxygen atoms as the water concentration decreases. This trend is observed for all three temperature conditions investigated.

A variety of new molecules emerges during the pyridine and pyridine:H<sub>2</sub>O ice irradiation. However, as mentioned earlier, IR spectroscopy is not a very effective technique for identifying new species, and only molecules present in sufficient quantities can be detected using this method and some of them are listed in Table 3.10. As the concentration of CO and CO<sub>2</sub> is notably higher than all other new molecules, it was possible to determine the formation cross section of these two molecules (Table 3.11, 3.12). However, for future work in order to more accurately identify new molecules, including complex biologically relevant molecules,

techniques such as high resolution mass spectroscopy, electrospray and others should be employed.

## References

- Altaf, A. A. et al., 2015. A review on the medicinal importance of pyridine derivatives. *J. Drug Des. Med. Chem.*, pp. 1-11.
- Andrade, D. P. et al., 2013. Chemical reactions induced in frozen formic acid by heavy ion cosmic rays. *Monthly Notices of the Royal Astronomical Society*, 430(2), pp. 787-796.
- Bibang, P. A., 2021. *Molécules organiques complexes sous irradiation: effets de la matrice et de la température*. Caen: Normandie Université.
- Bibang, P. A. et al., 2021. Radiolysis of pyridine in solid water. *The European Physical Journal D*, pp. 1-12.
- Bordalo, V. et al., 2013. Chemical processing of pure ammonia and ammonia–water ices induced by heavy ions. *The Astrophysical Journal*, 774(2), p. 105.
- Cable, M. L. et al., 2021. Titan in a test tube: Organic co-crystals and implications for Titan mineralogy. *Accounts of Chemical Research*, 54(15), pp. 3050-3059.
- Cernicharo, J. et al., 2001. Infrared space observatory's discovery of C<sub>4</sub>H<sub>2</sub>, C<sub>6</sub>H<sub>2</sub>, and benzene in CRL 618. *The Astrophysical Journal*, 546(2), p. L123.
- Costa, C. A. D. et al., 2020. Valine radiolysis by H<sup>+</sup>, He<sup>+</sup>, N<sup>+</sup>, and S<sup>15+</sup> MeV ions. *International journal of molecular sciences*, 21(5), p. 1893.
- Danger, G. et al., 2011. Experimental investigation of nitrile formation from VUV photochemistry of interstellar ices analogs: acetonitrile and amino acetonitrile. *Astronomy & Astrophysics*, Volume 525, p. A30.
- Dartois, E. et al., 2015. Heavy ion irradiation of crystalline water ice-Cosmic ray amorphisation cross-section and sputtering yield. *Astronomy & Astrophysics*, Volume 576, p. A125.
- Dartois, E. et al., 2013. Swift heavy ion irradiation of water ice from MeV to GeV energies- Approaching true cosmic ray compaction. *Astronomy & Astrophysics*, Volume 557, p. A97.
- De Barros, A. L. F. et al., 2012. Radiolysis of astrophysical ices by heavy ion irradiation: destruction cross section measurement. *Low Temperature Physics*, 38(8), pp. 759-765.
- De Barros, A. L. F. et al., 2012. Radiolysis of astrophysical ices by heavy ion irradiation: destruction cross section measurement. *Low Temperature Physics*, 38(8), pp. 759-765.
- De Barros, A. L. F. et al., 2016. Ion irradiation of ethane and water mixture ice at 15 k: Implications for the solar system and the ism. *The Astrophysical Journal*, 824(2), p. 81.
- Famá, M., Loeffler, M. J., Raut, U. & Baragiola, R. A., 2010. Radiation-induced amorphization of crystalline ice. *Icarus*, pp. 314-319.
- Feistel, R. & Wagner, W., 2006. A new equation of state for H<sub>2</sub>O ice Ih. *Journal of Physical and Chemical Reference Data*, pp. 1021-1047.
- Feng, J. Y. et al., 2021. Structures of pyridine–water clusters studied with infrared–vacuum ultraviolet spectroscopy. *The Journal of Physical Chemistry A*, 125(34), pp. 7489-7501.

- Fray, N. & Schmitt, B., 2009. Sublimation of ices of astrophysical interest: A bibliographic review. *Planetary and Space Science*, 57(14-15), pp. 2053-2080.
- Gerakines, P. A. & Hudson, R. L., 2015. Infrared spectra and optical constants of elusive amorphous methane. *The Astrophysical Journal Letters*, p. L20.
- Gerakines, P. A., Moore, M. H. & Hudson, R. L., 2004. Ultraviolet photolysis and proton irradiation of astrophysical ice analogs containing hydrogen cyanide. *Icarus*, 170(1), pp. 202-213.
- Gerakines, P. A., Schutte, W. A., Greenberg, J. M. & van Dishoeck, E. F., 1995. The infrared band strengths of H<sub>2</sub>O, CO and CO<sub>2</sub> in laboratory simulations of astrophysical ice mixtures. *Astronomy and Astrophysics*, p. 810.
- Gerakines, P. A., Yarnall, Y. Y. & Hudson, R. L., 2022. Direct measurements of infrared intensities of HCN and H<sub>2</sub>O+ HCN ices for laboratory and observational astrochemistry. *Monthly Notices of the Royal Astronomical Society*, 509(3), pp. 3515-3522.
- Ghormley, J. A. & Hochanadel, C. J., 1971. Amorphous ice: Density and reflectivity. *Science*, pp. 62-64.
- Godard, M. et al., 2011. Ion irradiation of carbonaceous interstellar analogues-Effects of cosmic rays on the 3.4  $\mu\text{m}$  interstellar absorption band. *Astronomy & Astrophysics*, Volume 529, p. A146.
- Gudipati, M. S. & Allamandola, L. J., 2004. Polycyclic aromatic hydrocarbon ionization energy lowering in water ices. *The Astrophysical Journal*, 615(2), p. L177.
- Hansen, G. B. & McCord, T. B., 2004. Amorphous and crystalline ice on the Galilean satellites: A balance between thermal and radiolytic processes. *Journal of Geophysical Research: Planets*, 109(E1).
- Herington, E. F. G. & Martin, J. F., 1953. Vapour pressures of pyridine and its homologues. *Transactions of the Faraday Society*, Volume 49, pp. 154-162.
- Hudson, R. L. & Yarnall, Y. Y., 2022. Infrared spectra and optical constants of astronomical ices: IV. Benzene and pyridine. *Icarus*, p. 114899.
- Jewitt, D. C. & Luu, J., 2004. Crystalline water ice on the Kuiper belt object (50000) Quaoar. *Nature*, 432(7018), pp. 731-733.
- Kofman, V., He, J., ten Kate, I. L. & Linnartz, H., 2019. The refractive index of amorphous and crystalline water ice in the UV-vis. *The Astrophysical Journal*, p. 131.
- Materese, C. K., Gerakines, P. A. & Hudson, R. L., 2020. The radiation stability of thymine in solid H<sub>2</sub>O. *Astrobiology*, 20(8), pp. 956-963.
- Materese, C. K., Nuevo, M. & Sandford, S. A., 2015. N- and O-heterocycles produced from the irradiation of benzene and naphthalene in H<sub>2</sub>O/NH<sub>3</sub>-containing ices. *The Astrophysical Journal*, p. 116.
- McMurtry, B. M., Turner, A. M., Saito, S. E. & Kaiser, R. I., 2016. On the formation of niacin (vitamin B<sub>3</sub>) and pyridine carboxylic acids in interstellar model ices. *Chemical Physics*, pp. 173-184.

- Mejía, C. et al., 2015. Compaction of porous ices rich in water by swift heavy ions. *Icarus*, pp. 222-229.
- Mejía, C. et al., 2015. Radiolysis and sputtering of carbon dioxide ice induced by swift Ti, Ni, and Xe ions. *Nuclear Instruments and Methods in Physics Research Section B: Beam Interactions with Materials and Atoms*, Volume 365, pp. 477-481.
- Mejía, C. et al., 2024. Modifications of astrophysical ices induced by cosmic rays-I. Water, carbon monoxide, and methanol mixtures. *Astronomy & Astrophysics*, Volume 687, p. A227.
- Mejía, C. et al., 2020. Radiolysis of Ices by Cosmic-Rays: CH<sub>4</sub> and H<sub>2</sub>O Ices Mixtures Irradiated by 40 MeV 58Ni<sup>11+</sup> Ions. *The Astrophysical Journal*, 894(2), p. 132.
- Mejía, C. et al., 2023. Swift heavy ion irradiation of thymine at cryogenic temperature. *Nuclear Instruments and Methods in Physics Research Section B: Beam Interactions with Materials and Atoms*, Volume 534, pp. 11-15.
- Moore, M. H. & Hudson, R. L., 1994. Far-infrared spectra of cosmic-type pure and mixed ices. *Astronomy and Astrophysics Suppl.*, Volume 103, pp. 45-56.
- Mootz, D. & Wussow, H. G., 1981. Crystal structures of pyridine and pyridine trihydrate. *The Journal of Chemical Physics*, 75(3), pp. 1517-1522.
- Morales, S. B. et al., 2011. A crossed molecular beam, low-temperature kinetics, and theoretical investigation of the reaction of the cyano radical (CN) with 1, 3-butadiene (C<sub>4</sub>H<sub>6</sub>). A route to complex nitrogen-bearing molecules in low-temperature extraterrestrial environments. *The Astrophysical Journal*, 742(1), p. 26.
- Muniz, G., 2017. *Irradiation of aromatic heterocyclic molecules at low temperature: a link to astrochemistry*. s.l.:PhD thesis.
- Öberg, K. I., Van Dishoeck, E. F., Linnartz, H. & Andersson, S., 2010. The effect of H<sub>2</sub>O on ice photochemistry. *The Astrophysical Journal*, 718(2), p. 832.
- Portugal, W. et al., 2014. Radiolysis of amino acids by heavy and energetic cosmic ray analogues in simulated space environments:  $\alpha$ -glycine zwitterion form. *Monthly Notices of the Royal Astronomical Society*, 441(4), pp. 3209-3225.
- Rachid, M. G. et al., 2021. Infrared spectra of complex organic molecules in astronomically relevant ice mixtures-IV. Methylamine. *Astronomy & Astrophysics*, Volume 653, p. A116.
- Rachid, M. G., Rocha, W. R. M. & Linnartz, H., 2022. Infrared spectra of complex organic molecules in astronomically relevant ice mixtures-V. methyl cyanide (acetonitrile). *Astronomy & Astrophysics*, Volume 665, p. A89.
- Rothard, H. et al., 2017. Modification of ices by cosmic rays and solar wind. *Journal of Physics B: Atomic, Molecular and Optical Physics*, 50(6), p. 062001.
- Smith, K. E. et al., 2014. Investigation of pyridine carboxylic acids in CM2 carbonaceous chondrites: Potential precursor molecules for ancient coenzymes. *Geochimica et Cosmochimica Acta*, pp. 1-12.



- Sun, B. J. et al., 2014. Theoretical study on reaction mechanism of ground-state cyano radical with 1, 3-butadiene: prospect of pyridine formation.. *The Journal of Physical Chemistry A*, 118(36), pp. 7715-7724.
- Theulé, P. et al., 2011. Hydrogenation of solid hydrogen cyanide HCN and methanimine CH<sub>2</sub>NH at low temperature. *Astronomy & Astrophysics*, Volume 534, p. A64.
- Timón, V., Maté, B., Herrero, V. J. & Tanarro, I., 2021. Infrared spectra of amorphous and crystalline urea ices. *Physical Chemistry Chemical Physics*, 23(39), pp. 22344-22351.
- Van Broekhuizen , F. A., Keane , J. V. & Schutte , W. A., 2004. A quantitative analysis of OCN-formation in interstellar ice analogs. *Astronomy & Astrophysics*, pp. 425-436.
- Ziegler, J. F., Ziegler, M. D. & Biersack, J. P., 2010. SRIM–The stopping and range of ions in matter. *Nuclear Instruments and Methods in Physics Research Section B: Beam Interactions with Materials and Atoms*, pp. 1818-1823.

## 4. Ion irradiation of pyrene ice

As highlighted in Section 1.1.2.1, PAHs are important carbon carriers in space, playing a significant role in galaxy evolution and planets formation. Although PAHs with sizes ranging from C<sub>50</sub> to C<sub>100</sub> are reported to be the most common in space (Allamandola, et al., 1989), smaller PAHs may also survive in icy grain mantles, as they are shielded from radiation in these environments. Here, the pyrene molecule (Figure 4.1) was selected as a suitable PAH representative, because it is one of the few well studied PAH molecules. Furthermore, from a technical point of view, pyrene is more convenient in experimental procedures than other PAHs. Moreover, pyrene was commonly detected in meteorites (Elsila, et al., 2005), (Basile, et al., 1984) and identified in the UV spectra of P/Halley comet (Clairemidi, et al., 2004). The possible formation pathway of pyrene from the reaction of 4-phenanthrenyl radical ([C<sub>14</sub>H<sub>9</sub>]<sup>•</sup>) with acetylene (C<sub>2</sub>H<sub>2</sub>) in carbon-rich circumstellar environment was demonstrated in the work of (Zhao, et al., 2018).

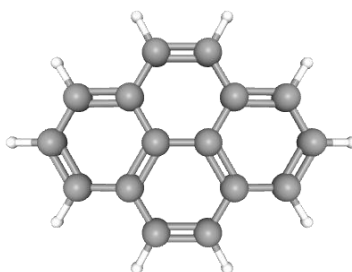


Figure 4.1. Schematic representation of pyrene (C<sub>16</sub>H<sub>10</sub>) molecule.

There is a significant amount of experimental and theoretical research focused on the UV irradiation of pyrene embedded in various matrices. In one of the pioneering studies on this topic (Bouwman, et al., 2010) demonstrated that pyrene exhibits a significantly higher ionization efficiency when trapped in a H<sub>2</sub>O matrix compared to a CO matrix. A follow-up investigation (Bouwman, et al., 2011) revealed that the conversion of neutral pyrene molecules into cations is enhanced at low pyrene concentrations in a water matrix. On the contrary, the conversion of neutral molecules into photoproducts was found to be more important at high pyrene concentrations. (Noble, et al., 2020) explored the influence of the water matrix structure on the photochemistry of anthracene, pyrene and coronene. Their findings indicate that the production of oxygenated PAHs is more efficient in porous amorphous water than in compact or crystalline water. In more organized matrices, PAHs are more likely to undergo fragmentation or dissipate energy within the icy mantle under UV irradiation. It has also been demonstrated that the matrix influences the final charge of pyrene under photon irradiation. For instance, in an ammonia matrix, pyrene anions are formed as a result of an electron donation process from ammonia-related species (Cuyllé, et al., 2012), (Ten Brinck, et al., 2022).

However, studies on the interaction of icy mantles containing pyrene with other types of cosmic radiation, including ions, are clearly absent in the literature. As mentioned in Chapter 1, GCR and SW particles, despite being less abundant than photons, can have a significant impact on icy mantles over astrophysical timescales. Therefore, in this chapter, we will first focus on a fundamental investigation of pure pyrene radiolysis under heavy ion bombardment. Subsequently, we will examine the impact of the water matrix and the concentration of pyrene within it on pyrene survivability.

## 4.1 Sample preparations

Pyrene irradiations were carried out with the IGLIAS setup at the IRRSUD beamline and at the ICA setup at the ATOMKI beamline. Pyrene is solid at room temperature. Therefore, ovens for evaporating pyrene powder were installed and used at both set-ups (IGLIAS and ICA). The temperature of the oven was set to at 48-54 °C for ICA setup and to 120-190 °C for the IGLIAS setup. The difference in temperature arises from the distinct layout and construction of the ovens. The target deposition and irradiation temperatures were the same across all experiments at a given facility, 10 K for the IGLIAS setup and 20 K for the ICA setup. Infrared spectra of pure pyrene and pyrene-water mixture (14 % of pyrene) are shown in Figure 4.2. Assignments, integrated ranges and band strengths of the pyrene bands are presented in Table 4.1. The values highlight in bold numbers were selected for the analysis in this study, as they correspond to different kinds of pyrene molecule vibrations: C-H out-of-plane bending ( $714\text{ cm}^{-1}$ ), C-C out of plane ring deformation ( $850, 1186\text{ cm}^{-1}$ ), C-C in-plane deformation ( $1435\text{ cm}^{-1}$ ) and C-H stretching ( $3051\text{ cm}^{-1}$ ). In the infrared spectrum of pyrene mixed with water a new band arises around  $3629\text{ cm}^{-1}$ , which is not observed neither in a pure water nor in a pure pyrene infrared spectrum. According to literature (Djomgoue & Njopwouo, 2013), (Geiger & Rossman, 2018), this band can be attributed to OH stretching vibrations.

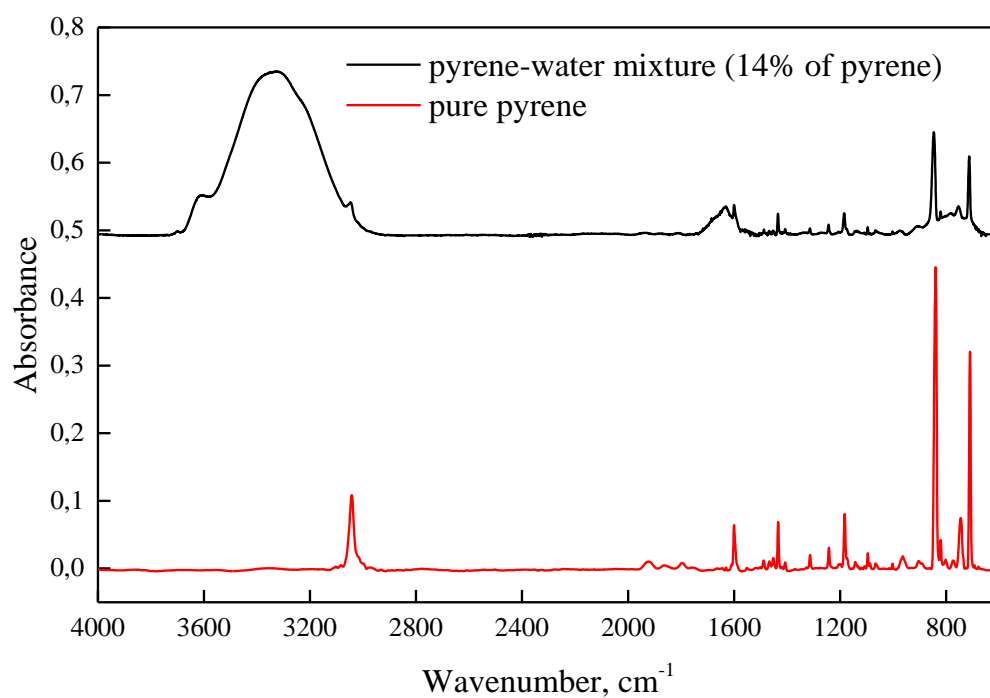


Figure 4.2. Infrared spectra of pure pyrene and pyrene mixture with water (14% of pyrene) obtained at ICA setup. The temperature for deposition and spectrum acquisition is 20 K.

Table 4.1. Pyrene infrared bands with assignments and corresponding integrating range and band strengths (Hardegree-Ullman , et al., 2014).

Wavenumber, $\text{cm}^{-1}$	Assignment	Integrated range	Avalue, $10^{-19}$ cm/molecule
<b>3051</b>	C-H stretching	3078-3032	60.36
1600	C=C in-plane ring stretching	1607-1584	33.56
1488		1493-1483	3.10
1468		1477-1463	3.80
1451		1460-1444	6.59
<b>1435</b>		1441-1426	28.28
1407	C-C in-plane ring stretching	1413-1402	3.71
1313		1321-1308	6.41
1244		1251-1235	13.08
<b>1186</b>		1194-1171	34.24
1096	C-H out-of-plane bending	1103-1091	7.62
1066		1072-1059	3.24
<b>850</b>	C-C out-of-plane ring deformation	864-837	191.25
821		826-817	7.05
<b>714</b>	C-H out-of-plane bending	722-700	140.73

## 4.2 Pure pyrene irradiations

In this section we will show results of pure pyrene irradiations with 11 different projectiles (5 elements). Table 4.2 summarizes experimental parameters. Column density calculations were made using eq. (2.6) with band strengths presented in Table 4.1. The column density values provided in Table 4.2 represent the mean for four bands (714, 850, 1186, 1435  $\text{cm}^{-1}$ ). The value for the 3051  $\text{cm}^{-1}$  band (C-H stretching) was excluded from the calculation of the column density, as it consistently returned results approximately 50% higher than those obtained for other bands did. The thickness of the samples were calculated using eq. (2.7), with the density of pyrene set at 1.27  $\text{g}/\text{cm}^3$ . The sample thicknesses ranged from 0.2 to 1.1  $\mu\text{m}$ . It was adjusted to ensure that ions possess nearly constant energy throughout their trajectory inside the sample. Stopping powers and penetration depths were calculated with the SRIM code (Ziegler, et al., 2010).

Table 4.2. Summary of the pure pyrene irradiations with 11 projectiles.

Ion	Energy, MeV	Energy, MeV/u	Setup/ Beamline	Electronic stopping power, keV/ $\mu\text{m}$	Nuclear stopping power, keV/ $\mu\text{m}$	Penetration depth, $\mu\text{m}$	Column density of pyrene, $10^{17} \text{ cm}^{-2}$	Initial thickness of the sample, $\mu\text{m}$	
$^1\text{H}^+$	2.0	2.0	ICA/ ATOMKI	19.69	0.012	60.8	3.63	0.96	
	0.8	0.8		36.76	0.03	14.0	3.88	1.03	
	0.2	0.2		84.65	0.091	2.09	3.27	0.87	
$^4\text{He}^{2+}$	0.4	0.1		273.1	0.67	2.08	0.79	0.21	
	0.8	0.2		273.5	0.38	3.51	1.35	0.36	
$^{12}\text{C}^{2+}$	2.0	0.167		969.3	3.56	3.14	3.23	0.86	
	2.4	0.2		1014	3.07	3.54	3.46	0.92	
$^{32}\text{S}^{2+}$	4.0	0.125		1933	27.4	3.38	1.41	0.37	
$^{32}\text{S}^{3+}$	6.4	0.2		2500	18.87	4.44	4.14	1.09	
$^{12}\text{C}^{4+}$	11.76	0.98		IGLIAS/ IRRSUD	886.5	0.79	12.86	3.07	0.81
$^{56}\text{Fe}^{10+}$	39.20	0.7		IRRSUD	5449	16.50	12.02	3.57	0.95

Figure 4.3 illustrated the evolution of the infrared spectra of pyrene under irradiation with 4 MeV  $^{32}\text{S}^{2+}$ . During irradiation, initial pyrene molecules undergo destruction and new species are formed. As previously mentioned, five bands were used to monitor the destruction of pyrene: 710, 850, 1186, 1435 and 3051  $\text{cm}^{-1}$ .

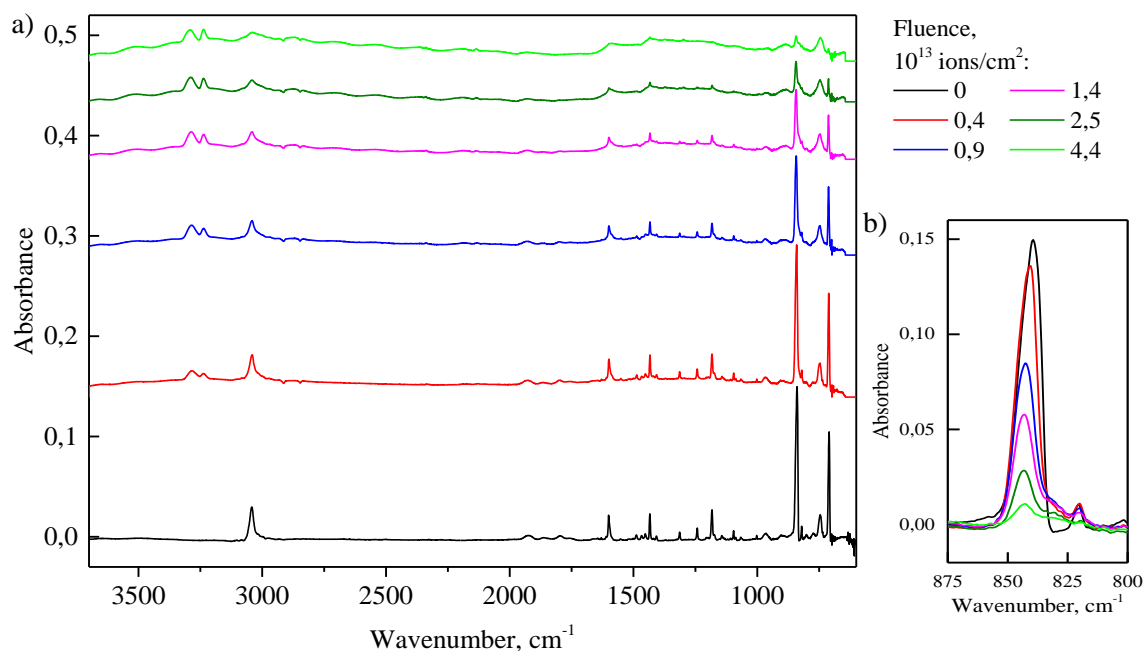


Figure 4.3. a) Evolution of the infrared spectra of pyrene irradiated at 20 K by 4 MeV  $^{32}\text{S}^{2+}$  at different fluences: unirradiated sample (black line),  $0.4 \cdot 10^{13}$  (red),  $0.9 \cdot 10^{13}$  (blue),  $1.4 \cdot 10^{13}$  (pink),  $2.5 \cdot 10^{13}$  (olive),  $4.4 \cdot 10^{13}$  (green); b) Evolution of the 850  $\text{cm}^{-1}$  pyrene band as a function of fluence.

Since in our experiments the electronic stopping power significantly predominates over nuclear stopping power, the pyrene destruction depends mainly on the electronic stopping power of the projectile. Experiments conducted with light ions typically require significantly more time compared to those with heavy ions, if the flux is roughly of the same order of magnitude. This is visually illustrated in Figure 4.4, which displays the evolution of the normalized  $1435\text{ cm}^{-1}$  peak area as a function of ion fluence for various projectiles. For ions with similar stopping power, the curves lie close to each other. For example,  $400\text{ keV } ^4\text{He}^{2+}$  or  $800\text{ keV } ^4\text{He}^{2+}$  or  $2\text{ MeV } ^{12}\text{C}^{2+}$  and  $2.4\text{ MeV } ^{12}\text{C}^{2+}$ .

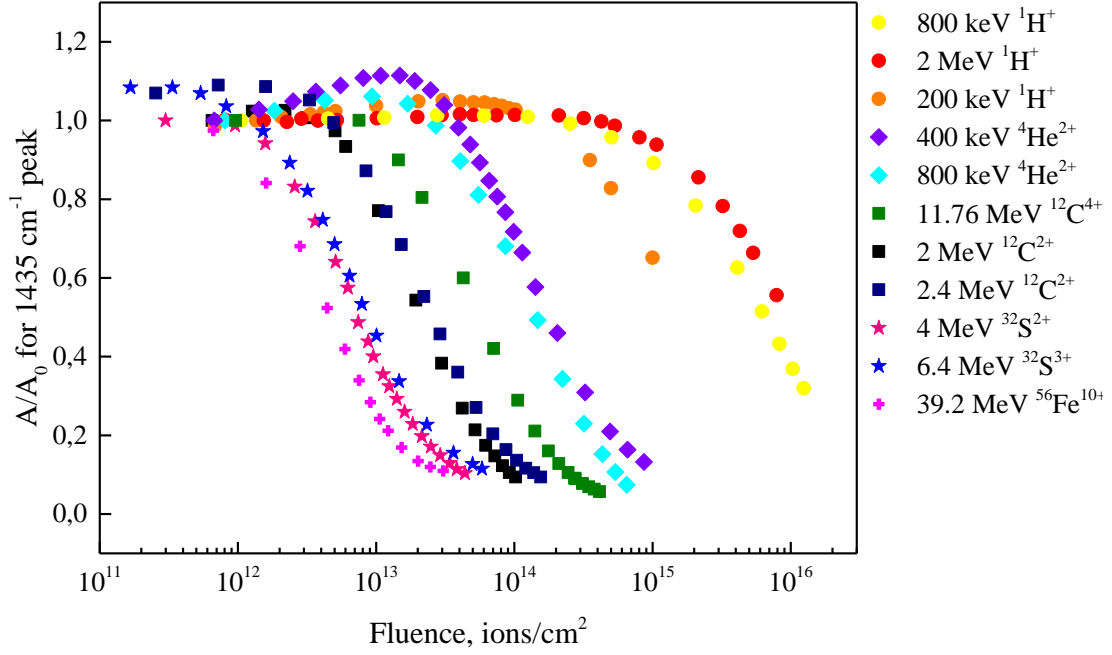


Figure 4.4. Normalized  $1435\text{ cm}^{-1}$  pyrene peak area as a function of fluence for different ions.

Figure 4.5 presents the column density evolution of pyrene bands during irradiation with  $4\text{ MeV } ^{32}\text{S}^{2+}$  as a function of ion fluence. At the beginning of irradiation, increasing column density is observed for some pyrene bands, which indicates compaction of the ice. The evolution of pyrene bands was fitted using eq. (3.1):

$$N(F) = N_0 e^{-\sigma_d F} - (N_0 - N_p) e^{-(\sigma_c + \sigma_d) F}.$$

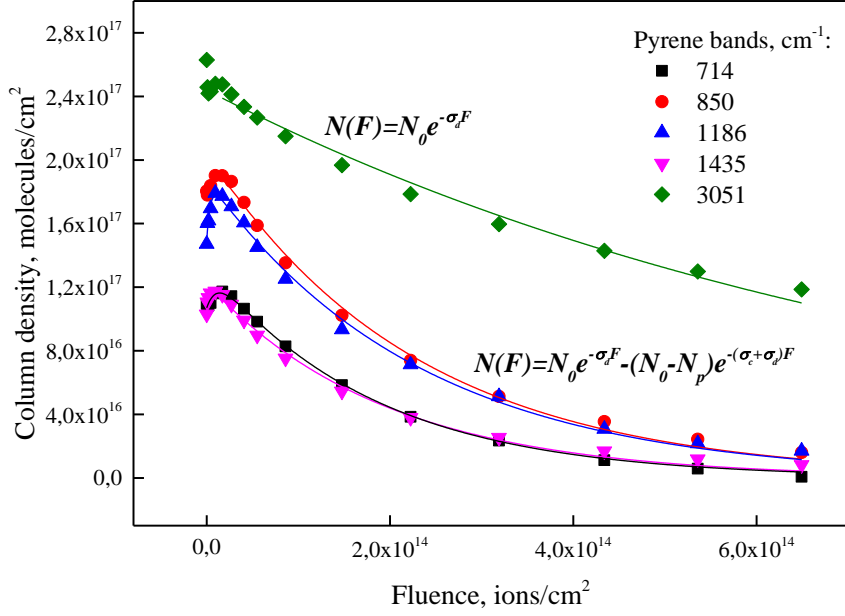


Figure 4.5. Fitting of the column density evolution for five pyrene bands as a function of 800 keV  ${}^4\text{He}^{2+}$  fluence.

Table 4.3. Destruction cross section of pyrene

Ion	Energy, MeV	Destruction cross section, $\text{cm}^2$					Mean $\pm$ SD
		710 $\text{cm}^{-1}$	850 $\text{cm}^{-1}$	1186 $\text{cm}^{-1}$	1435 $\text{cm}^{-1}$	3051 $\text{cm}^{-1}$	
${}^1\text{H}^+$	2.0	$8.77 \cdot 10^{-17}$	$8.11 \cdot 10^{-17}$	$8.18 \cdot 10^{-17}$	$8.10 \cdot 10^{-17}$	$3.61 \cdot 10^{-17}$	$7.35 \pm 2.11 \cdot 10^{-17}$
	0.8	$11.01 \cdot 10^{-17}$	$9.36 \cdot 10^{-17}$	$7.69 \cdot 10^{-17}$	$10.23 \cdot 10^{-17}$	$3.62 \cdot 10^{-17}$	$8.38 \pm 2.93 \cdot 10^{-17}$
	0.2	$5.84 \cdot 10^{-16}$	$5.39 \cdot 10^{-16}$	$5.49 \cdot 10^{-16}$	$5.02 \cdot 10^{-16}$	$2.99 \cdot 10^{-16}$	$4.95 \pm 1.13 \cdot 10^{-16}$
${}^4\text{He}^{2+}$	0.4	$4.19 \cdot 10^{-15}$	$3.65 \cdot 10^{-15}$	$3.55 \cdot 10^{-15}$	$4.14 \cdot 10^{-15}$	$0.91 \cdot 10^{-15}$	$3.29 \pm 1.36 \cdot 10^{-15}$
	0.8	$5.51 \cdot 10^{-15}$	$4.38 \cdot 10^{-15}$	$4.29 \cdot 10^{-15}$	$5.13 \cdot 10^{-15}$	$1.23 \cdot 10^{-15}$	$4.11 \pm 1.69 \cdot 10^{-15}$
${}^{12}\text{C}^{2+}$	2.0	$3.12 \cdot 10^{-14}$	$2.95 \cdot 10^{-14}$	$2.39 \cdot 10^{-14}$	$3.18 \cdot 10^{-14}$	$0.90 \cdot 10^{-14}$	$9.26 \pm 3.73 \cdot 10^{-15}$
	2.4	$3.02 \cdot 10^{-14}$	$2.53 \cdot 10^{-14}$	$2.68 \cdot 10^{-14}$	$2.68 \cdot 10^{-14}$	$0.94 \cdot 10^{-14}$	$2.51 \pm 0.95 \cdot 10^{-14}$
${}^{32}\text{S}^{2+}$	4.0	$9.74 \cdot 10^{-14}$	$8.47 \cdot 10^{-14}$	$9.22 \cdot 10^{-14}$	$8.43 \cdot 10^{-14}$	$4.54 \cdot 10^{-14}$	$2.37 \pm 0.82 \cdot 10^{-14}$
${}^{32}\text{S}^{3+}$	6.4	$9.14 \cdot 10^{-14}$	$8.11 \cdot 10^{-14}$	$9.24 \cdot 10^{-14}$	$7.97 \cdot 10^{-14}$	$4.94 \cdot 10^{-14}$	$8.08 \pm 2.05 \cdot 10^{-14}$
${}^{12}\text{C}^{4+}$	11.76	$1.23 \cdot 10^{-14}$	$0.99 \cdot 10^{-14}$	$1.02 \cdot 10^{-14}$	$1.11 \cdot 10^{-14}$	$0.28 \cdot 10^{-14}$	$7.88 \pm 1.74 \cdot 10^{-14}$
${}^{56}\text{Fe}^{10+}$	39.20	$1.59 \cdot 10^{-13}$	$1.31 \cdot 10^{-13}$	$1.58 \cdot 10^{-13}$	$1.37 \cdot 10^{-13}$	$1.16 \cdot 10^{-13}$	$1.40 \pm 0.18 \cdot 10^{-13}$

Table 4.3 represents destruction cross section values, calculated for five pyrene bands in all experiments. It is worth noting that the values for the 3051  $\text{cm}^{-1}$  peak, which corresponds to the CH stretch motion, are consistently smaller than those obtained for the other four peaks. Therefore, alongside the mean value in the last column, the standard deviation is provided.

Destruction cross section of pyrene as a function of projectile's electronic stopping power is presented in Figure 4.6. The values for destruction cross section were extracted from the "average" column of Table 4.3. The error bars correspond to standard deviation (Section 3.3). The relation between destruction cross section and electronic stopping power for the pyrene molecule is again well described with a power function (eq. (3.2)). The coefficients for

C and n equal to  $7.12 \cdot 10^{-19}$  and  $1.46 \pm 0.07$  were derived from the approximation. This information will be used for half-life time calculations of pyrene in Chapter 6.

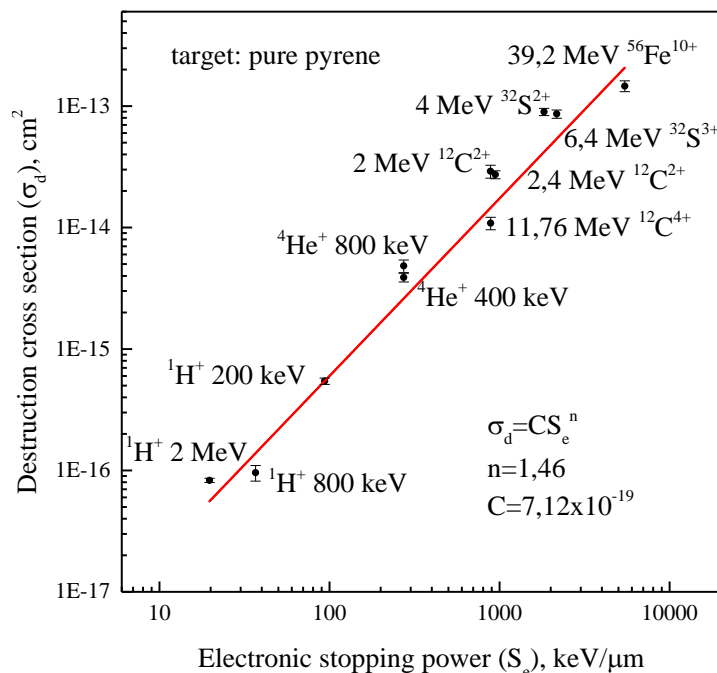


Figure 4.6. Destruction cross section as a function of electronic stopping power for pure pyrene at 20 K. The value of the destruction cross section is the average across five peaks ( $1030, 1068, 1438, 1483, 3051 \text{ cm}^{-1}$ ), with error bars corresponding to the standard deviation.

Table 4.4 presents the compaction cross section for pyrene bands and the compaction dose in experiments conducted at ATOMKI. In the experiments conducted at GANIL, no compaction was observed. The compaction dose varies significantly between projectiles, likely because the intervals between the irradiations were too large. The average value of compaction dose is 5.79 eV/molecule across nine projectiles. This value is more than ten times higher than the compaction cross section for pyridine, which is 0.46 eV/molecules, as obtained in Chapter 3, and more than twenty times higher than the compaction cross section of water, which is around 0.2 eV/molecule. This can be attributed to the molecular size effect: the bigger the molecule, the more energy is needed for compaction. Additionally, we found that the compaction cross section increases with the increase in the electronic stopping power of the projectile (Figure 4.10). A similar pattern was proposed in the literature (Dartois, et al., 2013) and (Mejía, et al., 2015).



Table 4.4. Compaction cross section for pyrene bands.

Ion	Energy, MeV	Compaction cross section, cm <sup>2</sup>					Compaction dose, eV/molecule
		714 cm <sup>-1</sup>	850 cm <sup>-1</sup>	1186 cm <sup>-1</sup>	1435 cm <sup>-1</sup>	Mean±SD	
<sup>1</sup> H <sup>+</sup>	2.0	-	-	7.38·10 <sup>-14</sup>	2.67·10 <sup>-14</sup>	5.03±3.33·10 <sup>-14</sup>	1.83
	0.8	-	-	8.78·10 <sup>-14</sup>	4.21·10 <sup>-13</sup>	2.54±2.35·10 <sup>-13</sup>	5.72
	0.2	-	-	1.95·10 <sup>-13</sup>	1.02·10 <sup>-13</sup>	1.49±0.65·10 <sup>-13</sup>	5.69
<sup>4</sup> He <sup>2+</sup>	0.4	1.90·10 <sup>-13</sup>	1.73·10 <sup>-13</sup>	2.44·10 <sup>-13</sup>	3.38·10 <sup>-13</sup>	2.36±0.74·10 <sup>-13</sup>	11.52
	0.8	9.62·10 <sup>-14</sup>	1.48·10 <sup>-13</sup>	2.71·10 <sup>-13</sup>	4.95·10 <sup>-13</sup>	2.53±1.77·10 <sup>-13</sup>	9.53
<sup>12</sup> C <sup>2+</sup>	2.0	6.01·10 <sup>-13</sup>	-	1.61·10 <sup>-12</sup>	1.56·10 <sup>-12</sup>	1.26±0.57·10 <sup>-12</sup>	6.45
	2.4	-	1.59·10 <sup>-12</sup>	2.25·10 <sup>-12</sup>	5.77·10 <sup>-12</sup>	3.20±2.25·10 <sup>-12</sup>	4.66
<sup>32</sup> S <sup>2+</sup>	4.0	1.68·10 <sup>-12</sup>	2.19·10 <sup>-12</sup>	4.43·10 <sup>-12</sup>	-	2.77±1.46·10 <sup>-12</sup>	4.92
<sup>32</sup> S <sup>3+</sup>	6.4	2.55·10 <sup>-12</sup>	2.88·10 <sup>-12</sup>	5.89·10 <sup>-12</sup>	-	3.77±1.84·10 <sup>-12</sup>	1.78

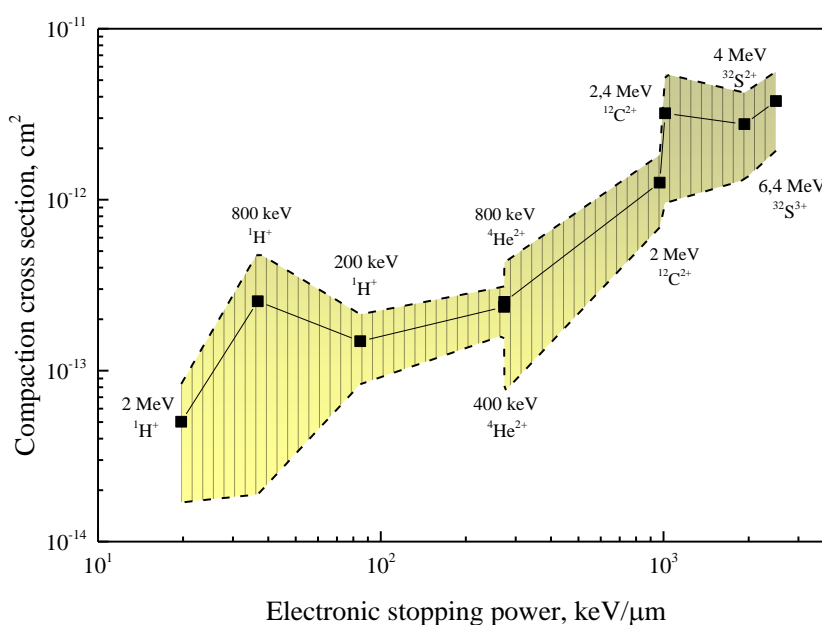


Figure 4.7. Mean compaction cross section across four pyrene bands for different projectiles, with associated standard deviation.

#### 4.2.1 Pyrene destruction as a function of deposited local dose

We then examined the evolution of the normalized peak area as a function of the deposited dose, as the literature indicates that the deposited dose is a key parameter: the normalized peak area follows the same trend regardless of the projectile. The study (da Costa, et al., 2020) presented results on the irradiation of the aliphatic molecule valine with 1.5 MeV H<sup>+</sup>, He<sup>+</sup>, N<sup>+</sup>, and 230 MeV S<sup>15+</sup> ions. The normalized absorbance of one of the valine infrared bands as a function of the deposited dose followed the same trend for different projectiles (Figure 4.8a). A similar result was obtained in another study, (Muniz, 2017) focused on the irradiation of the cyclic molecule cytosine with heavy ions 17 MeV Ni<sup>8+</sup>, 190 MeV Ca<sup>10+</sup>, 92 MeV Xe<sup>23+</sup>, 116 MeV U<sup>32+</sup> (Figure 4.8b).

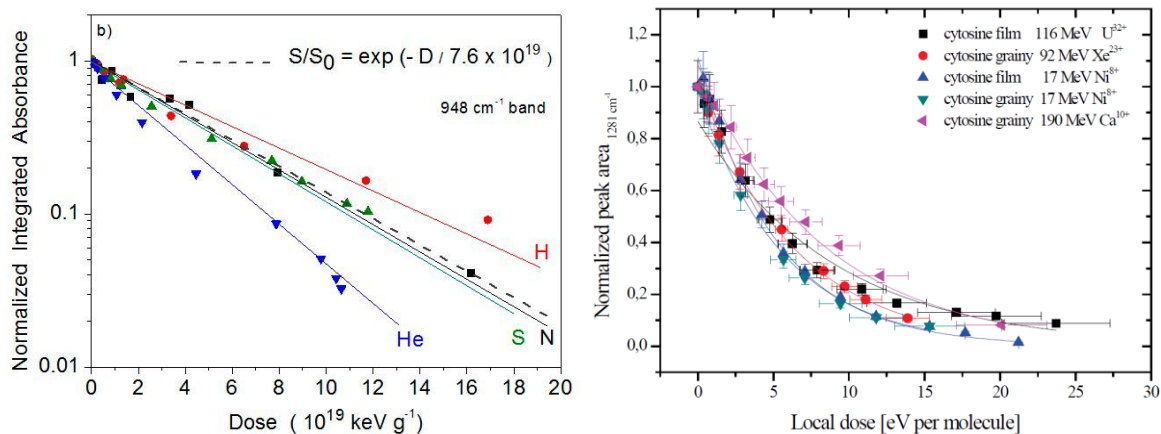


Figure 4.8. Normalized peak area as a function of local dose for a) cytosine and b) valine molecules, irradiated with different ions. Extracted from a) (da Costa, et al., 2020), b) (Muniz, 2017).

Figure 4.9 shows the evolution of five pyrene bands as a function of the local dose, calculated using eq. (2.8). We obtained an unexpected result, as the curves did not follow the same trend, especially for light projectiles (H and He), in contrast to the above cited previous studies. The destruction of pyrene is significantly lower when exposed to weakly ionizing projectiles compared to heavy ions for the same deposited dose. The curves corresponding to He and 11.76 MeV  $^{12}\text{C}^{4+}$  fall between those for protons and other ions. The remaining (heavy) ions follow more or less the same trend for all bands, except for the band at  $3051\text{ cm}^{-1}$ . However, as previously noted, the behaviour of this band often deviates from the others.

We investigated whether this effect also applies to the adenine ( $\text{C}_5\text{H}_5\text{N}_5$ ) molecule. To determine this, we examined previous experiments on the irradiation of pure adenine conducted at GANIL, ATOMKI and GSI-UNILAC (Darmstadt, Germany) facilities. The results obtained in these experiments were partially published in (Vignoli Muniz, et al., 2017) and (Bibang, 2021). Figure 4.10 shows the evolution of the normalized area of two adenine bands ( $914$  and  $1333\text{ cm}^{-1}$ ) as a function of deposited local dose for adenine irradiated with different projectiles. As evident from the graph, H and He destroy significantly less amount of adenine than heavy ions, starting from C. Therefore, we can conclude that this effect is also valid for the nucleobase adenine, which contains two aromatic rings (the structure is shown in Figure 4.10).

As was mentioned before, in our experiments, the projectile primarily loses its energy by transferring it to the electrons of the target material. The effect observed in Figure 4.9 can be attributed to the fact that the deposited dose value does not take into account the way of how ions transfer the energy to the electrons of the matter. Indeed, whereas light ions induce separated ionization events around the ion trajectory, heavy ions induce multiple simultaneous ionization and secondary cascades induced by fast  $\delta$ -electrons. Figure 4.10 presents ionization tracks, produced by different ions (Powell, et al., 1959). It is clear that heavy ions, starting with C, form continuous ionization tracks. However, for H and He ions, this is not the case. Additionally, this figure indicates that the greater the ion mass, the further the damage extends from the track. The damage distant from the track is caused by  $\delta$  electrons, which can possess relatively high (keV) energies (Krasheninnikov & Nordlund, 2010).

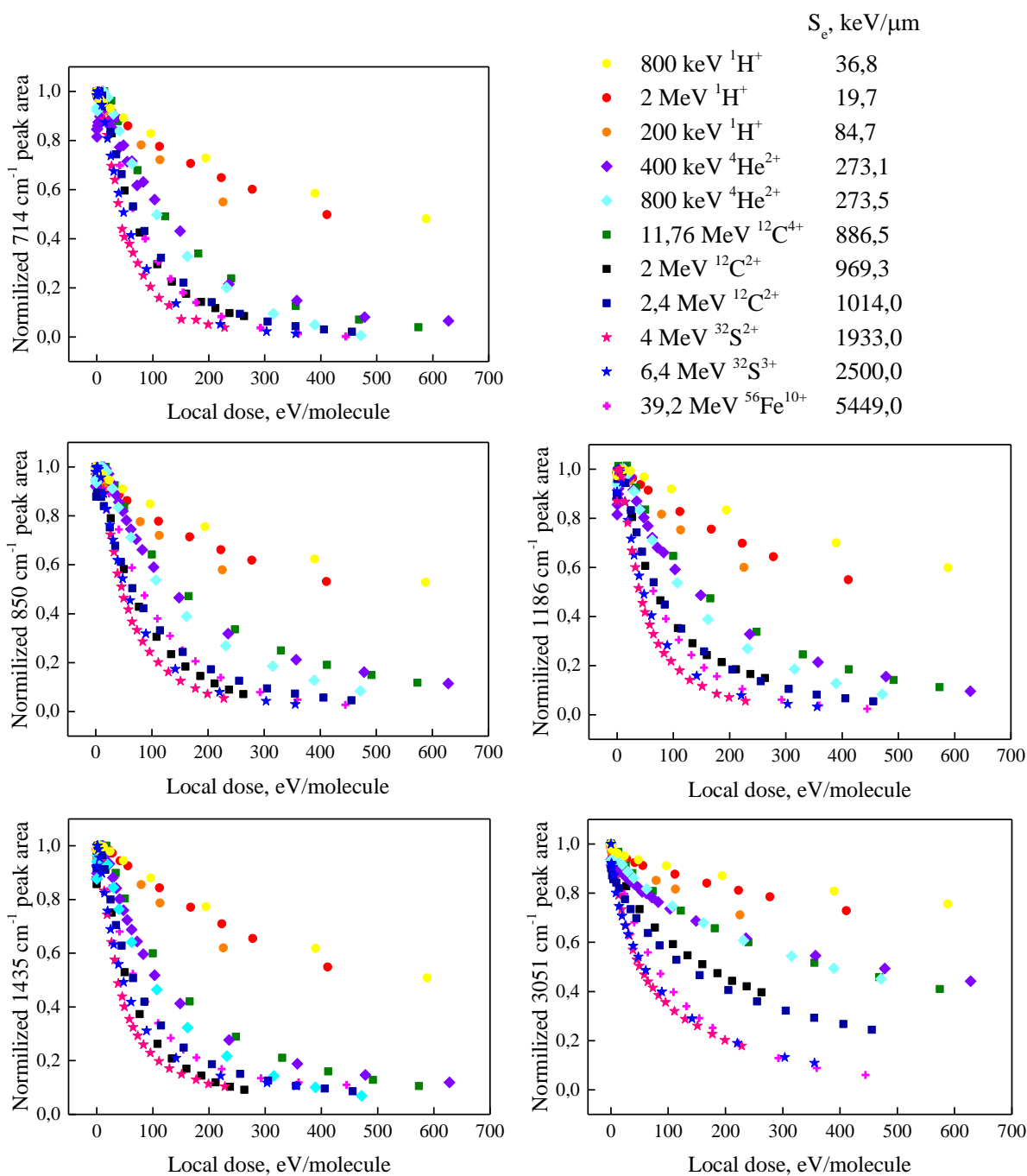


Figure 4.9. Normalized peak area as a function of deposited dose for different pyrene bands: a)  $710\text{ cm}^{-1}$ , b)  $850\text{ cm}^{-1}$ , c)  $1186\text{ cm}^{-1}$ , d)  $1435\text{ cm}^{-1}$ , e)  $3051\text{ cm}^{-1}$  in eleven experiments

The greater damage of aromatic structures induced by heavy ions compare to electrons was reported in the work (Balanzat, et al., 1995). It was postulated that the deposited dose is highly inhomogeneous in the case of heavy ions, resulting in the multiple ionization of aromatic rings (Balanzat, et al., 1995). Additionally, the amount of energy deposited locally is significant, reaching several keV per nm. However, to gain a more comprehensive understanding of the effect shown in Figure 4.9, additional investigations of the track structure by e.g. numerical simulations are required.

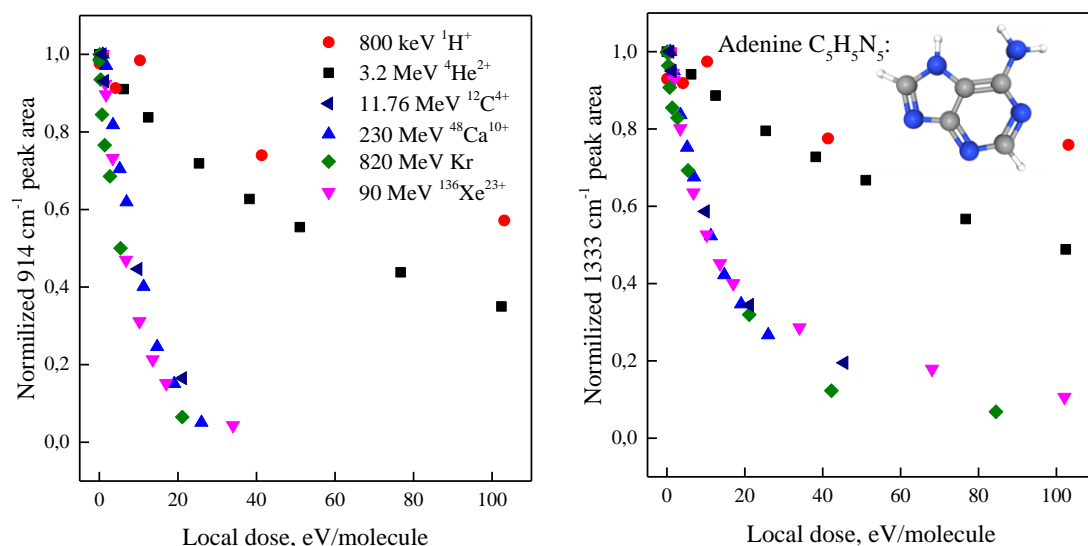


Figure 4.10. Normalized peak area evolution of 914 and 1333  $\text{cm}^{-1}$  adenine bands as a function of local dose during irradiation with different ions.

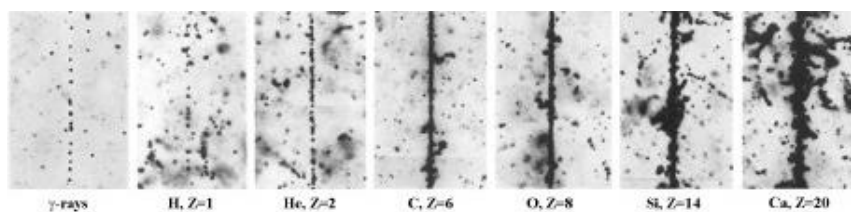


Figure 4.11. Electron production by  $\gamma$ -rays and different ions, moving at relativistic velocities. The images were obtained using electron sensitive emulsion. Extracted from (Powell, et al., 1959).

We irradiated amorphous pyrene with 11 different projectiles and derived the coefficients for the power dependence of the destruction cross section as a function of electronic stopping power. This will allow us to estimate the half-life time of pyrene in dense clouds. We also determined that the compaction cross section of pyrene is 10 times higher than that of pyridine and 20 times higher than that of water, which we attributed to the size effect. Additionally, we found that the compaction cross section increases with the electronic stopping power of the projectile. We also observed an interesting and unexpected effect: for the same deposited dose, protons cause significantly less damage than heavy ions.

### 4.3 Results on pyrene-water irradiations

As mentioned earlier, PAHs exist in space not only in form of solid grains, but also can freeze out in icy mantles as guest molecules (Bouwman, et al., 2011). In this case, the matrix influences significantly their survivability. Therefore, similar to the experiments with pyridine, we conducted experiments where pyrene was embedded in the water matrix, as water is the most abundant molecule in icy mantles (Gibb, et al., 2004).

Pyrene-water mixtures with different concentrations were irradiated with three projectiles: 39.2 MeV  $^{56}\text{Fe}^{10+}$ , 2 MeV  $^{12}\text{C}^{2+}$ , 200 keV  $^1\text{H}^+$  at IGLIAS and ICA setups. As previously mentioned, all mixtures were prepared at low temperatures (10-20 K), leading to the formation of an amorphous structure. The summary of the experiments is presented in Table

4.5. The column density of pyrene specified in Table 4.5 represents the mean value from the four pyrene bands (710, 850, 1186, 1435  $\text{cm}^{-1}$ ). The 3051  $\text{cm}^{-1}$  pyrene band was not used in the calculations or analysis, as it overlaps with the biggest water band near 3280  $\text{cm}^{-1}$ . For calculations of water column density, only the 3280  $\text{cm}^{-1}$  band was used, with an Avalue of  $2 \cdot 10^{-16}$   $\text{cm}/\text{molecule}$ . The pyrene concentration was calculated as the ratio of the column density of pyrene to the sum of the column densities of pyrene and water. Stopping powers and penetration depths were calculated using the SRIM code (Ziegler, et al., 2010). As in previous experiments, the penetration depth was significantly greater than the sample thickness.

Table 4.5. Experimental parameters of pyrene-water mixtures irradiations.

Ion	Setup/ Beamline	Pyrene concentration, %	Electronic stopping power, $\text{keV}/\mu\text{m}$	Nuclear stopping power, $\text{keV}/\mu\text{m}$	Penetration depth, $\mu\text{m}$	Column density of pyrene, $10^{17} \text{cm}^{-2}$	Column density of water, $10^{17} \text{cm}^{-2}$	Initial thickness of the sample, $\mu\text{m}$
200 keV $^1\text{H}^+$	ICA/ ATOMKI	3.5	64.65	0.0758	2.77	0.69	18.79	0.78
		14	66.37	0.0745	2.69	1.56	9.66	0.72
		32.5	70.09	0.0766	2.53	1.67	3.47	0.55
		100	84.65	0.091	2.09	3.27	-	0.87
2 MeV $^{12}\text{C}^{2+}$	ICA/ ATOMKI	1	721.4	2.978	4.89	0.21	20.23	0.69
		4	728.6	2.932	4.66	0.83	18.4	0.81
		30	795.7	3.016	3.95	2.73	6.09	0.93
		100	969.3	3.56	3.14	969.3	-	0.86
39.2 MeV $^{56}\text{Fe}^{10+}$	IGLIAS/ IRRSUD	0.3	4360	13.86	16.60	0.057	17.13	0.56
		4	4320	13.55	16.25	0.291	7.26	0.31
		6	4572	14.23	15.58	0.196	3.07	0.15
		100	5449	16.50	12.02	3.57	-	0.95

Figure 4.12 illustrates the evolution of the infrared spectra of the mixtures under irradiation. The spectra before (black line) and after irradiation (red line) of a) pyrene:H<sub>2</sub>O (4% of pyrene) mixture with  $7.8 \cdot 10^{12}$  ions of  $^{56}\text{Fe}^{10+}$  and b) pyrene:H<sub>2</sub>O (32.5% of pyrene) mixture with  $4.02 \cdot 10^{15}$  ions of 200 keV  $^1\text{H}^+$ . In both cases, it is evident that the amount of pyrene decreases during irradiation, while the quantity of water remains almost unchanged. This phenomenon can be attributed to the much higher resistance of water ice to radiation compared to pyrene. Furthermore, there is noticeable emergence of new compounds, which will be discussed in the following section.

The destruction of pyrene in pyrene-water mixtures was examined in the same manner as for pure pyrene. The decrease in column density was approximated with eq. (3.1). However, similar to the case with pyridine-water mixtures, the compaction is insignificant. Therefore, in the first approximation, only the destruction is taken into account:

$$N(F) = N_0 e^{-\sigma_a F} \quad \text{eq. (4.1)}$$

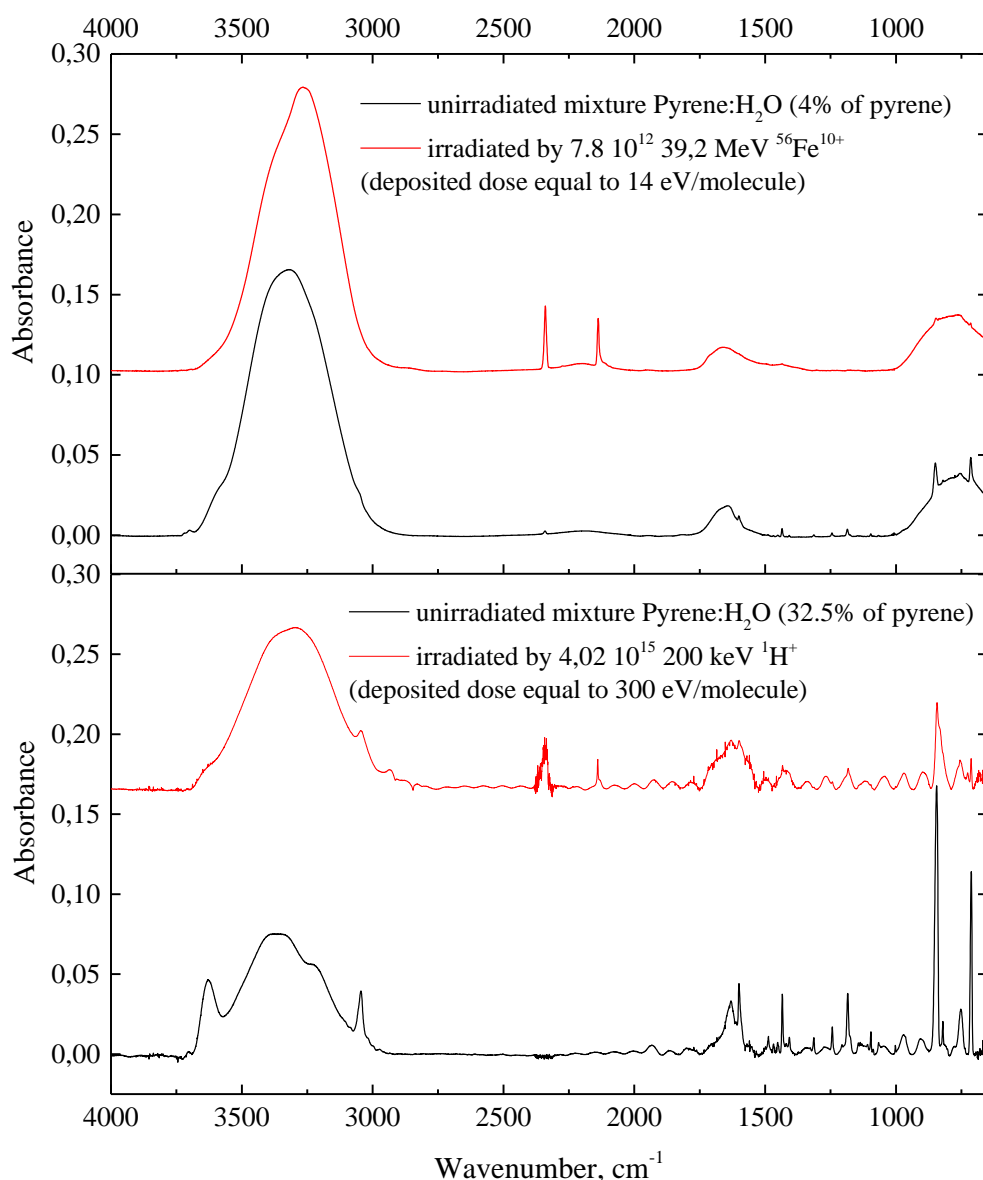


Figure 4.12. Infrared spectra of pyrene-water mixtures a) 4% of pyrene and b) 32.5% of pyrene before irradiation (black line) and after irradiation (red line) by a)  $7.8 \cdot 10^{12}$  39.2 MeV  $^{56}\text{Fe}^{10+}$  with deposited dose equal to 14 eV/molecule, and by b)  $4.02 \cdot 10^{15}$  200 keV  $^1\text{H}^+$  with deposited dose equal to 300 eV/molecule

Table 4.6 presents the results on the destruction cross section of pyrene in the water matrix. For clarity, the destruction cross section of pure pyrene is also included. Figure 4.13 presents the destruction cross section as a function of pyrene concentration in pyrene-water mixtures exposed to different ion irradiation. As with the experiments involving the pyridine molecule, presented in Chapter 3, there is a clear tendency towards higher destruction cross sections at lower pyrene concentrations. This phenomenon is likely to occur due to an indirect effect, which means that the ions induce the dissociation of water molecules, and the resulting water radicals subsequently attack the pyrene molecules. This effect has also been observed for other molecules embedded in a water matrix and exposed to ion irradiation. Examples are proton irradiation of thymine-water mixtures (Materese, et al., 2020) and methane-water mixtures irradiated with heavy ions (Mejía, et al., 2020). There is also a significant amount of

research on UV irradiation of ices, where this effect was also observed. (Öberg, et al., 2010) found that the photodestruction cross section of NH<sub>3</sub> and CH<sub>4</sub> increases up to a factor 10 in mixtures with water. (Cuyllé, et al., 2014) reported that the ionization yield of pyrene, trapped in water ice at a concentration of 0.008% is five times higher than at a concentration of 1.25%. These results were explained in studies by (Gudipati & Allamandola, 2004) and (Woon & Park, 2004). They demonstrated that the ionization potential of PAHs trapped in a water matrix is approximately 2 eV lower than that of pure PAHs.

Table 4.6. Destruction cross section of pyrene in the pyrene-water mixtures irradiated with different ions

Ion	Setup/ Beamline	Percentage of pyrene, %	Destruction cross section of pyrene, cm <sup>2</sup>				
			710 cm <sup>-1</sup>	850 cm <sup>-1</sup>	1186 cm <sup>-1</sup>	1435 cm <sup>-1</sup>	Mean
200 keV <sup>1</sup> H <sup>+</sup>		3.5	2.11·10 <sup>-15</sup>	1.15·10 <sup>-15</sup>	4.01·10 <sup>-15</sup>	3.25·10 <sup>-15</sup>	2.63·10 <sup>-15</sup>
		14	9.37·10 <sup>-16</sup>	7.63·10 <sup>-16</sup>	1.07·10 <sup>-15</sup>	1.13·10 <sup>-15</sup>	1.03·10 <sup>-15</sup>
		32.5	6.44·10 <sup>-16</sup>	4.10·10 <sup>-16</sup>	4.79·10 <sup>-16</sup>	5.79·10 <sup>-16</sup>	5.28·10 <sup>-16</sup>
		100	5.84·10 <sup>-16</sup>	5.39·10 <sup>-16</sup>	5.49·10 <sup>-16</sup>	5.02·10 <sup>-16</sup>	5.43·10 <sup>-16</sup>
2 MeV <sup>12</sup> C <sup>2+</sup>	ICA/ ATOMKI	1	5.03·10 <sup>-14</sup>	4.19·10 <sup>-14</sup>	1.21·10 <sup>-13</sup>	9.76·10 <sup>-14</sup>	7.77·10 <sup>-14</sup>
		4	4.16·10 <sup>-14</sup>	4.58·10 <sup>-14</sup>	1.09·10 <sup>-13</sup>	6.81·10 <sup>-14</sup>	6.62·10 <sup>-14</sup>
		30	4.02·10 <sup>-14</sup>	3.25·10 <sup>-14</sup>	3.82·10 <sup>-14</sup>	2.57·10 <sup>-14</sup>	3.42·10 <sup>-14</sup>
		100	3.11·10 <sup>-14</sup>	2.95·10 <sup>-14</sup>	2.39·10 <sup>-14</sup>	3.18·10 <sup>-14</sup>	2.91·10 <sup>-14</sup>
39,2 MeV <sup>56</sup> Fe <sup>10+</sup>	IGLIAS/ IRRSUD	0.3	1.59·10 <sup>-12</sup>	7.37·10 <sup>-13</sup>	1.59·10 <sup>-12</sup>	1.61·10 <sup>-12</sup>	1.38·10 <sup>-12</sup>
		4	4.77·10 <sup>-13</sup>	2.79·10 <sup>-13</sup>	3.30·10 <sup>-13</sup>	2.62·10 <sup>-13</sup>	3.37·10 <sup>-13</sup>
		6	2.93·10 <sup>-13</sup>	2.02·10 <sup>-13</sup>	3.09·10 <sup>-13</sup>	1.87·10 <sup>-13</sup>	2.48·10 <sup>-13</sup>
		100	1.59·10 <sup>-13</sup>	1.31·10 <sup>-13</sup>	1.57·10 <sup>-13</sup>	1.37·10 <sup>-13</sup>	1.46·10 <sup>-13</sup>

To estimate the half-life time of pyrene trapped in water matrix, we selected two reference concentrations of pyrene in H<sub>2</sub>O:C<sub>16</sub>H<sub>10</sub> mixture: 1% and 5%. In reality, the concentration of PAHs in icy mantles is probably much lower, below 0.1%. However, conducting experiments with such low concentrations is not feasible, as pyrene would not be detectable in the IR spectrum. Therefore, 1% and 5% are optimal values that will allow assessing how the half-life of pyrene changes in the presence of the water matrix. Since precisely achieving these concentrations during sample preparation is challenging, we used a fitting method to evaluate the destruction cross section specifically for the 1% and 5% pyrene concentrations. The exponential function was used because it provides the best fit, although there is no physical meaning behind:

$$\sigma_d(x) = a - b \cdot c^x \quad \text{eq. (4.1)}$$

where  $x$  is pyrene concentration in percentage % (from 0 to 100),  $a$ ,  $b$  and  $c$  are the fitting parameters. The example of the fitting is shown in Figure 4.14. The average destruction cross section values for pyrene across four bands, at concentrations of 1% and 5% in the H<sub>2</sub>O:C<sub>16</sub>H<sub>10</sub> mixture are presented in Table 4.7. Figure 4.15 illustrates the fitting of the destruction cross section of pyrene as a function of the electronic stopping power of the projectile for the H<sub>2</sub>O:C<sub>16</sub>H<sub>10</sub> mixtures (1 and 5 % of pyrene). These fittings will be used in Chapter 6 for half-life time calculations.

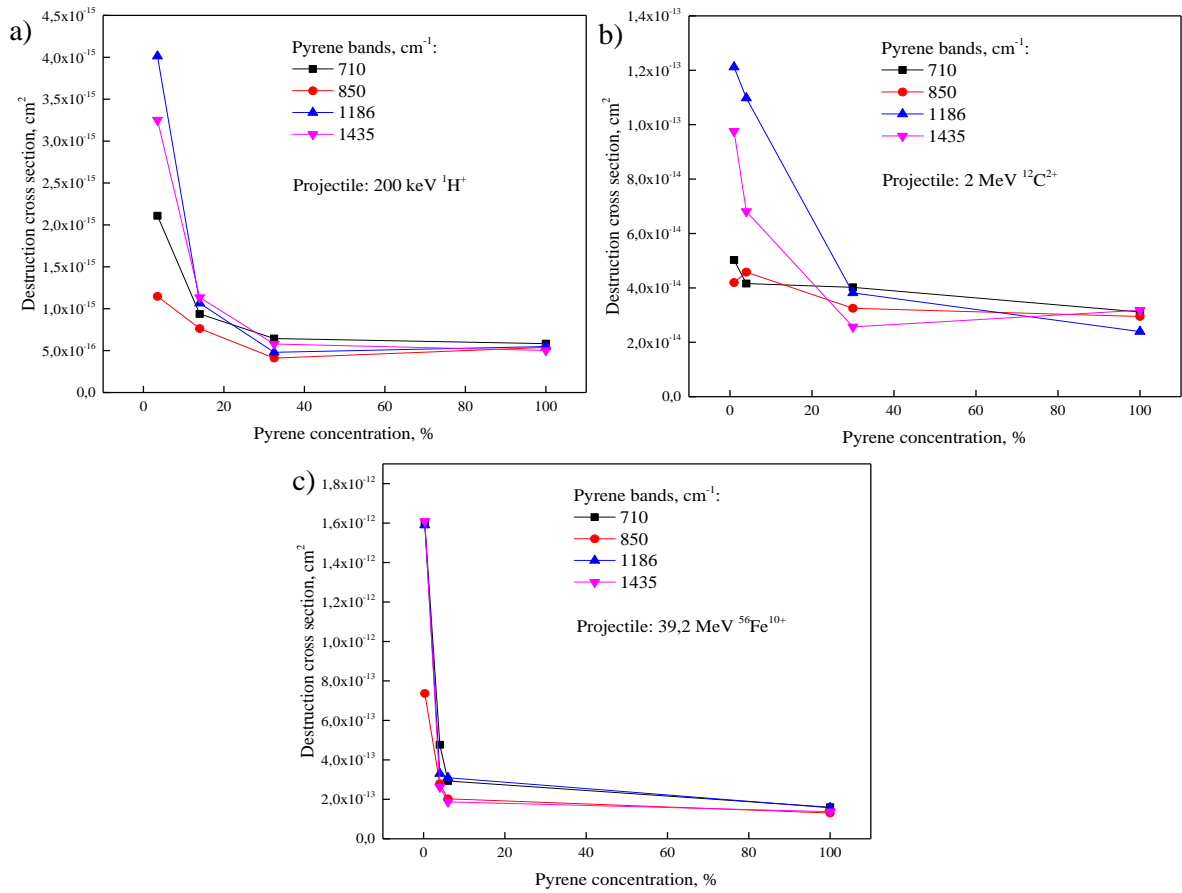


Figure. 4.13. Destruction cross section of pyrene in pyrene-water mixtures as a function of pyrene concentration in the mixture. The mixtures were irradiated by a) 200 keV <sup>1</sup>H<sup>+</sup>, b) 2 MeV <sup>12</sup>C<sup>2+</sup>, c) 39.2 MeV <sup>56</sup>Fe<sup>10+</sup>.

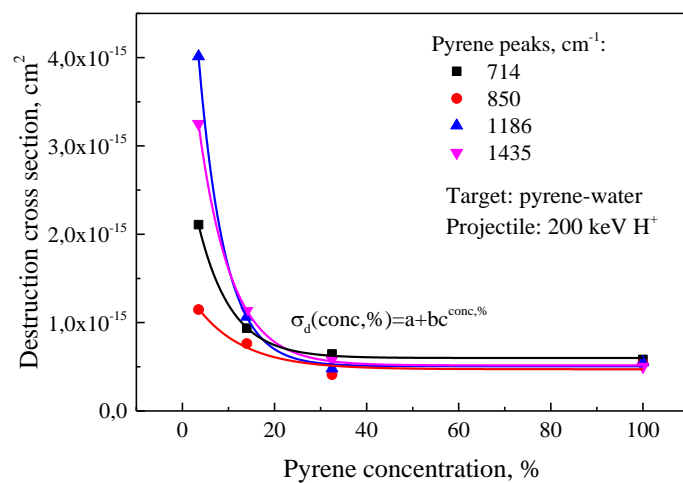


Figure 4.14. Fitting of destruction cross section as a function of pyrene concentration.



Table 4.7. Destruction cross section of pure pyrene and of pyrene in the  $H_2O:C_{16}H_{10}$  mixture ( $cm^2$ ).

Mixture \ Projectile	200 keV $^1H^+$	2 MeV $^{12}C^{2+}$	39.2 MeV $^{56}Fe^{10+}$
Pure pyrene	$5.44 \cdot 10^{-16}$	$2.91 \cdot 10^{-14}$	$1.46 \cdot 10^{-13}$
5 % of pyrene in $H_2O:C_{16}H_{10}$	$2.20 \cdot 10^{-15}$	$6.73 \cdot 10^{-14}$	$2.01 \cdot 10^{-13}$
1 % of pyrene in $H_2O:C_{16}H_{10}$	$3.61 \cdot 10^{-15}$	$9.01 \cdot 10^{-14}$	$7.59 \cdot 10^{-13}$

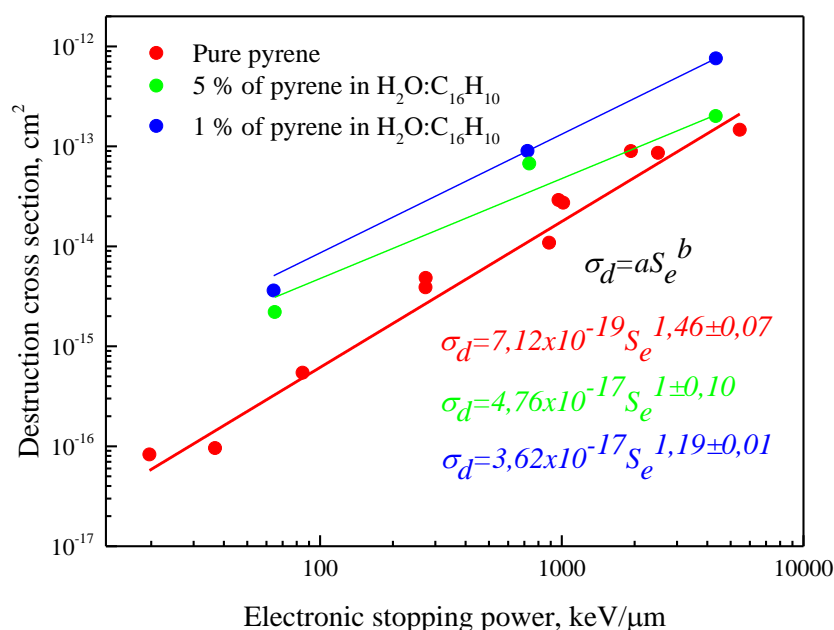


Figure 4.15. Fitting of the destruction cross section of pyrene as a function of the electronic stopping power of the projectile for pure pyrene and for 1 and 5 % of pyrene concentration in  $H_2O:C_{16}H_{10}$  mixtures.

This section presents the results about pyrene: $H_2O$  mixtures irradiation with three different ions at low temperature. The result was consistent with previous findings that the destruction cross section dramatically increases at low pyrene concentrations in the mixture. This is likely explained by an indirect effect, the radicals formed as a result of water irradiation attack pyrene molecules, which leads to the destruction of pyridine and formation of new species.

#### 4.4 New molecules formation

It is evident that irradiation of pyrene ( $C_{16}H_{10}$ ) can lead to the formation of molecules and ions containing either carbon (C), hydrogen (H), or both. Extensive research has been conducted to analyse the new species generated during hydrocarbon irradiation (De Barros, et al., 2011), (Dartois, et al., 2017), (Pino, et al., 2019). The most commonly observed compounds include acetylene ( $C_2H_2$ ), ethylene ( $C_2H_4$ ), methane ( $CH_4$ ), ethane ( $C_2H_6$ ), etc. In the case of

pyrene-water mixtures, in addition to hydrocarbons, some oxygen-bearing species could also be formed.

In this section, we will primarily discuss the new compounds that arise from the irradiation of pure pyrene (Figure 4.16). It is much easier to identify new molecules and estimate the column densities in case of pure pyrene compared to the pyrene-water mixture. For pyrene-water mixtures, column density calculations of new compounds are challenging, since new peaks are usually not intense and often overlap with water bands.

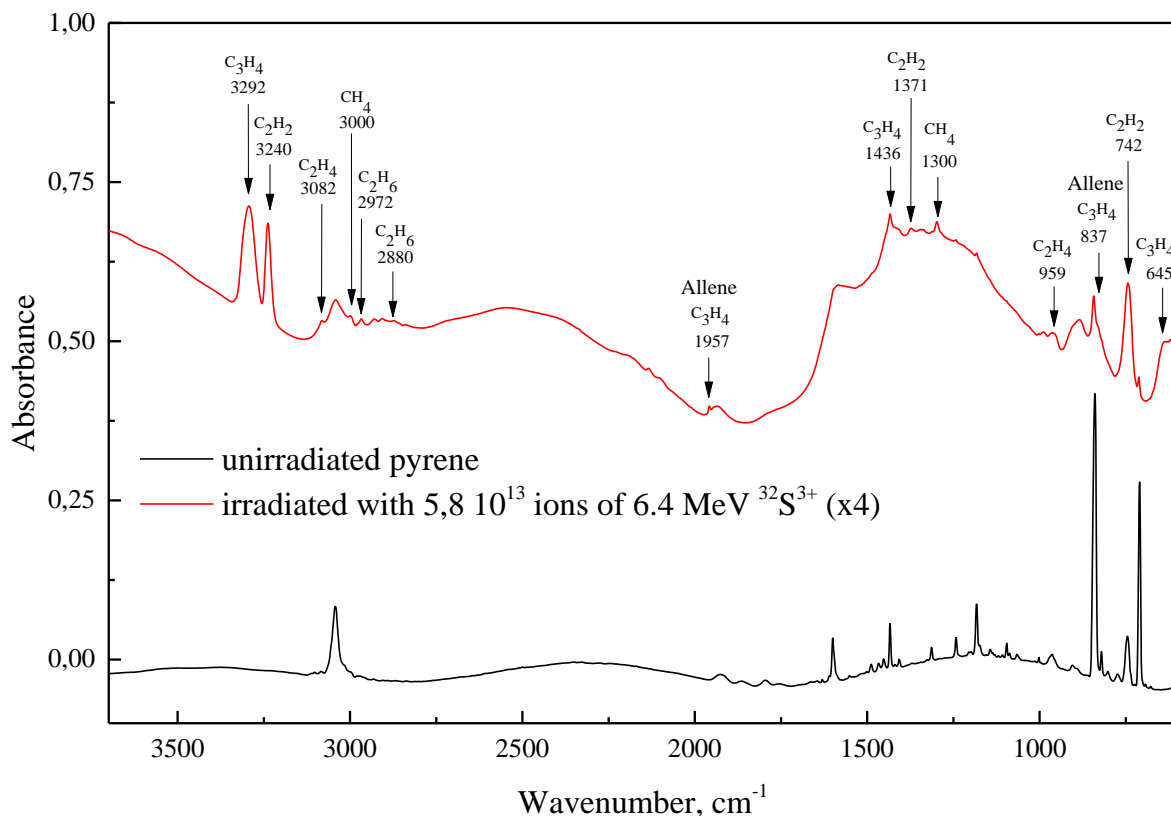


Figure 4.16. Infrared spectrum of pure pyrene before irradiation (black) and after irradiation with 6,4 MeV  $^{32}\text{S}^{3+}$  at fluence of  $5.8 \cdot 10^{13}$  (red) with newly identified peaks indicated.

IR spectroscopy has limitations for the identification of molecules present only in small quantities. This is particularly true for complex, large molecules, too. The more efficient techniques are high-resolution mass spectrometry, electrospray and laser ablation (Jones & Kaiser, 2013), (Henderson & Gudipati, 2015), (Ruf, et al., 2019). However, in the present study, infrared spectrometry was the only technique available for the in-situ analysis of the newly formed compounds. Therefore, for accurate identification, a sufficient quantity of new molecules is necessary, which was the case for thick samples, where at least half of the initial molecules were destroyed and contributed to formation of new molecular species.

Another problematic aspect is that data on the infrared spectra in the solid phase of molecules that could potentially form during irradiation in our experiments is limited. Infrared spectra with corresponding intensities are available for following hydrocarbons: methane ( $\text{CH}_4$ ), acetylene ( $\text{C}_2\text{H}_2$ ), ethylene ( $\text{C}_2\text{H}_4$ ), ethane ( $\text{C}_2\text{H}_6$ ), allene ( $\text{C}_3\text{H}_4$ ), benzene ( $\text{C}_6\text{H}_6$ ), cyclopropane ( $\text{c-C}_3\text{H}_6$ ), propane ( $\text{C}_3\text{H}_8$ ), propylene ( $\text{C}_3\text{H}_6$ ), propyne ( $\text{C}_3\text{H}_4$ ). Some of these molecules were identified in our samples with high probability.

Depending on the incoming ions, different bands are arising during pyrene irradiation. For example, new bands appear around 3292 (propyne) and 3240 (acetylene)  $\text{cm}^{-1}$  when pyrene is bombarded with heavy ions from C to Fe (Figure 4.3). However, these peaks are absent for H and He ions. Moreover, in the case of light ions (H and He), fewer new peaks are generally formed compared to heavy ions (C, S, Fe). Table 4.8 presents identified molecules and unidentified bands arising at irradiations with C, S and Fe ions.

Table 4.8. The biggest bands of identified molecules in experiments with pure pyrene, irradiated with C, S, Fe ions and the corresponding band strengths, extracted from the literature.

New molecules identified	Wavenumber, $\text{cm}^{-1}$	Avalue, $10^{-18}$ $\text{cm}/\text{molecule}$	New molecules identified	Wavenumber, $\text{cm}^{-1}$	Avalue, $10^{-18}$ $\text{cm}/\text{molecule}$
Acetylene $\text{C}_2\text{H}_2$	3240	23.9 <sup>a</sup>	Ethylene $\text{C}_2\text{H}_4$	3082	1.5 <sup>e</sup>
	1371	3.1 <sup>a</sup>		2974	1.0 <sup>e</sup>
	742	24.2 <sup>a</sup>		1434	2.3 <sup>e</sup>
Propyne $\text{C}_3\text{H}_4$	3292	17.7 <sup>b</sup>	Unidentified	959	12.6 <sup>e</sup>
	1436	2.87 <sup>b</sup>		2931	
	645	13.3 <sup>b</sup>		2906	
Methane $\text{CH}_4$	3000	14.1 <sup>c</sup>	2184		
	1300	10.4 <sup>c</sup>	2107		
Allene $\text{C}_3\text{H}_4$	1957	8.7 <sup>d</sup>	1935		
	837	16.4 <sup>d</sup>	1342		
Ethane $\text{C}_2\text{H}_6$	2972	20.0 <sup>e</sup>	988		
	2880	3.5 <sup>e</sup>	889		
	1462	3.3 <sup>e</sup>			

a – (Hudson, et al., 2014), b – (Hudson, et al., 2021), c – (Gerakines & Hudson, 2015), d – (Hudson & Yarnall, 2022), e – (Hudson, et al., 2014)

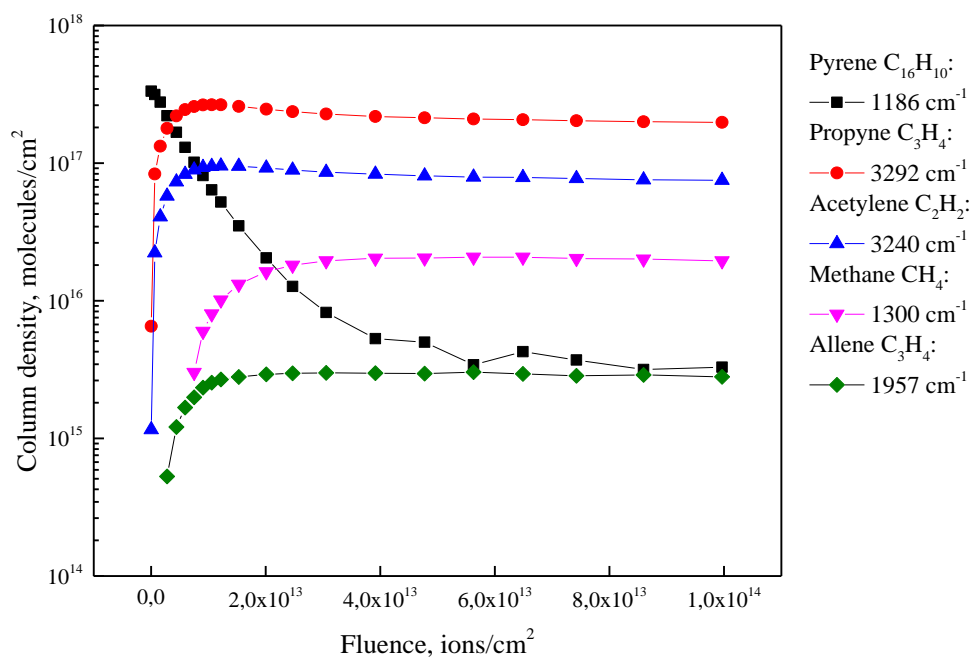


Figure 4.17. Column density evolution of pyrene, propyne, acetylene, methane and allene during irradiation with  $39.2 \text{ MeV } ^{56}\text{Fe}^{10+}$ .

It was possible to track the evolution of the intense peaks, attributed to molecules identified with high confidence. Figure 4.17 presents example of column density evolution of parent and daughter compounds for Fe projectile. As evident from the figure, the new molecules rapidly outnumber pyrene.

The formation cross section of new species was determined using eq. (3.5). Given that the only parent molecule in these experiments is pyrene,  $N_{<i>i,0</i>}$  represents the column density of pyrene at the beginning of irradiation. Table 4.9 presents the formation cross section of selected bands of new compounds alongside the destruction cross section of the initial pyrene. Therefore, the formation of propyne is the most probable, followed by acetylene, methane and allene for all projectiles. The alternations in column density before irradiation and at a local dose equal to 150 eV/molecule of parent and daughter molecules for various beams are presented in Table 4.10.

*Table 4.9. Formation cross section of new molecules for pure pyrene irradiations with different beams.*

		Wavenumber, cm <sup>-1</sup>	11,76 MeV <sup>12</sup> C <sup>4+</sup>	2 MeV <sup>12</sup> C <sup>2+</sup>	2,4 MeV <sup>12</sup> C <sup>2+</sup>	4 MeV <sup>32</sup> S <sup>2+</sup>	6,4 MeV <sup>32</sup> S <sup>3+</sup>	39,2 MeV <sup>56</sup> Fe <sup>10+</sup>
$\sigma_d, 10^{-15}$ cm <sup>2</sup>	Pyrene C <sub>16</sub> H <sub>10</sub>	Average (710, 850, 1186, 1435, 3051 cm <sup>-1</sup> )	78.8	9.26	25.1	23.7	80.8	140.0
	Acetylene C <sub>2</sub> H <sub>2</sub>	3240	0.13	2.01	4.27	13.73	44.77	55.29
$\sigma_f, 10^{-15}$ cm <sup>2</sup>	Propyne C <sub>3</sub> H <sub>4</sub>	3292	0.76	12.21	20.49	62.41	155.74	165.36
	Methane CH <sub>4</sub>	1300	-	-	0.19	1.11	1.53	0.71
	Allene C <sub>3</sub> H <sub>4</sub>	1957	-	-	0.06	0.71	0.71	1.02

*Table 4.10. Column density alternations ( $\Delta N, 10^{16}$  molecules/cm<sup>2</sup>) of new molecules for pure pyrene irradiations with different beams at deposited dose approximately equal to 150 eV/molecule.*

	Wavenumber, cm <sup>-1</sup>	11,76 MeV <sup>12</sup> C <sup>4+</sup>	2 MeV <sup>12</sup> C <sup>2+</sup>	2,4 MeV <sup>12</sup> C <sup>2+</sup>	4 MeV <sup>32</sup> S <sup>2+</sup>	6,4 MeV <sup>32</sup> S <sup>3+</sup>	39,2 MeV <sup>56</sup> Fe <sup>10+</sup>
Pyrene C <sub>16</sub> H <sub>10</sub>	1186	-15.21	-28.39	-25.13	-13.44	-36.39	-26.89
Acetylene C <sub>2</sub> H <sub>2</sub>	3240	0.44	1.85	2.78	1.83	8.59	9.47
	1371	-	-	1.75	0.57	1.49	1.34
	742	-	-	-	2.85	10.57	10.09
Propyne C <sub>3</sub> H <sub>4</sub>	3292	2.56	8.22	11.93	5.68	28.59	26.57
	645	-	-	5.22	2.90	21.20	15.70
Methane CH <sub>4</sub>	3000	-	-	-	0.05	0.19	0.45
	1300	-	-	0.33	0.23	0.81	0.80
Allene C <sub>3</sub> H <sub>4</sub>	1957	-	-	0.05	0.09	0.27	0.25
Ethane C <sub>2</sub> H <sub>6</sub>	2972	-	-	0.41	1.61	5.88	0.39
	2880	-	-	2.25	-	1.05	0.41
Ethylene C <sub>2</sub> H <sub>4</sub>	3082	-	-	0.61	0.52	1.22	2.04
	959	-	-	1.42	0.66	2.37	2.41

The appearance of peaks at the following wavenumbers were observed during irradiation with the light H and He projectiles: 656, 683, 725, 756, 812, 831, 880, 1013, 1197, 1505, 1550, 2125, 2800, 2834, 2869 and 2930  $\text{cm}^{-1}$ . However, no clear assignment and identification of new molecules was possible with a high probability and confidence, because the bands are too weak.

The new molecules appearing after irradiation of pyrene-water mixtures resemble the ones appearing from pure pyridine irradiations; however, new compounds containing oxygen also appear. In the case of pyrene-water mixtures, the following peaks were identified: 3283 ( $\text{C}_3\text{H}_4$ ), 3235 ( $\text{C}_2\text{H}_2$ ), 2339 ( $\text{CO}_2$ ), 2139 ( $\text{CO}$ ), 2278 ( $^{13}\text{CO}_2$ ), 2154 ( $\text{C}_5\text{O}$ ), 2091 ( $^{13}\text{CO}$ ) and 659 ( $\text{CO}_2$ )  $\text{cm}^{-1}$ . There are also unidentified peaks: 2930, 2261, 2239, 2171, 755 and 727  $\text{cm}^{-1}$ .

## References

- Allamandola, L. J., Tielens, A. G. G. M. & Barker, J. R., 1989. Interstellar polycyclic aromatic hydrocarbons-The infrared emission bands, the excitation/emission mechanism, and the astrophysical implications. *Astrophysical Journal Supplement Series (ISSN 0067-0049)*, pp. 733-775.
- Balanzat, E., Betz, N. & Bouffard, S., 1995. Swift heavy ion modification of polymers. Nuclear Instruments and Methods. *Physics Research Section B: Beam Interactions with Materials and Atoms*, 105(1-4), pp. 46-54.
- Basile, B. P., Middleditch, B. S. & Oró, J., 1984. Polycyclic aromatic hydrocarbons in the Murchison meteorite. *Organic Geochemistry*, 5(4), pp. 211-216.
- Bibang, P. A., 2021. *Molécules organiques complexes sous irradiation: effets de la matrice et de la température*. Caen: Normandie Université.
- Bouwman, J. et al., 2010. Photochemistry of the PAH pyrene in water ice: the case for ion-mediated solid-state astrochemistry. *Astronomy & Astrophysics*, Volume 511, p. A33.
- Bouwman, J., Mattioda, A. L., Linnartz, H. & Allamandola, L. J., 2011. Photochemistry of Polycyclic Aromatic hydrocarbons in cosmic water ice-I. Mid-IR Spectroscopy and Photoproducts. *Astronomy & Astrophysics*, Volume 525, p. A93.
- Bouwman, J. et al., 2009. Real-time optical spectroscopy of vacuum ultraviolet irradiated pyrene: H<sub>2</sub>O interstellar ice. *The Astrophysical Journal*, 700(1), p. 56.
- Califano, S. & Abbondanza, G., 1963. Infrared Spectra in Polarized Light and Vibrational Assignment of the Infrared-Active Modes of Pyrene and Pyrene-d 10. *The Journal of Chemical Physics*, pp. 1016-1023.
- Clairemidi, J., Bréchnignac, P., Moreels, G. & Pautet, D., 2004. Tentative identification of pyrene as a polycyclic aromatic molecule in UV spectra of comet P/Halley: An emission from 368 to 384nm. *Planetary and Space Science*, 52(8), pp. 761-772.
- COOK, A. M. et al., 2015. Photochemistry of polycyclic aromatic hydrocarbons in cosmic water ice: The role of PAH ionization and concentration. *The Astrophysical Journal*, 799(1), p. 14.
- Cuylle, S. H., Allamandola, L. J. & Linnartz, H., 2014. Photochemistry of PAHs in cosmic water ice-The effect of concentration on UV-VIS spectroscopy and ionization efficiency. *Astronomy & Astrophysics*, Volume 562, p. A22.
- Cuylle, S. H. et al., 2012. Ly $\alpha$ -induced charge effects of polycyclic aromatic hydrocarbons embedded in ammonia and ammonia: water ice. *Monthly Notices of the Royal Astronomical Society*, 423(2), pp. 1825-1830.
- da Costa, C. A. D. et al., 2020. Valine radiolysis by H<sup>+</sup>, He<sup>+</sup>, N<sup>+</sup>, and S<sup>15+</sup> MeV ions. *International journal of molecular sciences*, p. 1893.
- Dartois, E. et al., 2017. Swift heavy ion irradiation of interstellar dust analogues-Small carbonaceous species released by cosmic rays. *Astronomy & Astrophysics*, Volume 599, p. A130.

- Dartois, E. et al., 2013. Swift heavy ion irradiation of water ice from MeV to GeV energies- Approaching true cosmic ray compaction. *Astronomy & Astrophysics*, Volume 557, p. A97.
- De Barros, A. L. F. et al., 2011. Cosmic ray impact on astrophysical ices: laboratory studies on heavy ion irradiation of methane. *Astronomy & Astrophysics*, Volume 531, p. A160.
- Djomgoue, P. & Njopwouo, D., 2013. FT-IR spectroscopy applied for surface clays characterization. *Journal of Surface Engineered Materials and Advanced Technology*, p. 275.
- Elsila, J. E., de Leon, N. P., Buseck, P. R. & Zare, R. N., 2005. Alkylation of polycyclic aromatic hydrocarbons in carbonaceous chondrites. *Geochimica et Cosmochimica Acta*, 69(5), pp. 1349-1357.
- Geiger, C. A. & Rossman, G. R., 2018. IR spectroscopy and OH<sup>-</sup> in silicate garnet: The long quest to document the hydrogarnet substitution. *American Mineralogist*, pp. 384-393.
- Gerakines, P. A. & Hudson, R. L., 2015. Infrared spectra and optical constants of elusive amorphous methane. *The Astrophysical Journal Letters*, p. L20.
- Gibb, E. L., Whittet, D. C. B., Boogert, A. C. A. & Tielens, A. G. G., 2004. Interstellar ice: the infrared space observatory legacy. *The astrophysical journal supplement series*, p. 35.
- Gudipati, M. S. & Allamandola, L. J., 2004. Polycyclic aromatic hydrocarbon ionization energy lowering in water ices. *The Astrophysical Journal*, 615(2), p. L177.
- Hardegree-Ullman, E. E. et al., 2014. Laboratory determination of the infrared band strengths of pyrene frozen in water ice: Implications for the composition of interstellar ices. *The Astrophysical Journal*, p. 172.
- Henderson, B. L. & Gudipati, M. S., 2015. Direct detection of complex organic products in ultraviolet (Ly $\alpha$ ) and electron-irradiated astrophysical and cometary ice analogs using two-step laser ablation and ionization mass spectrometry. *The Astrophysical Journal*, 800(1), p. 66.
- Herczku, P. et al., 2021. The Ice Chamber for Astrophysics–Astrochemistry (ICA): A new experimental facility for ion impact studies of astrophysical ice analogs. *Review of Scientific Instruments*, 92(8).
- Hudson, R. L., Ferrante, R. F. & Moore, M. H., 2014. Infrared spectra and optical constants of astronomical ices: I. Amorphous and crystalline acetylene. *Icarus*, pp. 276-287.
- Hudson, R. L., Gerakines, P. A. & Moore, M. H., 2014. Infrared spectra and optical constants of astronomical ices: II. Ethane and ethylene. *Icarus*, Volume 243, pp. 148-157.
- Hudson, R. L., Gerakines, P. A., Yarnall, Y. Y. & Coones, R. T., 2021. Infrared spectra and optical constants of astronomical ices: III. Propane, propylene, and propyne. *Icarus*, p. 114033.
- Hudson, R. L. & Yarnall, Y. Y., 2022. Infrared Spectra and Intensities of Amorphous and Crystalline Allene. *ACS Earth and Space Chemistry*, pp. 1163-1170.
- Jones, B. M. & Kaiser, R. I., 2013. Application of reflectron time-of-flight mass spectrometry in the analysis of astrophysically relevant ices exposed to ionization radiation: Methane (CH<sub>4</sub>) and D<sub>4</sub>-methane (CD<sub>4</sub>) as a case study. *The Journal of Physical Chemistry Letters*, 4(11), pp. 1965-1971.

- Krasheninnikov, A. V. & Nordlund, K., 2010. Ion and electron irradiation-induced effects in nanostructured materials. *Journal of applied physics*, 107(7).
- Marciniak, A. et al., 2021. Photodissociation of aliphatic PAH derivatives under relevant astrophysical conditions. *Astronomy & Astrophysics*, Volume 652, p. A42.
- Materese, C. K., Gerakines, P. A. & Hudson, R. L., 2020. The radiation stability of thymine in solid H<sub>2</sub>O. *Astrobiology*, 20(8), pp. 956-963.
- Mejía, C. et al., 2015. Compaction of porous ices rich in water by swift heavy ions. *Icarus*, pp. 222-229.
- Mejía, C. et al., 2020. Radiolysis of Ices by Cosmic-Rays: CH<sub>4</sub> and H<sub>2</sub>O Ices Mixtures Irradiated by 40 MeV <sup>58</sup>Ni<sup>11+</sup> Ions. *The Astrophysical Journal*, 894(2), p. 132.
- Muniz, G., 2017. *Irradiation of aromatic heterocyclic molecules at low temperature: a link to astrochemistry*. s.l.:PhD thesis.
- Noble, J. A., Michoulier, E., Aupetit, C. & Mascetti, J., 2020. Influence of ice structure on the soft UV photochemistry of PAHs embedded in solid water. *Astronomy & Astrophysics*, Volume 644, p. A22.
- Öberg, K. I., Van Dishoeck, E. F., Linnartz, H. & Andersson, S., 2010. The effect of H<sub>2</sub>O on ice photochemistry. *The Astrophysical Journal*, 718(2), p. 832.
- Pino, T. et al., 2019. Release of large polycyclic aromatic hydrocarbons and fullerenes by cosmic rays from interstellar dust-Swift heavy ion irradiations of interstellar carbonaceous dust analogue. *Astronomy & Astrophysics*, Volume 623, p. A134.
- Portugal, W. et al., 2014. Radiolysis of amino acids by heavy and energetic cosmic ray analogues in simulated space environments:  $\alpha$ -glycine zwitterion form. *Monthly Notices of the Royal Astronomical Society*, 441(4), pp. 3209-3225.
- Powell, C. F., Fowler, P. H. & Perkins, D. H., 1959. *The study of elementary particles by the photographic method: An account of the principal techniques and discoveries illustrated by an atlas of photomicrographs*. s.l.:s.n.
- Ruf, A. et al., 2019. Organosulfur compounds formed by sulfur ion bombardment of astrophysical ice analogs: implications for moons, comets, and Kuiper Belt objects. *The Astrophysical journal letters*, 885(2), p. L40.
- Ten Brinck, S. et al., 2022. Polycyclic Aromatic Hydrocarbons (PAHs) in Interstellar Ices: A Computational Study into How the Ice Matrix Influences the Ionic State of PAH Photoproducts. *ACS Earth and Space Chemistry*, 6(3), pp. 766-774.
- Vignoli Muniz, G. S. et al., 2017. Radioresistance of adenine to cosmic rays. *Astrobiology*, 4(298-308), p. 17.
- Woon, D. E. & Park, J. Y., 2004. Photoionization of benzene and small polycyclic aromatic hydrocarbons in ultraviolet-processed astrophysical ices: A computational study. *The Astrophysical Journal*, 607(1), p. 342.
- Zhao, L. et al., 2018. Pyrene synthesis in circumstellar envelopes and its role in the formation of 2D nanostructures. *Nature Astronomy*, 2(5), pp. 413-419.



Ziegler, J. F., Ziegler, M. D. & Biersack, J. P., 2010. SRIM—The stopping and range of ions in matter. *Nuclear Instruments and Methods in Physics Research Section B: Beam Interactions with Materials and Atoms*, pp. 1818-1823.

## 5. Radioresistance of aromatic molecules: size effect

As emphasized before, PAH molecules are widespread in space. Thus, the question of their survivability is crucial. Polycyclic structures are more stable than aliphatic ones because they are bound by a delocalized electron cloud shared by several atoms. It has long been known that the most common PAH molecules in space contain 50-100 carbon atoms (Allamandola, et al., 1989), as they are more resistant to ionizing radiation than smaller ones. The reason for this is that, when exposed to ionizing radiation, large molecules tend to wobble, which helps to dissipate the energy, whereas for smaller molecules fragmentation is more efficient.

Several studies dedicated to investigation of the stability of different PAH structures exposed to photon irradiation confirm that the stability of PAHs is directly dependent on the molecule size. Although, most of the studies on this topic come from environmental sciences, as PAHs are omnipresent as dangerous pollutant produced from petrol combustion. For example, in the work (Cataldo & Keheyran, 2006), a liquid mixture of different PAHs dissolved in acetonitrile was exposed to gamma-irradiation. They found that the radiation chemical yield (number of destroyed molecules per 100 eV deposited dose) decreasing with increasing size of molecule (with a few exceptions). A similar dependence was observed in the study by (Nadal, et al., 2006), where PAHs, dissolved in a tetradecane solution, were exposed to UV irradiation.

In the present study, we present preliminary results comparing the radioresistance of different cyclic molecules under ion irradiation: pyrene, phenanthrene, naphthalene, indene and adamantane (Figure 5.1). These molecules were chosen because they have different numbers of carbon cycles, different number of carbons per ring (five- and six-membered) and different structures. Naphthalene, phenanthrene and pyrene consist of two, three and four fused hexagonal rings, respectively. Indene consist of fused hexa- and pentagonal rings. Adamantane is a diamondoid and it consists of four fused hexagonal rings, which form a cage structure. In Figure 5.1 catacondensed molecules (carbon atoms has maximum two rings in common) presented in the upper row and pericondensed (at least one carbon atom has three rings in common) in the lower row (Holm, et al., 2011).

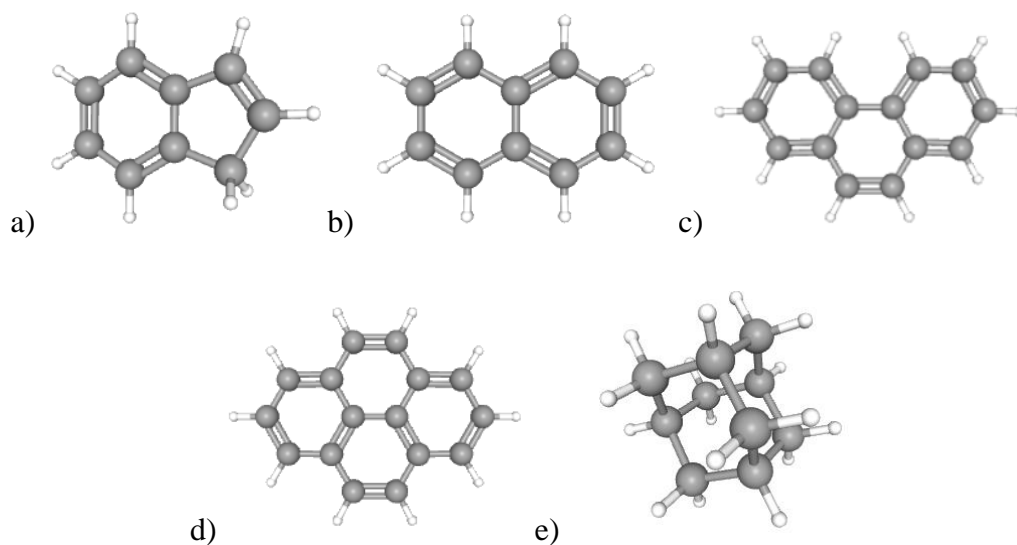


Figure 5.1. Schematic representation of a) indene  $C_9H_8$ , b) naphthalene  $C_{10}H_8$ , c) phenanthrene  $C_{14}H_{10}$ , d) pyrene  $C_{16}H_{10}$  and e) adamantane  $C_{10}H_{16}$ .

As noted in Chapter 1, indene has recently been detected in the molecular cloud TMC-1 through its rotational spectrum at radio frequencies (Burkhardt, et al., 2021), (Cernicharo, et al., 2021). Soon after, infrared studies on indene (Maté, et al., 2023), including UV and electron irradiation (Maté, et al., 2024) emerged. High symmetry and lack of permanent dipole moment makes naphthalene, phenanthrene and pyrene difficult to detect through radio observations. However, mentioned PAHs were commonly detected in meteorites (Elsila, et al., 2005), (Basile, et al., 1984) and they are believed to be widespread in space. In addition, naphthalene derivatives were recently detected in TMC-1 (McGuire, et al., 2021). Diamonoids, including adamantane, are also believed to be present in space, although they are supposed to be less abundant than PAHs (Pirali, et al., 2007).

## 5.1 Sample preparations

Pyrene, phenanthrene, naphthalene, indene and adamantane were irradiated with 39.2 MeV  $^{56}\text{Fe}^{10+}$  at the IGLIAS setup at the IRRSUD beamline of the GANIL facility. Indene is liquid at room temperature, so the deposition of the sample was similar to pyridine (Section 3.1). All other molecules are solid at room temperature and the oven was used for sample preparations (Section 2.3.2.1). Samples characteristics as well as stopping powers, calculated with the SRIM software (Ziegler, et al., 2010) are presented in Table 5.1. Table 5.2 also presents assignments and band strengths of infrared bands that were used for column density calculations shown in Table 5.1 and in further analysis.

*Table 5.1. Characteristics of the samples of aromatic molecules that were irradiated with 39.2 MeV  $^{56}\text{Fe}^{10+}$  at GANIL facility.*

	Chemical formula	Molecular weight, g/mol	Density, g/cm <sup>3</sup> (Sherry, 2024)	Initial thickness of the sample, $\mu\text{m}$	Column density, 10 <sup>16</sup> molecules/cm <sup>2</sup>	Electronic stopping power, keV/ $\mu\text{m}$	Nuclear stopping power, keV/ $\mu\text{m}$	Projected range, $\mu\text{m}$
Indene	C <sub>9</sub> H <sub>8</sub>	116.16	0.997	0.25	12.7	4714	14.1	14.2
Naphthalene	C <sub>10</sub> H <sub>8</sub>	128.17	1.14	0.11	6.1	5071	15.3	13.0
Phenanthrene	C <sub>14</sub> H <sub>10</sub>	178.23	1.025	0.47	16.1	4481	13.5	14.7
Pyrene	C <sub>16</sub> H <sub>10</sub>	202.25	1.27	0.95	35.7	5449	16.5	12.0
Adamantane	C <sub>10</sub> H <sub>16</sub>	136.24	1.08	0.11	5.3	5476	16.2	12.5

Table 5.2. Assignments and strengths of infrared bands of aromatic molecules used in the analysis.

	Wavenumber, $\text{cm}^{-1}$	Vibration assignment	Integrated range	Avalue, $10^{-19}$ cm/molecule
Indene	720	C-H hexa-ring out-of-plane bending <sup>f</sup>	740–711	60 <sup>f</sup>
	768	C-H out-of-plane bending <sup>f</sup>	793–755	200 <sup>f</sup>
	1313	C-H penta-ring in-plane bending <sup>f</sup>	1321–1302	14 <sup>f</sup>
	1390	CH <sub>2</sub> bending <sup>f</sup>	1419–1374	51 <sup>f</sup>
	1459	C-H hexa-ring in-plane bending <sup>f</sup>	1487–1443	64 <sup>f</sup>
	3100	C-H hexa- and penta- rings asymmetric stretch <sup>f</sup>	3153–2983	136 <sup>f</sup>
Naphthalene	783	C-H-wagging <sup>e</sup>	805-757	120 <sup>d</sup>
	1390	C-H-bending, C-C stretch <sup>e</sup>	1403-1372	8.1 <sup>d</sup>
	1508	C=C stretch <sup>e</sup>	1530-1497	11.5 <sup>d</sup>
	3049	C-H stretch <sup>e</sup>	3085-2994	50 <sup>d</sup>
Phenanthrene	817	C-H out-of-plane bending <sup>b</sup>	855-800	99.17 <sup>b</sup>
	1250	C-H in-plane bending <sup>b</sup>	1262-1228	15.61 <sup>b</sup>
	1500	C-C stretch <sup>b</sup>	1508-1492	11.79 <sup>b</sup>
	3058	C-H stretch		
Pyrene	714	C-H deformation <sup>a</sup>	722-700	140.73 <sup>a</sup>
	850	ring deformation <sup>a</sup>	864-837	191.25 <sup>a</sup>
	1186	ring deformation <sup>a</sup>	1194-1171	34.24 <sup>a</sup>
	1435	ring stretch <sup>a</sup>	1441-1426	28.28 <sup>a</sup>
	3051	C-H stretch <sup>a</sup>	3078-3032	60.36 <sup>a</sup>
Adamantane	1101	CH <sub>2</sub> twist <sup>g</sup>	1124-1090	4.98 <sup>g</sup>
	1450	CH <sub>2</sub> scissor <sup>g</sup>	1464-1433	18.3 <sup>g</sup>
	2850		2872-2837	94.7 <sup>h</sup>
	2906	C-H stretch <sup>g</sup>	3205-2870	1205 <sup>h</sup>

*a* – (Hardegree-Ullman, et al., 2014), *b* – (Hudgins, et al., 1994), *c* – (Hudgins & Sandford, 1998), *d* – (Sandford, et al., 2004), *e* – (Srivastava & Singh, 2017), *f* – (Maté, et al., 2023), *g* – (Jensen, 2004), *h* – (Patzer, et al., 2012)

## 5.2 Results

In Figure 5.2, the IR spectra of the investigated molecules before and after irradiation at a deposited dose of 60 eV/molecule are presented. As the initial thickness of the samples varies significantly (Table 5.1), some samples have been completely destroyed at this dose, while for others half of the initial molecules still remained. Additionally, in many cases, the appearance of new molecules is noticeable. In particular, features near 3292 and 3240  $\text{cm}^{-1}$  which, as discussed previously, belong to propyne ( $\text{C}_3\text{H}_4$ ) and acetylene ( $\text{C}_2\text{H}_2$ ), respectively, appear for all PAH molecules. In contrast, they are not observed in the case of adamantane; this issue remains unclear for us.

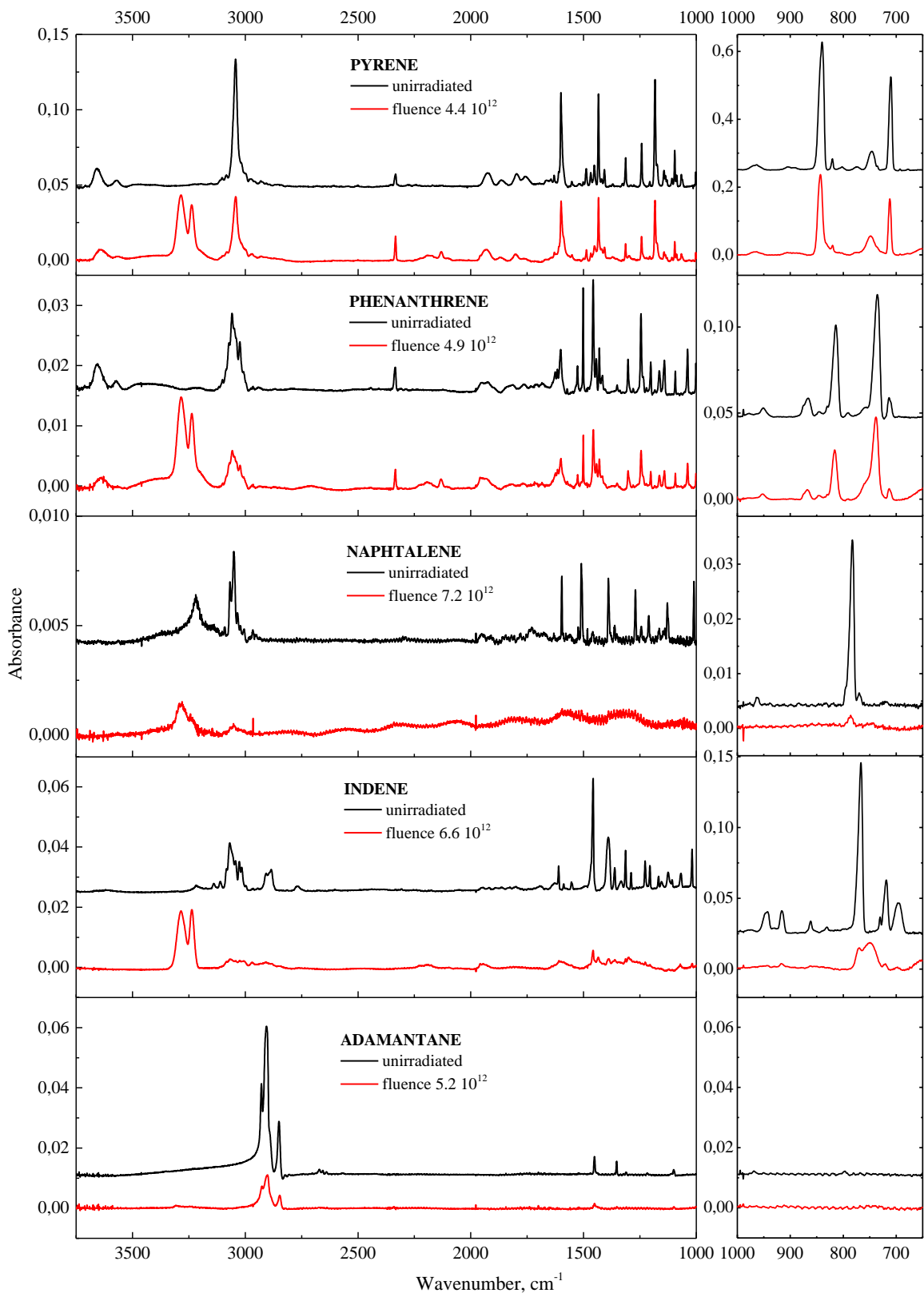


Figure 5.2. Infrared spectra of unirradiated (top-bottom) pyrene, phenanthrene, naphthalene, indene and adamantane – black line, and irradiated with 39.2 MeV  $^{56}\text{Fe}^{10+}$  with deposited local dose around 60 eV/molecule – red line. The fluences are (from top to bottom)  $4.4 \cdot 10^{12}$ ;  $4.9 \cdot 10^{12}$ ;  $7.2 \cdot 10^{12}$ ;  $6.6 \cdot 10^{12}$ ;  $5.2 \cdot 10^{12}$  ions/cm<sup>2</sup>.

The destruction cross section was calculated for bands, specified in Table 5.2, using eq. (4.1). The results are presented in Table 5.3. The strong correlation between the average destruction cross section and the molecular weight is noticeable. The least radioresistant molecule is indene. The destruction cross section of the latter is three times higher than that of pyrene. In order to compare our results on ion irradiation with data from the literature on photon irradiation, we calculated the chemical yield (Vignoli Muniz, et al., 2017), which indicates the number of destroyed molecules per 100 eV deposited dose:

$$G = \frac{100 [eV] * \sigma_d [cm^2]}{S_e + S_n [eV cm^2 molecule^{-1}]}. \quad \text{eq. (5.1)}$$

The stopping powers were calculated with the SRIM software (Ziegler, et al., 2010) in units of eV/(1e15 atoms/cm<sup>2</sup>) and were then multiplied by the number of atoms in each molecule.

Table 5.3. Destruction cross section of PAHs.

	Molecular weight, g/mol	Wavenumber, cm <sup>-1</sup>	Destruction cross section, 10 <sup>-13</sup> cm <sup>2</sup>	Average destruction cross section ± SD, 10 <sup>-13</sup> cm <sup>2</sup>	Chemical yield G, molecules
Indene	116.16	720	4.65	4.01±0.82	5.13
		768	4.49		
		1313	4.38		
		1390	4.44		
		1459	3.55		
		3100	2.53		
Naphthalene	128.17	783	4.03	3.43±0.49	3.60
		1390	2.87		
		1508	3.59		
		3049	3.21		
Phenanthrene	178.23	817	1.50	1.63±0.36	1.25
		1250	1.83		
		1500	1.99		
		3058	1.19		
Pyrene	202.25	714	1.59	1.40±0.18	0.97
		850	1.31		
		1186	1.57		
		1435	1.37		
		3051	1.16		
Adamantane	136.24	1101	1.93	2.24±0.51	1.93
		1450	1.68		
		2850	2.56		
		2906	2.77		

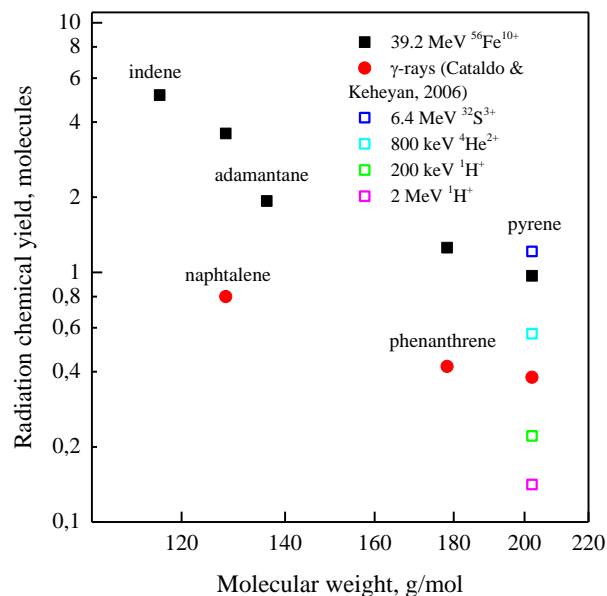


Figure 5.3. Radiation chemical yields for cyclic molecules irradiated with ions and  $\gamma$ -rays (Cataldo & Keheyan, 2006) as a function of their molecular weight.

Figure 5.3 presents the radiation chemical yield of PAHs, irradiated with heavy ions as reported in this chapter and in Chapter 4, along with results on  $\gamma$ -rays irradiation, obtained by (Cataldo & Keheyan, 2006). The number of destroyed molecules is greater for Fe than for  $\gamma$ -rays, which seems reasonable due to the lower ionization capability of  $\gamma$ -rays. Additionally, it is noticeable that for protons, this value is even lower than for  $\gamma$ -rays. In general, our results confirm the trend, that radioresistance of the molecule increases with molecular weight (Montillaud, et al., 2013).

Regarding the stability difference between catacondensed and pericondensed structures, it has been reported in a theoretical study (Holm, et al., 2011) that fragmentation yields in ion-PAH collisions in the gas phase are significantly smaller for pericondensed structures. This suggests that catacondensed molecules are more stable.

Additionally, the question of isomer stability arises. (Cataldo & Keheyan, 2006) found that chemical yield for pyrene (0.38) is slightly smaller than for fluoranthene (0.42). The study of (Delaunay, et al., 2018) compared the yields of newly formed compounds during ion irradiation of fluoranthene and pyrene clusters. They found that the yield for fluoranthene is 2.5 times higher than that for pyrene clusters.

As mentioned earlier, large PAH (more than 50 carbon atoms) are more representative of conditions in the interstellar medium. However, conducting experiments with them is more challenging. Nevertheless, for a better understanding of the evolution of PAHs in space, it is crucial to conduct experiments on the irradiation of large PAHs trapped in a water matrix in the solid phase.

## References

- Allamandola, L. J., Tielens, A. G. G. M. & Barker, J. R., 1989. Interstellar polycyclic aromatic hydrocarbons-The infrared emission bands, the excitation/emission mechanism, and the astrophysical implications. *Astrophysical Journal Supplement Series (ISSN 0067-0049)*, pp. 733-775.
- Basile, B. P., Middleditch, B. S. & Oró, J., 1984. Polycyclic aromatic hydrocarbons in the Murchison meteorite. *Organic Geochemistry*, 5(4), pp. 211-216.
- Burkhardt, A. M. et al., 2021. Discovery of the pure polycyclic aromatic hydrocarbon indene (c-C<sub>9</sub>H<sub>8</sub>) with GOTHAM observations of TMC-1. *The Astrophysical Journal Letters*, 913(2), p. L18.
- Cataldo, F. & Keheyan, Y., 2006. Gamma-radiolysis and ozonolysis of polycyclic aromatic hydrocarbons (PAHs) in solution. *Journal of radioanalytical and nuclear chemistry*, 267(3), pp. 679-683.
- Cernicharo, J. et al., 2021. Pure hydrocarbon cycles in TMC-1: Discovery of ethynyl cyclopropenylidene, cyclopentadiene, and indene. *Astronomy & Astrophysics*, Volume 649, p. L15.
- Delaunay, R. et al., 2018. Ion-collision induced molecular growth in polycyclic aromatic hydrocarbon clusters: comparison of C<sub>16</sub>H<sub>10</sub> structural isomers. *The European Physical Journal D*, Volume 72, pp. 1-7.
- Elsila, J. E., de Leon, N. P., Buseck, P. R. & Zare, R. N., 2005. Alkylation of polycyclic aromatic hydrocarbons in carbonaceous chondrites. *Geochimica et Cosmochimica Acta*, 69(5), pp. 1349-1357.
- Hardegree-Ullman, E. E. et al., 2014. Laboratory determination of the infrared band strengths of pyrene frozen in water ice: Implications for the composition of interstellar ices. *The Astrophysical Journal*, p. 172.
- Holm, A. I., Johansson, H. A., Cederquist, H. & Zettergren, H., 2011. Dissociation and multiple ionization energies for five polycyclic aromatic hydrocarbon molecules. *The Journal of chemical physics*, 134(4).
- Hudgins, D. M. & Sandford, S. A., 1998. Infrared spectroscopy of matrix isolated polycyclic aromatic hydrocarbons. 1. PAHs containing two to four ring. *The Journal of Physical Chemistry A*, pp. 329-343.
- Hudgins, D. M., Sandford, S. A. & Allamandola, L. J., 1994. Infrared spectroscopy of polycyclic aromatic hydrocarbon cations. 1. Matrix-isolated naphthalene and perdeuterated naphthalene. *The Journal of physical chemistry*, pp. 4243-4253.
- Jensen, J. O., 2004. Vibrational frequencies and structural determination of adamantane. *Spectrochimica Acta Part A: Molecular and Biomolecular Spectroscopy*, pp. 1895-1905.
- Maté, B. et al., 2024. Indene energetic processing in ice mantles in the interstellar medium. *Astronomy & Astrophysics*, Volume 682, p. A158.



- Maté, B. et al., 2023. Infrared spectra of solid indene pure and in water ice: implications for observed IR absorptions in TMC-1.. *Monthly Notices of the Royal Astronomical Society*, pp. 5887-5898.
- McGuire, B. A. et al., 2021. Detection of two interstellar polycyclic aromatic hydrocarbons via spectral matched filtering. *Science*, 371(6535), pp. 1265-1269.
- Montillaud, J., Joblin, C. & Toubanc, D., 2013. Evolution of polycyclic aromatic hydrocarbons in photodissociation regions-Hydrogenation and charge states. *Astronomy & Astrophysics*, Volume 552, p. A15.
- Nadal, M. et al., 2006. Influence of UV-B radiation and temperature on photodegradation of PAHs: preliminary results. *Journal of Atmospheric Chemistry*, Volume 55, pp. 241-252.
- Patzer, A., Schütz, M., Möller, T. & Dopfer, O., 2012. Infrared spectrum and structure of the adamantane cation: direct evidence for Jahn-Teller distortion. *Angewandte Chemie*, pp. 4925-4929.
- Pirali, O. et al., 2007. Infrared spectroscopy of diamondoid molecules: New insights into the presence of nanodiamonds in the interstellar medium. *The Astrophysical Journal*, 661(2), p. 919.
- Sandford, S. A., Bernstein, M. P. & Allamandola, L. J., 2004. The mid-infrared laboratory spectra of naphthalene (C<sub>10</sub>H<sub>8</sub>) in solid H<sub>2</sub>O. *The Astrophysical Journal*, p. 346.
- Sherry, S., 2024. *National library of medicine*. [Online] Available at: <https://www.ncbi.nlm.nih.gov/> [Accessed 24 06 2024].
- Srivastava, A. & Singh, V. B., 2017. Theoretical and experimental studies of vibrational spectra of naphthalene and its cation. *Indian journal of pure and applied physics*, p. Theoretical and experimental studies of vibrational spectra of naphthalene and its cation..
- Tielens, 2008. Interstellar polycyclic aromatic hydrocarbon molecules. *Annu. Rev. Astron. Astrophys.*, pp. 289-337.
- Vignoli Muniz, G. S. et al., 2017. Radioresistance of adenine to cosmic rays. *Astrobiology*, 17(4), pp. 298-308.
- Ziegler, J. F., Ziegler, M. D. & Biersack, J. P., 2010. SRIM—The stopping and range of ions in matter. *Nuclear Instruments and Methods in Physics Research Section B: Beam Interactions with Materials and Atoms*, pp. 1818-1823.

## 6. Astrophysical implications

Cyclic molecules play an essential role in biochemical processes of terrestrial organisms and serve as main carbon carriers, significantly influencing the carbon cycle in the cosmos. Different cyclic molecules, including PAHs have already been detected in molecular clouds (Burkhardt, et al., 2021), (Cernicharo, et al., 2021), (McGuire, et al., 2021). Icy mantles, formed in dense clouds, are promising sites for the formation of cyclic molecules. Dense clouds, with a relatively high density of  $10^3$ - $10^7$  particles per cubic centimeter, effectively shield the icy mantles from UV photons. Most photons do not penetrate the dense cloud from outside; however, small amounts of photons are generated as a result of interactions between ions and the material within the dense cloud. The average lifetime of a molecular cloud is  $\sim$  a few tens million years (Chevance, et al., 2020), (Meidt, et al., 2015). As the dense clouds evolve, they transform into accretion discs, eventually leading to the formation of stellar system (Figure 6.1). Therefore, studying the survivability of cyclic molecules is crucial for understanding the evolution of carbon matter.

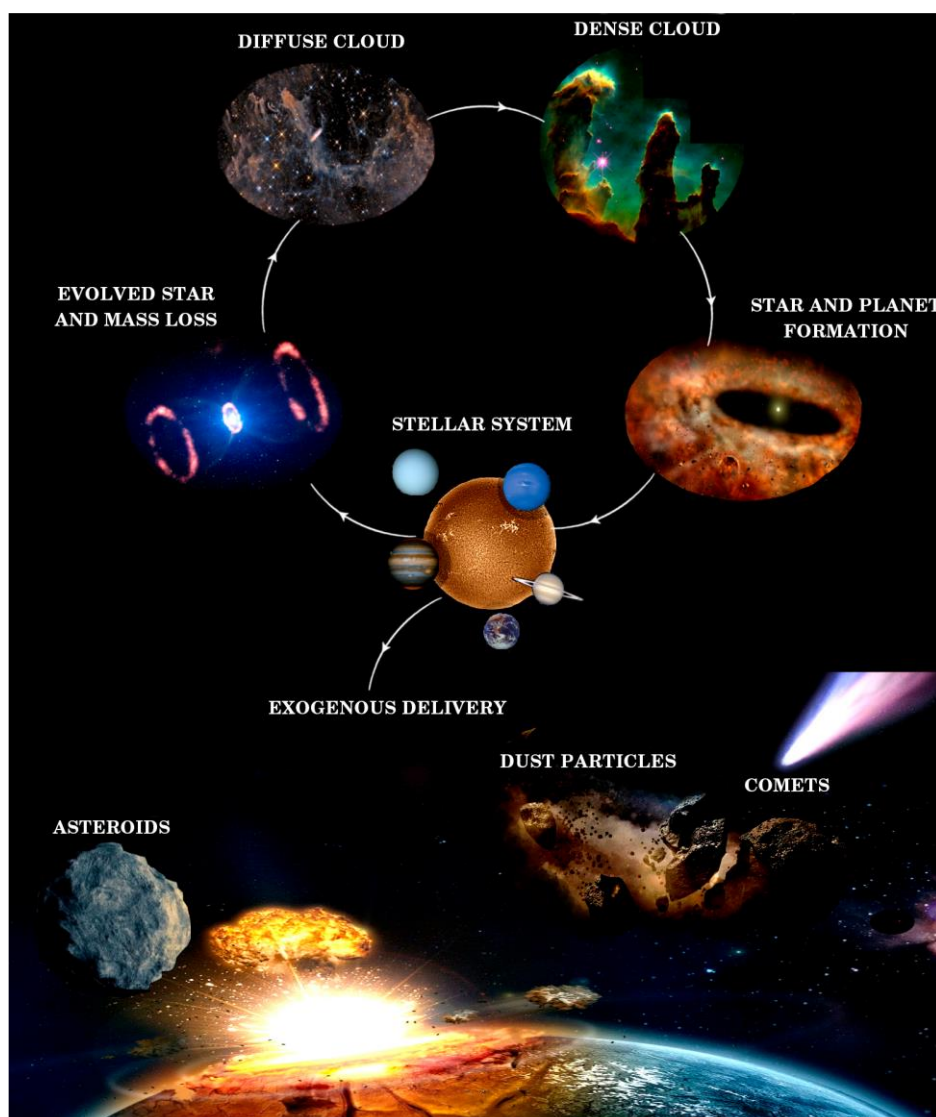


Figure 6.1. Cosmic carbon life cycle. Extracted from (Mateo-Martí, et al., 2019).

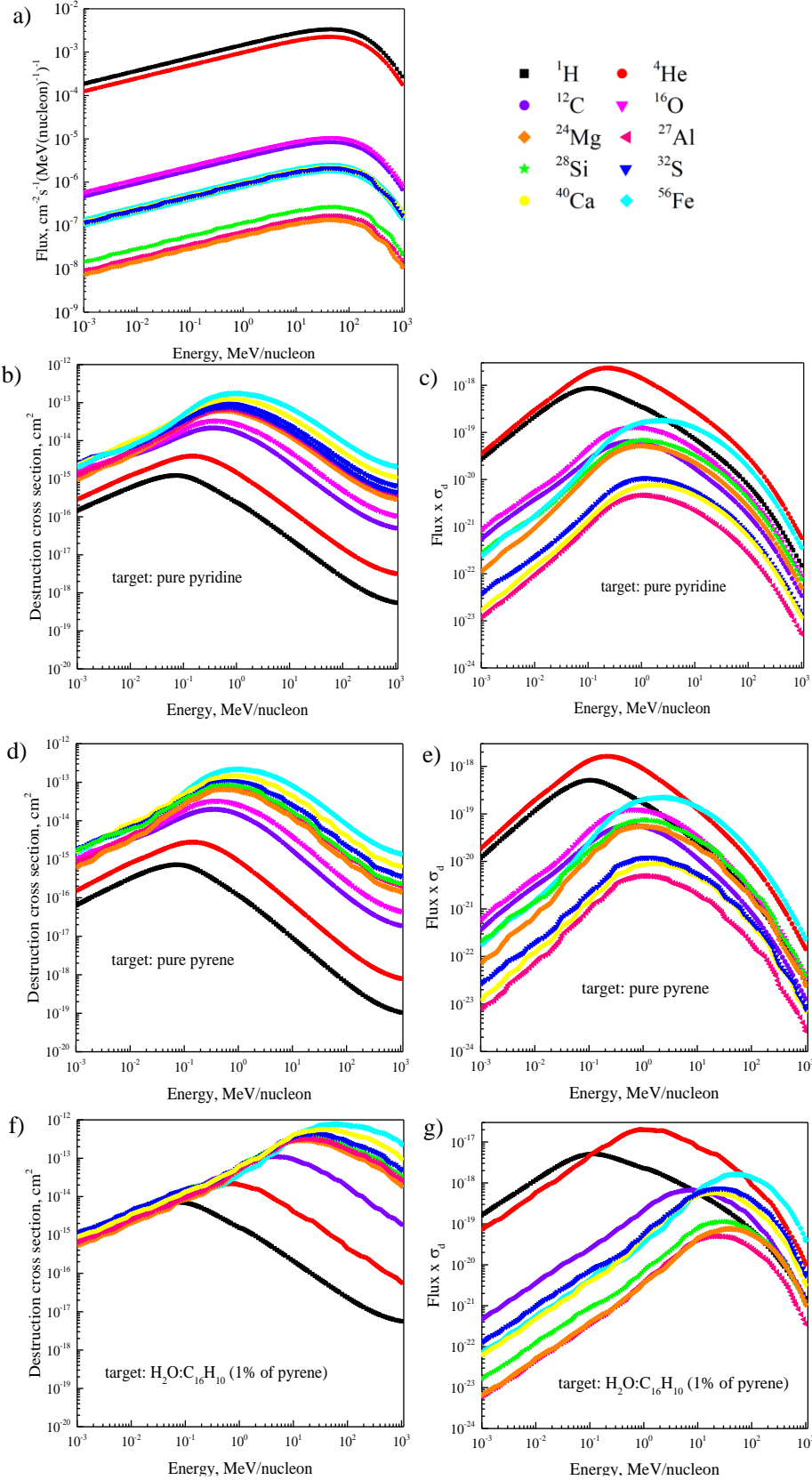


Figure 6.2. a) Flux ( $\Phi(E)$ ) of the ten most abundant cosmic ray constituents. Destruction cross section and differential dissociation rate for different ions in pure pyridine (b, c), pure pyrene (d, e) and in  $\text{H}_2\text{O}:\text{C}_{16}\text{H}_{10}$  mixture with 1% of pyrene (f, g).

The survivability of the molecules can be quantified by their half-life time commonly used in the literature. To evaluate the damage induced by ionic projectiles to molecules in space, we used ion flux data available for Earth's orbit (Webber & Yushak, 1983):

$$\Phi(E) = \frac{C_z E^{0.3}}{(E+E_0)^3} \left[ \frac{\text{particles}\cdot\text{nucl}}{\text{cm}^2\cdot\text{s}\cdot\text{sr}\cdot\text{MeV}} \right], \quad \text{eq. (6.1)}$$

where  $C_z$  is a normalized constant representing the abundance of the element relative to hydrogen.  $E_0 = 400 \text{ MeV}$  is a form parameter and 400 MeV is the most accurate value to describe cosmic ray flux (Shen, et al., 2004).

We calculated the half-life time of pure pyridine and pyrene molecules in dense molecular clouds, as well as the half-life time of pyrene trapped in a water matrix at different pyrene concentrations: 1% and 5%. Using the power law dependences between the destruction cross section and the electronic stopping power of the incident ion, obtained in Chapters 3 and 4 (Figures 3.8, 4.6 and 4.15), we can estimate the destruction of these molecules caused by ten most abundant cosmic ray elements. The normalized constant  $C_z$  for each cosmic ray constituent was extracted from the work of (Portugal, et al., 2014).

Figure 6.2 present the flux of each cosmic ray component as a function of ion energy (a) along with the electronic stopping power of each cosmic ray constituent in pyridine (b), pyrene (c) and in  $\text{H}_2\text{O}:\text{C}_{16}\text{H}_{10}$  mixture with 1% of pyrene (d). The destruction cross section as a function of ion energy, which was obtained using the power law dependence is presented in Figure 6.2 (b, d and f).

The half-life time is calculated with the formula (Portugal, et al., 2014):

$$\tau = \frac{\ln(2)}{\sum j \int_{10^{-3}}^{10^3} \Phi(E)\sigma(E)dE} \text{ [seconds]}, \quad \text{eq. (6.2)}$$

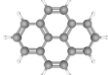
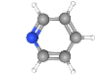
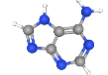
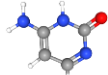
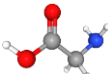
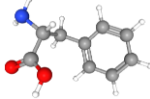
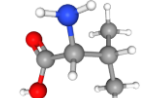
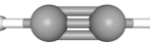
where  $\sum j \int_{10^{-3}}^{10^3} \Phi(E)\sigma(E)dE$  is differential dissociation rate as a function of ion energy in the interval from  $10^{-3}$  to  $10^3$  MeV/nucleon, which is shown in Figure 6.2 (c, e and g).

Table 6.1 shows the half-life times of various organic molecules in dense clouds. The half-life time of pyridine ( $9.1 \times 10^6$  years) is comparable to that of other molecules with six-membered rings in their structure, such as cytosine ( $7.3 \times 10^6$ ) or phenylalanine ( $10 \times 10^6$ ). These values are also similar to the half-life time of nucleobase adenine ( $7.96 \times 10^6$ ), which has fused five- and six-membered rings in the structure. The pyrene molecule ( $82 \times 10^6$ ) is predictably having a longer half-life time than pyridine. It is also well known that aliphatic molecules are less stable than aromatic ones (Bhimabhai, 2018), as clearly demonstrated by comparing the half-life time of glycine ( $2.8 \times 10^3$ ) and valine ( $0.94 \times 10^6$ ) to that of aromatic compounds. For comparison, the small acetylene molecule ( $\text{C}_2\text{H}_2$ ), which has a triple bond between carbon atoms, can survive in dense clouds for up to 230 million years (Pereira, et al., 2020).

Additionally, the half-life times of pyrene trapped in a water matrix was calculated using two concentrations of pyrene in  $\text{H}_2\text{O}:\text{C}_{16}\text{H}_{10}$  mixtures: 1% and 5%. A power dependence model was applied to fit the destruction cross section as a function of electronic stopping power of the incoming ion, following the same methodology as used for pure pyrene (Figure 4.15). As expected, the half-life of pyrene trapped in a water matrix is significantly shorter than that of pure pyrene, estimated to be around 3 million years for  $\text{H}_2\text{O}:\text{C}_{16}\text{H}_{10}$  mixture with 5% pyrene and 1 million years for  $\text{H}_2\text{O}:\text{C}_{16}\text{H}_{10}$  mixture with 1% pyrene (Table 6.2).

The survival of PAHs in dense clouds will primarily depend on the matrix surrounding them. For example, if a grain is composed entirely of pyrene or pyridine, it is likely to survive within a dense cloud, which has a lifespan of several million years, and later contribute to the formation of planetary systems. However, if pyrene is dissolved in a large amount of water, the lifespan of the molecule will clearly be shorter than that of the dense cloud. Other matrix molecules can also influence the radioresistance of PAHs. Therefore, the key factor determining the survival of PAHs is the composition of the matrix in which they are trapped. To better understand this, experiments should be conducted where PAHs are trapped in matrices composed not only of water but also of NH<sub>3</sub>, CO<sub>2</sub>, and CO.

Table 6.1. The half-life time of different organic molecules in the dense clouds.

Molecule	Structure	Ions considered	Half-life time, years	Temperature
Pyrene C <sub>16</sub> H <sub>10</sub>		H, He, O, C, Mg, Si, Fe, S, Al, Ca	82 × 10 <sup>6</sup>	20 K
Pyridine C <sub>5</sub> H <sub>5</sub> N			9.1 × 10 <sup>6</sup>	10 K
Adenine C <sub>5</sub> H <sub>5</sub> N <sub>5</sub>			7.96 × 10 <sup>6a</sup>	13 K
Cytosine C <sub>4</sub> H <sub>5</sub> N <sub>3</sub> O			7.3 × 10 <sup>6b</sup>	20 K
Glycine C <sub>2</sub> H <sub>5</sub> NO <sub>2</sub>		H, He, O, C, Fe, Si, Mg S, Ni, Ca, Al, Mn, V, Cr, Ti, Sc, Ar, K, Cl, P, Co, Cu	2.8 × 10 <sup>3e</sup>	14 K
			7.8 × 10 <sup>3e</sup>	300 K
Phenylalanine C <sub>9</sub> H <sub>11</sub> NO <sub>2</sub>		H, He, C, O, Ne, Fe	10 × 10 <sup>6c</sup>	300 K
Valine C <sub>5</sub> H <sub>11</sub> NO <sub>2</sub>			0.94 × 10 <sup>6d</sup>	300 K
Acetylene C <sub>2</sub> H <sub>2</sub>			230 × 10 <sup>6f</sup>	45 K

*a*- (Vignoli Muniz, et al., 2017), *b*- (Vignoli Muniz, et al., 2022), *c*- (Mejía, et al., 2022), *d* - (Costa, et al., 2020), *e* - (Portugal, et al., 2014), *f* - (Pereira, et al., 2020)

Table 6.2. The half-life times of pure pyrene and pyrene trapped in the water matrix with concentrations 1 and 5 %.

Mixture	Half-life time, years
Pure pyrene	82 × 10 <sup>6</sup>
H <sub>2</sub> O:C <sub>16</sub> H <sub>10</sub> (5% of C <sub>16</sub> H <sub>10</sub> )	2.8 × 10 <sup>6</sup>
H <sub>2</sub> O:C <sub>16</sub> H <sub>10</sub> (1% of C <sub>16</sub> H <sub>10</sub> )	1.3 × 10 <sup>6</sup>

## References

- Bhimabhai, K., 2018. Comparative study of aliphatic and aromatic compounds. *J. Pharm. Innov*, Volume 7, pp. 175-177.
- Burkhardt, A. M. et al., 2021. Discovery of the pure polycyclic aromatic hydrocarbon indene (c-C<sub>9</sub>H<sub>8</sub>) with GOTHAM observations of TMC-1. *The Astrophysical Journal Letters*, 913(2), p. L18.
- Cernicharo, J. et al., 2021. Pure hydrocarbon cycles in TMC-1: Discovery of ethynyl cyclopropenylidene, cyclopentadiene, and indene. *Astronomy & Astrophysics*, Volume 649, p. L15.
- Chevance, M. et al., 2020. The molecular cloud lifecycle. *Space Science Reviews*, Volume 216, pp. 1-42.
- Costa, C. A. D. et al., 2020. Valine radiolysis by H<sup>+</sup>, He<sup>+</sup>, N<sup>+</sup>, and S<sup>15+</sup> MeV ions. *International journal of molecular sciences*, 21(5), p. 1893.
- Mateo-Marti, E. et al., 2019. Characterizing interstellar medium, planetary surface and deep environments by spectroscopic techniques using unique simulation chambers at Centro de Astrobiologia. *Life*, 3(72), p. 9.
- McGuire, B. A. et al., 2021. Detection of two interstellar polycyclic aromatic hydrocarbons via spectral matched filtering. *Science*, 371(6535), pp. 1265-1269.
- Meidt, S. E. et al., 2015. Short GMC lifetimes: an observational estimate with the PdBI Arcsecond Whirlpool Survey (PAWS). *The Astrophysical Journal*, 806(1), p. 72.
- Mejía, C., da Costa, C. A., Iza, P. & da Silveira, E. F., 2022. Irradiation of Phenylalanine at 300 K by MeV Ions. *Astrobiology*, 22(4), pp. 439-451.
- Pereira, R. et al., 2020. Ion irradiation of acetylene ice in the ISM and the outer Solar system: laboratory simulations. *Monthly Notices of the Royal Astronomical Society*, 495(1), pp. 40-57.
- Portugal, W. et al., 2014. Radiolysis of amino acids by heavy and energetic cosmic ray analogues in simulated space environments:  $\alpha$ -glycine zwitterion form. *Monthly Notices of the Royal Astronomical Society*, 441(4), pp. 3209-3225.
- Sandford, S. A., Nuevo, M., Bera, P. P. & Lee, T. J., 2020. Prebiotic astrochemistry and the formation of molecules of astrobiological interest in interstellar clouds and protostellar disks. *Chemical reviews*, 120(11), pp. 4616-4659.
- Shen, C. J., Greenberg, J. M., Schutte, W. A. & Van Dishoeck, E. F., 2004. Cosmic ray induced explosive chemical desorption in dense clouds. *Astronomy & Astrophysics*, 415(1), pp. 203-215.
- Vignoli Muniz, G. S. et al., 2022. Radiolysis of cytosine at cryogenic temperatures by swift heavy ion bombardments. *ACS Earth and Space Chemistry*, 6(9), pp. 2149-2157.
- Vignoli Muniz, G. S. et al., 2017. Radioresistance of adenine to cosmic rays. *Astrobiology*, 17(4), pp. 298-308.

Webber, W. R. & Yushak, S. M., 1983. A measurement of the energy spectra and relative abundance of the cosmic-ray H and He isotopes over a broad energy range. *Astrophysical Journal, Part 1 (ISSN 0004-637X)*, Volume 275, pp. 391-404., 275, 391-404.

## Conclusion and perspectives

In this work we investigated how ions in space interact with aromatic molecules of astrochemical relevance in the solid phase. The study focused on two aromatic molecules: pyridine, which plays an important role in biochemical processes in living beings, and pyrene, one of the simplest PAHs, which is ubiquitous on Earth and in meteorites and asteroids. Both molecules are considered to be present in space and to play a role in carbon cycle, although they have not yet been detected.

These two aromatic molecules were irradiated at the GANIL and ATOMKI facilities with both light and heavy ions, imitating solar wind and galactic cosmic rays. The main technique used for sample analysis was infrared spectroscopy. Using pyridine, we investigated for the first time how the initial structure (amorphous/crystalline) influences the destruction cross section and found out that the crystalline structure has a higher destruction cross section. We investigated the effect of irradiation temperature on the destruction cross section of pyridine and concluded that this does not have a significant impact. Additionally, we studied the influence of the aqueous matrix on the destruction cross section of pyridine and obtained results that confirm previous studies: as the concentration of pyridine in the aqueous matrix decreases, the destruction cross section of pyridine increases. It was attributed this to the indirect effect, where increased water concentration results in a greater number of water radicals attacking the pyridine molecules.

For the pyrene molecule, we focused on evaluating the destruction effects from both heavy and light ions. We found that the local dose is not the key parameter, as the destruction caused by heavy ions was significantly greater than that caused by light ions, despite the same deposited local dose. Additionally, we conducted experiments involving the irradiation of pyrene-water mixtures and observed the same effect, which was mentioned earlier: the destruction cross-section dramatically increases as the concentration of pyrene in the mixture decreases.

For both pyridine and pyrene, the new species that emerged during irradiation were identified. The formation cross sections were determined for some of these species.

For both molecules, the main goal was to predict the survivalability of pyridine and pyrene in space. To achieve this, we identified the relationship between the destruction cross section and electronic stopping power of incoming ion to predict the destruction effect on these molecules when exposed to cumulative irradiation from all ions present in space. We found that pure pyridine and pure pyrene may survive approximately 9 and 80 million years, respectively, in dense clouds, which approximately corresponds to the lifetime of a dense cloud. However, when pyrene is trapped in a water matrix, its lifetime predictably decreases to just 1 million years, when its concentration is 1% in the water matrix.

Additionally, a comparative analysis of the destruction cross section for PAHs of different sizes (indene, naphthalene, phenanthrene, adamantane and pyrene) irradiated with heavy ions was conducted. We concluded that the probability of molecular destruction decreases with increasing atomic weight, a trend previously observed for photon irradiation in the literature. This is because, under external influence, larger molecules tend to wobble and relax rather than break bonds, which is more energetically favorable for smaller molecules.



Since much of the work in this study was done for the first time in our group, including the irradiation of crystalline structures and the use of PAHs as the solid target, many aspects can still be improved.

For example, for a more realistic simulation of the conditions under which organic material evolves in the icy mantles, it is necessary to add CO, CO<sub>2</sub> and NH<sub>3</sub> to the water matrix. Since the concentration of these molecules can reach up to 40% in the icy mantle, they can either balance the effects caused by water or lead to unpredictable consequences for organic matter trapped in the mantle.

The concept of the deposited local dose as a “key parameter” still remains unclear. Our research shows that H and He ions cause significantly less damage to pyrene and adenine compared to heavier ions, starting from C. However, in previous studies on valine irradiation, this was not the case — when the deposited local dose was the same for H, He and heavy ions, the extent of damage was comparable. This discrepancy might be explained by the molecular structure, as pyrene and adenine have stable aromatic structure, while valine has less stable aliphatic structure. In any case, further experiments with other molecules, as well as theoretical calculations, are needed to gain a better understanding of this effect.

In addition to ions, the space is penetrated with other types of ionizing radiation, such as electrons and photons. Ions, photons and electrons generally interact simultaneously, though one type may dominate depending on the location. Therefore, it is important to determine whether there is a synergic effect when different types of ionizing radiation are present simultaneously. For these purposes, MIRPLAA (Multiple-beam IRRadiation PLAtform) is being designed at CIMAP laboratory in Caen, which will allow simultaneous irradiation of the samples with ions, photons, and electrons. The chamber will be equipped with an ion trap, allowing the detection of volatile species released during irradiation and the heating of the sample afterward.

In this study, we relied only on the infrared spectroscopy to analyse the compounds, formed during irradiation, even though it is not the most effective technique for identifying new molecules. We made efforts to send samples to other laboratory for the identification of new compounds using high-resolution mass spectroscopy method, but due to technical challenges, this could not be achieved before the completion of this thesis. In the future, in order to obtain a more comprehensive understanding of the compounds formed during irradiation, it would be very useful to use laser desorption ionisation or electrospray methods.